DESIGN AND CHARACTERISTICS OF HIGH PERFORMANCE MID-WAVELENGTH TYPE-2 SUPERLATTICE SENSORS

A THESIS SUBMITTED TO
THE GRADUATE SCHOOL OF NATURAL AND APPLIED SCIENCES
OF
MIDDLE EAST TECHNICAL UNIVERSITY

BY

FİKRİ OĞUZ

IN PARTIAL FULFILLMENT OF REQUIREMENTS
FOR
THE DEGREE OF MASTER OF SCIENCE
IN
MICRO AND NANOTECHNOLOGY

JANUARY 2018

Approval of the thesis:

DESIGN AND CHARACTERISTICS OF HIGH PERFORMANCE MID-WAVELENGTH TYPE-2 SUPERLATTICE SENSORS

submitted by **FİKRİ OĞUZ** in partial fulfillments of the requirements for the degree of **Master of Science in Micro and Nanotechnology Department, Middle East Technical University** by,

Prof. Dr. Gülbin DURAL ÜNVER _____
Dean, Graduate School of **Natural and Applied Sciences**

Assoc. Prof. Burcu AKATA KURÇ _____
Head of Department, **Micro and Nanotechnology**

Assoc. Prof. Dr. Alpan BEK _____
Supervisor, **Physics Dept., METU**

Examining Committee Members:

Prof. Dr. Ekmel ÖZBAY _____
Electrical and Electronics Eng. Dept., Bilkent University

Assoc. Prof. Dr. Alpan BEK _____
Physics Dept., METU

Prof. Dr. Mehmet Parlak _____
Physics Dept., METU

Assist Prof. Dr. Selçuk Yerci _____
Electrical and Electronics Eng. Dept., METU

Assist Prof. Dr. Emre Yüce _____
Physics Dept., METU

Date:24.01.2018

I hereby declare that all information in this document has been obtained and presented in accordance with academic rules and ethical conduct. I also declare that, as required by these rules and conduct, I have fully cited and referenced all material and results that are not original to this work.

Name, Last Name : Fikri OĞUZ

Signature :

ABSTRACT

DESIGN AND CHARACTERISTICS OF HIGH PERFORMANCE MID-WAVELENGTH TYPE-2 SUPERLATTICE SENSORS

OĞUZ, Fikri

M.Sc., Department of Micro and Nanotechnology

Supervisor: Assoc. Prof. Alpan BEK

Co-Advisor: Dr. Yetkin ARSLAN

January 2018, 126 pages

Type-II Superlattices (T2SLs) are bandgap engineered structures that have attracted a lot of attention in the last couple of decades and is still some of the hot topics in infrared imaging applications. T2SLs are the most promising member of the quantum structured infrared family. By the end of maturity period of T2SLs, Focal Plane Array (FPA) level products have been released since a decade. Offering performance compatible with high-end infrared systems, yielding respectable results and still being open to further development make T2SL subjects worth to work on. The flexibility in design and the opportunity provided by nature of structures enable

researchers and manufacturers to give their focus on this today's world materials system. This thesis work covers the state of the art Mid-Wavelength Infrared Region (MWIR) InAs/GaSb Type-II Superlattice infrared technology in terms of design, fabrication, and characterization. Large format (640 x 512) and small pitch (15 μm) architecture are implemented for the fabrication of T2SL FPAs.

The critical design parameters and design approaches for ultimate performance and reasons for capabilities of T2SLs to offer such performance are handled. After the presentation of detailed fabrication procedure and experimented fabrication methods, large area pixel level and FPA level characterizations are also discussed. The performance comparisons of experimented fabrication processes are demonstrated.

With dark current modeling of large area T2SL diodes, the dominant dark current mechanisms for varying bias regions are clarified. With this modeling, our properly designed T2SL structure shows no tunneling dark current and is dominated only by detector shunt current at most of the bias regions.

Electro-optical measurements yielded very satisfactory results. The optimized FPA which is a 15 μm pitch detector with cut-off wavelength of 4.92 μm yields 1.2 A/W peak responsivity and 30 mK Noise Equivalent Temperature Difference (NETD) with $f/2.3$ optics. The calculated quantum efficiency for this detector is larger than 60 %. Example images were acquired using optimized FPA device, and are provided in the thesis for demonstrative purposes.

Keywords: Type-2 Superlattice, Infrared Photodetectors, Mid-wavelength Infrared Region, Focal Plane Array, Dark Current Modeling

ÖZ

YÜKSEK PERFORMANSLI ORTA DALGABOYU TİP-2 SÜPERÖRGÜ SENSÖRLERİN DİZAYN VE KARAKTERİSTİKLERİ

OĞUZ, Fikri

Yüksek Lisans, Mikro ve Nanoteknoloji Bölümü

Tez Yöneticisi: Doc. Dr. Alpan BEK

Eş Danışman: Dr. Yetkin ARSLAN

Ocak 2018, 126 sayfa

Tip-II Süperörgüler (T2SÖ), yakın tarih boyunca büyük ilgi çeken, bant aralığı tasarlanmış yapılardır ve günümüzde kızılötesi görüntüleme uygulamaları için hâlâ gündemdedir. T2SÖ'ler, kuantum yapılı kızılötesi ailesinin en umut vadeden üyesidir. T2SÖ'lerin olgunlaşma sürecinin tamamlanmasıyla birlikte, Odak Düzlem Dizini (ODD) seviyesinde ürünler piyasaya sürülmüştür. Uzun soluklu olgunlaşmış kızılötesi sistemler ile uyumlu performans sunması, kaydadeğer sonuçlar vermesi ve gelişime hâlâ açık olması, T2SÖ'leri çalışılmaya değer yapmıştır. Tasarımdaki esnekliği ve yapısının doğası gereği sunduğu avantajlar, araştırmacıların ve üreticilerin ilgilerini, günümüzün malzeme sistemine vermelerine teşvik etmiştir.

Bu tez çalışması, son teknoloji Orta-Dalgaboyu Kızılötesi (ODK) InAs/GaSb Tip-II Süperörgü kızılötesi teknolojisinin temel olarak tasarım, üretim ve karakterizasyon aşamalarını kapsamaktadır. Geniş formatlı (640 x 512) ve küçük piksel adımlı (15 μm) yapı T2SÖ ODK'ların üretimi için uygulanmıştır.

Üst düzey performans için önemli olan tasarım parametreleri ve yaklaşımları ve T2SÖ'lerin böyle performans sunabilme yeteneklerinin sebepleri ele alınmıştır. Detaylandırılmış üretim süreci yöntemleri ve araştırılmış üretim metotlarının sunumundan sonra, geniş alanlı piksel ve ODK seviyesindeki karakterizasyonlar ayrıca incelenmiştir. Üretim süreçlerinin performans karşılaştırmaları sunulmuştur.

Geniş alanlı T2SÖ diyotlarının karanlık akım modellemeleri ile birlikte, değişen yönlendirme gerilimleri için baskın karanlık akım mekanizmaları açığa çıkarılmıştır. Bu modelleme ile birlikte, uygun bir şekilde tasarlanmış T2SÖ yapısının, hiçbir tünelleme karanlık akımı göstermediği ve çoğu yönlendirme bölgesinde sadece paralel akım ile baskılandığı gözlenmiştir.

Elektriksel-optik ölçümler oldukça tatmin edici sonuçlar vermiştir. Nihai hale getirilmiş 4.92 μm kesim dalga boyuna sahip olan 15 μm piksel adımlı ODK, $f/2.3$ optik ile, 1.2 A/W tepe tepkisellik değeri ve 30 mK Gürültüye Eşdeğer Sıcaklık Farkı (GESF) sunmuştur. Bu dedektör için hesaplanan kuantum etkinliği değeri % 60'tan fazladır. Örnek görüntüler nihai hale getirilmiş ODK aygıtı ile elde edilmiştir ve sergileme amacıyla tez içerisinde sunulmaktadır.

Anahtar Kelimeler: Tip-2 Süperörgü, Kızılötesi Fotodedektör, Orta Dalga Boyu Kızılötesi, Odak Düzlem Dizini, Karanlık Akım Modelleme

To my recently deceased grandmother and grandfather

ACKNOWLEDGMENT

First of all, I would like to thank **Prof. Dr. Ekmel ÖZBAY** for giving me the opportunity for doing my master thesis as a member in his group at Nanotechnology Research Center (NANOTAM) at Bilkent University. His countless advice and suggestions make this group such a pleasant place to work.

I would like to thank, my supervisor **Assoc. Prof. Dr. Alpan BEK**, for everything without any exception. Also, I would like to express my gratitude for your incredible help during the whole thesis time.

I would like to thank my co-advisor **Dr. Yetkin ARSLAN**, for always having an infinite amount of ideas and time for my questions, for all your patience and even more for never hesitating to tell me when I am wrong, and for pushing me to excel beyond limits I did not think possible. I think we both know I have come a long way since we first met, and I owe very much of that to you. Throughout these years I received the help, guidance and the lessons that no one else could and would provide

I would like to thank, **Prof. Dr. Mehmet PARLAK** and **Assist. Prof. Dr. Emre YÜCE,** for their valuable comments and being on my thesis committee.

I would like to thank **Mr. Erkin ÜLKER** for sharing his experiences in the whole cycle of thesis work and his ability to overcome obstacles intentionally or unintentionally created.

Thanks to **Özlem ARSLAN**, **Halit DOLAŞ** and **Murat İLDERE** for being such helpful friends.

Most importantly, I would like to thank my parents, my friends and my ‘big’ family for their care throughout all these years. I am very grateful for their understanding and support.

Last but not least, I also give my special thanks for my wife in future **Deniz Şule UĞUR** for experiencing life with me, supporting me without any exception and enduring my ‘lovely’ mood in thesis writing time. It is an indescribable feeling that to know, you are there.

TABLE OF CONTENTS

ABSTRACT V
ÖZ VII
ACKNOWLEDGMENT X
TABLE OF CONTENTS XII
LIST OF FIGURES XV
LIST OF TABLES XIX
CHAPTERS
1. INTRODUCTION 1
2. INFRARED RADIATION AND DETECTORS 7
2.1. Blackbody Radiation 8
2.2. Atmospheric Transmission 11
2.3. Detector Types 15
2.3.1. Thermal Detectors 15
2.3.2. Photon Detectors 16
2.4. Figure of Merits 20
2.4.1. Quantum Efficiency (QE) 20
2.4.2. Noise 21
2.4.3. Responsivity (R) 22
2.4.4. Noise Equivalent Power (NEP) 23
2.4.5. Detectivity (D) 24
2.4.6. Noise Equivalent Temperature Difference (NETD) 24
2.4.7. Modulation Transfer Function (MRTD) 25
2.4.8. Minimum Resolvable Temperature Difference (MRTD) 25
2.5. Imaging Concept 25
2.6. Technology Comparison 27

3. TYPE-II SUPERLATTICE TECHNOLOGY 31
3.1. History of Type-II Superlattices..... 32
3.2. Basic Properties of Type-II Superlattices 35
3.2.1. 6.1Å Material System..... 36
3.2.2. Tunneling Effect..... 37
3.2.3. Auger Recombination 38
3.2.4. Dark Current Mechanism..... 39
3.3. Recent Developments..... 42
4. FABRICATION OF MWIR INAS/GASB FOCAL PLANE ARRAY 47
4.1. Type-II Superlattice Epilayer Design..... 48
4.2. Type-II Superlattice Focal Plane Array Fabrication 50
4.2.1. Mesa Formation 52
4.2.1.1. Wet Etching..... 52
4.2.1.2. Dry (Plasma) Etching..... 55
4.2.2. Ohmic Contact 58
4.2.3. Passivation..... 59
4.2.3.1. SiO_2 59
4.2.3.2. Photoresist..... 63
4.2.3.3. Polyimide 64
4.2.4. Pre-treatments 67
4.2.5. Under Bump Metallization (UBM) and In Bump Formation 68
4.2.6. Dicing, Flip-Chip Bonding, and Injection of Underfill..... 72
4.2.7. Substrate Thinning 73
5. CHARACTERIZATION OF TYPE-II SUPERLATTICE..... 77
5.1. Performance Comparison of Different Fabrication Methods..... 78
5.1.1. Large Area Detector Fabrication..... 78
5.1.2. I-V Measurement Setup 79
5.1.3. I-V Comparison of Applied Fabrication Methods 79
5.1.3.1. I-V Comparison of Mesa Etching Methods and Etch Depth Analysis 79
5.1.3.2. Determination of Passivation Method and Material 81

5.2. Dark Current Modeling of T2SL 92
5.3. NETD and Responsivity Measurements 100
5.3.1. Responsivity and NETD Measurement Setups 100
5.3.2. NETD and Responsivity Measurements 101
5.4. FPA Image Demonstration of T2SL FPA 107
6. CONCLUSIONS AND FUTURE WORK 113
REFERENCES 115
APPENDIX
OCTAVE SCRIPT 123

LIST OF FIGURES

FIGURES

Figure 2.1. Blackbody spectral radiant emittance and spectral radiance for different temperatures [21]. 10

Figure 2.2. Atmospheric transmission and respective particles responsible for absorption [22]. 12

Figure 2.3. The energy transition in extrinsic and intrinsic detector structures [24]. 18

Figure 2.4. Photoconductor type detector operation [19]. 19

Figure 2.5. p-n junction photon detector operation [19]. 20

Figure 3.1. Schematic illustration of an InAs/Ga(In)Sb type-II broken-gap superlattice showing the spatial separation of the conduction band and the heavy-hole band wave functions. The infrared transition is indicated by an arrow [30]..... 32

Figure 3.2. Band edge energy positions for (A) unstrained InAs and GaSb and (B) strained InAs and $Ga_{0.6}In_{0.4}Sb$ in a free-standing InAs/GaInSb superlattice [30]. .. 34

Figure 3.3. The schematic illustration of broken-gap type-II alignment [57]..... 36

Figure 3.4. Zone center (**Γ**-point) conduction and valence band edge positions plotted against lattice parameter for antimonide, arsenide and arsenide-antimonide III-V semiconductors [30]. 37

Figure 3.5. Thermal image of 320 x 256 InAs/GaSb SLs nBn design at 77 K with 16.3 ms integration time [67]. 42

Figure 3.6. Left image 3-4 μm channel, right image 4-5 μm, white indicates colder region [68]. 43

Figure 3.7. 640 x 512 15 μm pitch FPA images at 90 K [69]. 43

Figure 3.8. Image of 6 μm cut-off wavelength [70]. 44

Figure 3.9. The images taken at different temperatures, from 81 K to 150 K [71].. 44
Figure 3.10. 320 x 256, 30 µm pitch p-i-n FPA image [72]..... 45
Figure 3.11. 1156 x 2040, 5 µm pitch FPA images at 150 K [73]. 45
Figure 3.12. 10 µm pitch 2k x 2k FPA images at 120 K and 150 K with $\boldsymbol{f3.9}$ [74]. 46
Figure 4.1. Band gap and respective wavelength as a function of lattice constants for III-V semiconductors [75]. 49
Figure 4.2. T2SL epilayer design used in this thesis (not to scale). 50
Figure 4.3. T2SL FPA fabrication steps (not to scale). 51
Figure 4.4. Illustration of the T2SL pixel after fabrication processes completed (not to scale)..... 51
Figure 4.5. The SEM image of H_3PO_4 : H_2O (3:1) etched sample..... 54
Figure 4.6. SEM images of mesa etched sample with $C_6H_8O_7$ / H_2O : H_3PO_4 : H_2O_2. 55
Figure 4.7. The initial result of dry etching of T2SL. 57
Figure 4.8. The optimized dry etching recipe results in mesa structures. 57
Figure 4.9. The enhanced dry etching recipe result in mesa structures..... 58
Figure 4.10. SiO_2 coated mesa structures with PECVD method..... 61
Figure 4.11. SEM images of e-beam SiO_2 coated samples with passivation openings. 62
Figure 4.12. Microscope image of photoresist coated wafers with passivation openings..... 64
Figure 4.13. SEM images of uncured Poly-a and its passivation openings. 65
Figure 4.14. Microscope images uncured Poly-b and its passivation openings..... 65
Figure 4.15. SEM images of cured Poly-a and its passivation openings. 66
Figure 4.16. SEM images of uncured Poly-b and its passivation openings. 66
Figure 4.17. SEM images of $(NH_4)_2S$ treated surfaces. 68
Figure 4.18. SEM images of positive photoresist develop profile. 69
Figure 4.19. SEM images of negative photoresist develop profile with different post-exposure bake temperatures, (a) at 115 ℃, (b) at 120 ℃, (c) and (d) at 125 ℃..... 70
Figure 4.20. SEM images of In bumps formed with positive photoresist..... 71

Figure 4.21. SEM images of In bumps formed with the negative photoresist. 71
Figure 4.22. SEM images of ROIC In bumps formed with a negative photoresist. 72
Figure 4.23. SEM images of the grinded substrate. 74
Figure 4.24. SEM images of chemically etched but not completely removed substrate..... 74
Figure 4.25. FPA-ROIC hybrid on LCC in the dewar. 75
Figure 5.1. Dark currents of 220 µm x 220 µm pixel area samples, etched dry and wet at 77 K. 80
Figure 5.2. I-V characteristics of deep and short etch-depth samples sized 220 µm x 220 µm at 77 K..... 81
Figure 5.3. The dark current comparison of different passivation methods/materials at 77 K. 82
Figure 5.4. The dark current comparison of $(NH_4)_2S$ pre-treated sample with SiO_2 PECVD sample at 77 K..... 83
Figure 5.5. The dark current comparison of different passivation methods/materials at 77 K. 84
Figure 5.6. Dark current densities of passivation methods and materials. 85
Figure 5.7. Dark current densities of passivation methods and materials. 86
Figure 5.8. Dark current comparison of cured and uncured polyimides. 87
Figure 5.9. Dark current comparison of cured and uncured polyimides. 88
Figure 5.10. Photocurrent of differently passivated samples at 77 K. 89
Figure 5.11. Photocurrent of differently passivated samples at 77 K. 90
Figure 5.12. The photo-current over the dark current ratio of differently passivated samples with varying bias voltage. 91
Figure 5.13. R_0. A product of differently passivated samples. 92
Figure 5.14. The result of dark current simulation in between -1.5 V and -1.0 V... 97
Figure 5.15. The result of dark current simulation in between -1 V and -0.2 V..... 98
Figure 5.16. The result of dark current simulation in between -0.8 V and 0.05 V. . 99
Figure 5.17. Cold and hot frame averages for 640 x 512 T2SL FPA. 101
Figure 5.18. Noise and high noise mappings for 640 x 512 T2SL FPA. 102
Figure 5.19. NETD and responsivity mapping for 640 x 512 T2SL FPA. 103

Figure 5.20. Low and high responsivity mapping for 640 x 512 T2SL FPA..... 104
Figure 5.21. High NETD and total bad pixel mapping for 640 x 512 T2SL FPA. 105
Figure 5.22. NETD histogram for 640 x 512 T2SL FPA..... 105
Figure 5.23. Responsivity spectrum for the T2SL FPA for varying bias voltages. 106
Figure 5.24. An image acquired by a 640 x 512 MWIR SiO_2 passivated and $(NH_4)_2S$ pre-treatment FPA at 77K. 107
Figure 5.25. An image acquired by a 640 x 512 MWIR SiO_2 passivated T2SL FPA at 77 K. 108
Figure 5.26. An image acquired by a T2SL FPA having 50 µm substrate. 109
Figure 5.27. An image acquired by a T2SL FPA having completely removed substrate. 110
Figure 5.28. An image acquired by a 640 x 512 MWIR Type-II Superlattice Detector. 111

LIST OF TABLES

TABLES

Table 2.1. Infrared Thermal Detectors [22]. 16

Table 4.1. Lattice constants and bandgap for selected III-V compound semiconductors [75]. 49

Table 4.2. GaSb and InAs etching solutions [76]. 53

Table 4.3. Etch rates for different materials where A, B, and C are citric acid based solution, tartaric acid based solution, and hydrochloric acid-based solutions, respectively. 53

Table 5.1. Dark Current values of passivation methods/materials at -0.1 V at 77 K. 84

Table 5.2. The fitting parameters for simulating dark current of the InAs/GaSb T2SL detector. 95

CHAPTER 1

INTRODUCTION

Infrared imaging is an important concept that provides opportunities in many field ranging from daily work applications to advanced scientific studies such as weather forecasting, remote temperature sensing, night vision, and target acquisition. Furthermore, infrared radiation makes possible to observe far away objects having a very low temperature or being in a dusty environment especially for astronomic applications. Infrared region has separated into different sub-regions according to the wavelength of photons, namely Visible Region (VIS - 0.4 μm – 0.7 μm), Near Infrared Region (NIR - 0.7 μm – 1.4 μm), Short Wave Infrared Region (SWIR - 1.4 μm – 3.0 μm), Mid-Wave Infrared Region (MWIR - 3.0 μm – 8.0 μm), Long Wave Infrared Region (LWIR - 8.0 μm – 12 μm), Very-Long Wave Infrared Region (VLIR - 12 μm – 20 μm), and Far Infrared Region (FIR - 20 μm – 1000 μm). Imaging technologies of each of these regions differ from each other. Also, numbers of elements participate in imaging cycle such as optics elements, lenses, signal converters, and power suppliers. However, the element that the conversion of gathered photons to electrical signal takes place, and thus, that is at the heart of the imaging is Focal Plane Array (FPA). In this thesis, it is aimed to design, fabricate, and characterize a high-performance MWIR FPA based on Type-II Superlattice (T2SL) active region. By using proper design, 640 x 512 large format array with 15 μm pixel pitch FPAs are fabricated and characterized.

The term infrared is the combination of *infra* -beyond or below- and red meaning that beyond the red. The origin of it comes from the region, which belongs to the electromagnetic spectrum. The region starting from the end of the visible spectrum ranging to microwave part is called infrared region. It covers up all light having wavelength 0.7 μm to 1 mm. On the one hand, radiation in this part of the electromagnetic spectrum is used in various military applications namely night vision, target acquisition, surveillance, homing, and tracking; on the other hand, also in medical applications; such as weather forecasting, remote temperature sensing for daily life. Since it addresses many fields and applications, infrared (IR) technology has been an active research topic for a long time. Performing research and developing technology assures the advancements in each area regarding reliability, operability, and low cost for mass production. The era of finding/developing new materials and new methods has started.

The history of the infrared radiation dates from the first experiment with thermometer conducted by Frederick William Herschel. In 1800, he measured the distribution of energy in sunlight by using a thermometer as a detector [1]. After a relatively long time, thermoelectric effect is discovered by Thomas Johann Seebeck in 1826 [2,3]. After the discovery of Seebeck, L.Nobili improves the electrical thermometer by using the fundamentals of thermoelectric effect, and he invented the first thermocouple, which is used in many areas today [3]. Thermopiles, the connection of several thermocouples, were made by Macedonio Melloni [4]. Samuel Pierpont Langley developed his first bolometer in 1880, and over 20 years, he enhanced his bolometer resulting in reaching the ability to detect heat from about 400 meters [5].

Initially, IR detectors were not separated as thermal detectors or photon detectors. Willoughby Smith in 1873 showed the first photon effect with selenium conductivity [6]. Theodore W. Case discovered the IR photoconductivity of some sulfur-containing substances in 1917 [7]. The significant part of the developments in IR technology was accomplished in the second part of the 20th century. During the World War II and after the war, many research and discoveries were made. In the 1950s, the narrow bandgap materials like InSb and HgCdTe drew attention. The performance

enhancements in epitaxial growth techniques pushed IR technology forward, and it was possible to produce better detectors and quantum structured detectors, as well [8]. After the discovery of HgCdTe by mixing HgTe-CdTe crystals, Lawson and co-workers [9], the domination of this ternary material in the infrared world began because of its outstanding optical and electrical properties. Initially, some other ternary compound materials like PbSnTe were proposed to rival with HgCdTe. However, dielectric properties and the high thermal expansion coefficient of PbSnTe did not satisfy the requirements of infrared detectors such as high responsivity frequency and coupling reliability. In 1970, Esaki et al. published new infrared structure namely "Superlattice" [10]. It was the first proposal of superlattice structures in literature. Esaki's and his friends' idea about superlattice structures threw Quantum Well Infrared Photon (QWIP) detectors and Type-II Superlattices out for consideration. Infrared detection is dependent on intersubband transition in quantum wells for QWIPs [11–13].

In 1983, initial experiments were done by Chiu et al. [14]. The observations on QWIP structure continued with West's and Eglashs's studies [15]. In 1987 at Bell Labs, Levine and co-workers finished his work showing first QWIP FPA [16]. While these works had been studying about QWIPs, the idea of broken band alignment and Type-II superlattices were born. The history and development of Type-II superlattices will be given in details in Chapter III.

Being fast and giving high performance make photon detectors more attractive research topic compared to thermal sensors. Especially after the 1930s, photon detectors suppressed thermal sensors, and research on thermal detectors significantly decreased. Thermal detectors are less favorable than photon detectors for military and commercial applications; since they give a slower response, and they are less sensitive, compared to photon detectors. However, cooling requirement, which increases the cost of the detector, and high cost/low-reliability photon detector systems attracted attention to producing better uncooled thermal detectors.

From the 1940s to the 1970s, large numbers of studies were performed on uncooled thermal detectors [17,18]. In the mid-1990s, amorphous silicon technology for bolometer fabrication has appeared [19]. Today, VO_x microbolometers dominate thermal detector market.

The previously mentioned detector types and systems are called 1st and 2nd generation infrared detectors. The main approaches for infrared detectors today are focused on enhancing spectral capabilities, reducing array sizes, small pixel pitch, large format arrays with high pixel count, high operating temperature resulting in lowered power and cooling requirements, and detectors having those features are called 3rd generation infrared detectors. Therefore, in this thesis study, the design and characteristics of 3rd generation 15 μm pitch MWIR Type-II Superlattice (T2SL) sensors are studied. 640 x 512 large format with small pixel pitch FPAs are fabricated. The primary objectives of this thesis work can be summarized as follows:

- The first part of this study is devoted to the fabrication of T2SL FPAs. Different methods in each fabrication step are performed to optimize device performance. The morphologic investigation of T2SL structures will be explained in detail.
- The second part is focused on the characterization of fabricated T2SL test detectors. The electro-optical performance comparisons of experimented methods in fabrication steps will be presented. Also, the laboratory images acquired by fabricated MWIR 15 μm pitch Type-II superlattice FPA will be provided.

Contrary to initial studies, today, significant number of research is kept secret by developers and manufacturers because of the critical usage areas of infrared detectors, and the rivalry between each other. In line with this approaches, some details of fabrication steps will be skipped.

The thesis starts with introducing the history and usage area of the infrared detector. It also presents the flow chart of the thesis and highlights the significance of the work. This introduction is followed by a review of technical background on infrared radiation and fundamentals. The current technology comparisons of different infrared materials are given. The third chapter of this thesis work describes the specific

features of Type-II superlattice structures in terms of technical background and performance criteria besides with history of them. The latest detector technology status will be presented, and the state-of-the-art studies will be discussed. In following next chapter, the design and fabrication details of Type-II Superlattices are given. Different fabrication methods to reach ultimate performance, and their morphologic investigations are studied. Chapter V presents the characterization methods of Type-II Superlattices and electro-optical performance comparisons of tested fabrication methods. The dark current modeling of large area diodes is also served. The FPA level performance for fabricated T2SL FPAs is handled. The final decision of fabrication methods for optimum device performance is also underlined. Chapter VI includes significant portions of the study, necessary conclusions drawn in this thesis, and the main focus of future work.

CHAPTER 2

INFRARED RADIATION AND DETECTORS

In atomic scale, all atoms forming an object vibrate continuously. Depending on own energy, the frequency of vibrational motion changes in a sense that the higher energy, the more frequently vibration is. The origin of electromagnetic waves comes from these vibrational motions of atoms. When the temperature increases meaning that the energy of each atom increases, the vibration of molecules also rises resulting in, more electromagnetic waves emitted from these objects. Therefore, it can be stated that all objects which have the temperature above absolute 0 temperature (0 K) continually emit radiations in a wavelength range depending on the temperature and its emissivity, which is the wavelength and material-dependent property. The electromagnetic radiation released from objects that have the temperature around room temperature (300 K) is the specific interest of IR detectors because of the fact that most of the radiation emitted from these objects have a wavelength that is in the IR range.

Before starting to discuss the properties of infrared detectors, it is welcomed to define some of the concepts commonly used in infrared terminology. These concepts are either the general concepts that help to understand infrared basics or the parameters to characterize infrared devices.

2.1. Blackbody Radiation

Continually emitted electromagnetic radiations from objects that have a temperature above 0 K is absorbed by other matters. In other words, the emitted electromagnetic waves are absorbed by other objects. Besides with this feature, it is understood from the Maxwell's Law that a charged particle causes energy to be released when it is accelerated [20]. By relating this law with the thermodynamic approach, excitation in molecular level increases even a slight change in temperature occurs, and this causes charged carrier to accelerate resulting in generation of radiation. The relation in between emitted radiation and its wavelength is given as,

$$E = \frac{hc}{\lambda} \tag{2.1}$$

where λ is the wavelength, h is the Planck's constant, and c is the speed of ligth. By substituting Equation (2.1) for usual practice, and to use eV for energy and μm for wavelength, Equation.(2.1) becomes

$$E\ (eV) = \frac{1.24}{\lambda\ (\mu m)} \tag{2.2}$$

By using either Equation. (2.1) or Equation. (2.2), the bandgap of energy, which is required for the desired wavelength, can be obtained.

The emission and the absorption of electromagnetic waves are continuous processes. Moreover, good absorbers are also known as good emitters, meaning that

$$\alpha = \varepsilon \tag{2.3}$$

where ε is the emissivity, and α is the absorbance.

It should also be stated that all objects subjected to the incident radiation undergo several processes like absorption, reflection, and transmission.

From the Kirchhoff's Law of thermal radiation,

$$\alpha + \rho + \tau = 1 \tag{2.4}$$

where α is absorbance, ρ is reflectance, and τ is transmittance.

The absorbed energy is re-emitted from objects which are at equilibrium, and this process is called blackbody radiation. The "blackbody", introduced first by Gustav Kirchhoff in 1860, is defined as the object that absorbs all incident electromagnetic radiation regardless of the frequency and the angle of incidence. Then, emissivity is given as the exitance of an object per blackbody exitance at the same temperature and the same wavelength.

$$Emissivity\ (\varepsilon) = \frac{M_{object}}{M_{blackbody}} \tag{2.5}$$

The characteristic of blackbody radiation is stated by Planck's Law, and according to the Planck's law;

$$M(\lambda, T) = \frac{2\pi hc^2}{\lambda^5} \frac{1}{\exp\left(\frac{hc}{\lambda kT}\right) - 1} \tag{2.6}$$

where λ is the wavelength, c is the velocity of light, h is the Planck's constant, k is the Boltzmann's constant, and T is the absolute temperature of blackbody. The unit is $\mathrm{W/(cm^2 \cdot \mu m)}$. The relation between spectral radiant exitance $M(\lambda, T)$ and spectral radiance $L(\lambda, T)$ is known as;

$$M(\lambda, T) = \pi . L(\lambda, T) \tag{2.7}$$

Therefore, Equation (2.7) is also defined in terms spectral radiance as;

$$L(\lambda, T) = \frac{2hc^2}{\lambda^5} \frac{1}{\exp\left(\frac{hc}{\lambda kT}\right) - 1} \tag{2.8}$$

Then, unit becomes $\mathrm{W/(sr \cdot cm^2 \cdot \mu m)}$. The blackbody spectral emittance and blackbody spectral radiance for different temperatures are shown in Figure 2.1.

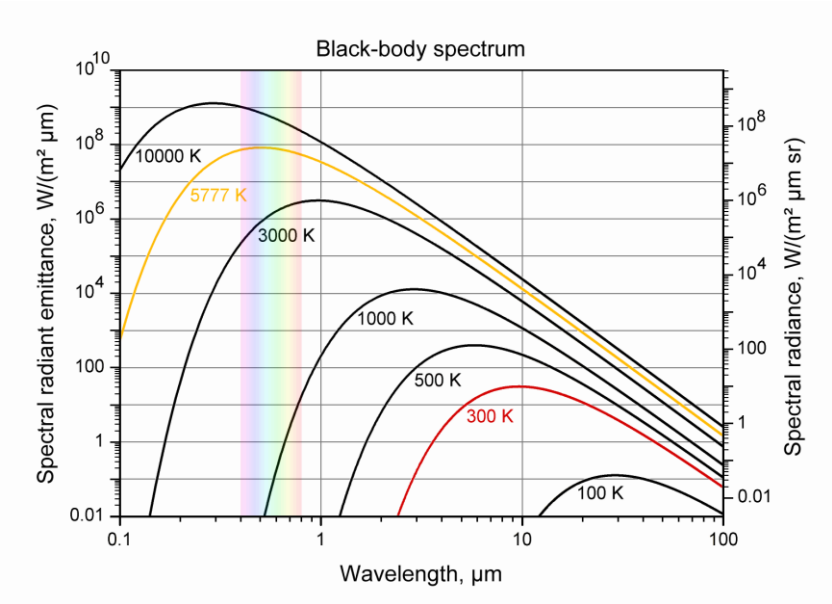

Figure 2.1. Blackbody spectral radiant emittance and spectral radiance for different temperatures [21].

When the temperature of an object is increased, the wavelength of the peak emittance shifts toward lower wavelengths.

From the Planck's Law, it can be easily understood that the spectral radiance of blackbody is not directional function; thus, a perfect blackbody is a Lambertian Radiator.

With this point of view,

$$\lambda_{peak} = \frac{2898\ \mu m.K}{T} \equiv \frac{b}{T} \tag{2.9}$$

where b is the Wien's constant (μm. K), and T is the absolute temperature in K. This is called Wien's displacement law. Wien's displacement law relates peak emittance wavelength with temperature.

The total exitance of a blackbody at given temperature is obtained by integrating Planck's Law through all wavelengths meaning that $\lambda = 0$ to $\lambda = \infty$. This relation is called Stefan-Boltzmann Law This law was first deduced by Josef Stefan in 1879, depending on experimental measurements, and it was theoretically derived by Ludwig Boltzmann in 1884 by using laws of thermodynamics.

$$M_{total} = \sigma.T^4 \tag{2.10}$$

where $\sigma = 5.67 \text{ x } 10^{-8}\ \mathrm{W/m^2K^4}$ is the Stefan's constant, and T is the temperature of blackbody. This equation enables to understand the strong temperature dependence of radiant power.

Due to their transparent and reflective properties, ordinary objects do not follow perfect blackbody conditions. Emissivity property of materials characterizes the disturbance from perfect blackbody conditions.

2.2. Atmospheric Transmission

In most cases, atmosphere plays a vital role in IR applications. Moreover, the propagation medium for blackbody radiation is air, except for the astronomical applications. The role of the atmosphere can be divided into two groups as emission processes and attenuation processes. Emission processes are caused by which atmospheric radiation interfere with the object's radiation, mostly in conditions of atmospheric radiation becoming important. Emission processes consist of noise-source property of atmosphere. Attenuation processes are mostly composed of

absorption and scattering phenomenon. Radiation propagating through the atmosphere is subjected to absorption, generally caused by gas molecules, and scattering caused by particles. The content of gas molecules and particles in the atmosphere changes with the weather conditions, sea level, that is, altitude, and humidity. Therefore, atmospheric transmission depends on these conditions.

The absorption process also leads to IR region intervals which are created in accordance with the different transmission properties of different wavelengths. These wavelength intervals are known as IR bands. In Figure 2.2, the IR atmospheric transmission and respective molecules responsible for absorption are shown.

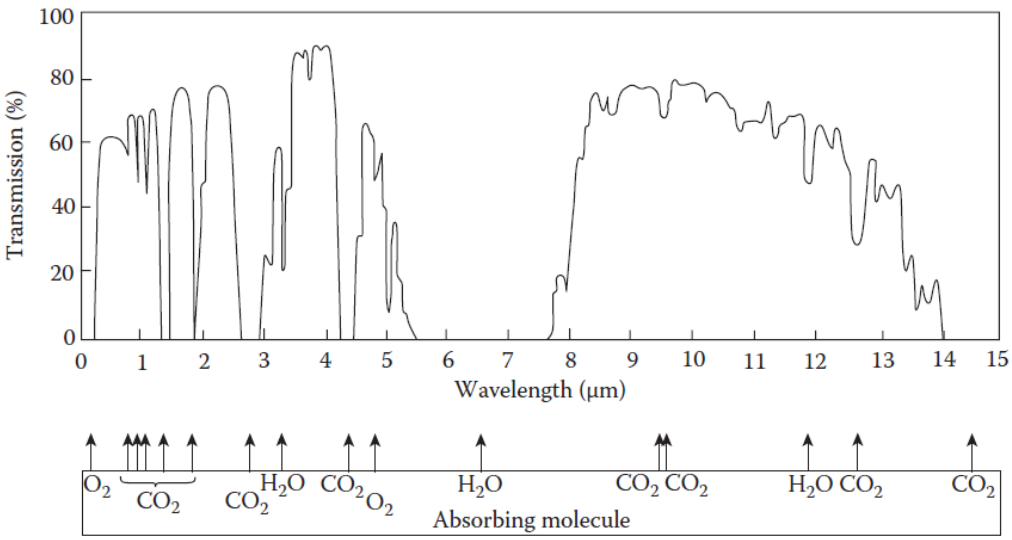

Figure 2.2. Atmospheric transmission and respective particles responsible for absorption [22].

The commonly used terms for IR regions and general properties of these band are as follows:

0.7 – 1.4 μm, Near-Infrared, (NIR): This region starts from the end of the visible region and continues up to 1.38 μm until the transmission is vanished by absorptions related to H_2O molecules. Fiber optics telecommunications and some imaging applications are important usage areas of this band.

1.4 – 3.0 µm, Short-Wavelength Infrared, (SWIR): Besides with H_2O molecules, CO_2 molecules play an important role in this region transmission properties. 1.55 µm is important for long-range telecommunication systems. The ~2.5-3.0 µm part of this region is the significant interval for night glow applications. The transmission in SWIR is better than VIS under fogy and hazy weather conditions.

3.0 – 8.0 µm, Mid-Wavelength Infrared, (MWIR): Significant contribution of radiation takes place in 3–5 µm part of this region. In fact, some sources end this window at 5 µm. The radiation emission from hot objects, such as engines, is main radiation source for this region. With the production and use of sensitive thermal detectors, passive imaging is possible.

8 – 12 µm, Long-Wavelength Infrared, (LWIR): This region is the most effective candidate for thermal imaging applications especially in long-range imaging. Objects having temperatures around 300 K emit the large amount of radiation, which belongs to this region. The main difference between LWIR and MWIR is that MWIR provides higher thermal contrast because of the thermal emission nature.

12 – 20 µm, Very Long-Wavelength Infrared, (VLWIR): When the temperature of an object decreases below the room temperature, photon flux naturally falls down in accordance with the decrease in the temperature. This region mainly deals with the low-temperature operations such as astronomical applications.

20 – 1000 µm, Far-Infrared, (FIR): It is possible to extend this region to larger wavelengths. Some astronomical applications dealing with very cold objects, Terahertz Lasers, and some medical issues are general interests of this region.

The importance of scattering effect on transmission through atmosphere depends on the band of interest. While scattering by particles having sizes smaller than the wavelength of incoming radiation is significant for visible region, it is un-important for other bands since their wavelengths are larger than the size of gas molecules.

Scattering caused by larger sized particles, also called Mie Scattering, depends more on weather conditions, and effect of this scattering should be considered in accordance with those conditions.

Mid-wave and long-wave windows of IR spectrum are the key regions, especially for ground base operations. MWIR and LWIR differ from each other in terms of requirements of an application. MWIR is more suitable for applications such that higher contrast is needed, and that humidity is considerably high for ranges exceeding 10 km. LWIR is the better choice for foggy and dusty conditions. Its scale is smaller than MWIR, and it provides better performance for ranges smaller than 10 km.

There are also several things to be considered before deciding the infrared band of operation. First of all, even if it is not directly related with spectral bands, whether the spectral emissivity of a target is high enough to operate in the band of interest should be considered because insufficient spectral emissivity may create difficulties for imaging.

Secondly, it can be easily obtained from Wien's displacement law (Equation (2.9)) that emitted radiation changes depending on the temperature of an object. Moreover, as the emitted radiation peak shifts towards shorter (or longer) wavelengths, an increasing portion of radiation can fall into a different band. Therefore, the temperature of the target objects and possible change in their temprature must be considered to increase the amount of incoming signal to the detector in the band of interest.

The atmospheric transmission, which is the actual reason for the existence of IR bands, is the other factor that affects the operation band decision in terms of imaging range.

Last but maybe most important consideration is thermal contrast. Thermal contrast can be interpreted as the measurement of a change in the emission of radiation in certain IR band when the temperature change.

The formula for thermal contrast can be shown as;

$$C_{\lambda_1-\lambda_2} = \frac{\frac{d}{dT}\int_{\lambda_1}^{\lambda_2} M(\lambda,T)}{\int_{\lambda_1}^{\lambda_2} M(\lambda,T)} \tag{2.11}$$

The thermal contrast comparison for a detector does not have to be in between different IR bands. It can also be from the same region of different cut-off wavelengths'. In this case, the one with lower cut-off wavelength would show larger thermal contrast. The limitation in detectors dynamic range, which is defined as the maximum temperature difference in a scene that a sensor can detect, is created by thermal contrast. The upper and lower limits, which are due to the saturation of readout capacitors, and signal to noise ratio being too low, respectively, should be considered. Thus, both thermal contrast requirements and dynamic range considerations must be taken into account for the determination of the IR band of operation [19].

2.3. Detector Types

Depending on effects of the incoming radiation on detecting material, IR detectors can be classified into two main groups:

- Thermal Detectors
- Photon Detectors

2.3.1. Thermal Detectors

The change in detecting material temperature due to incoming radiation causes a change in the material physical properties such as conductivity, transmission, polarization, and dimension. Thermal Detectors working principle relies on detecting the signal generated by the change in these physical properties and using this signal for the desired operation. Their direct dependence on the change in physical properties makes thermal detectors independent of incoming radiation and photons.

Thermal detection is a slow process since the time needed for changing the temperature of the device is large. As a result, the sensitivity and the response time are low in thermal detectors [22,23].

Table 2.1. Infrared Thermal Detectors [22]**.**

DETECTOR	METHOD OF OPERATION
Bolometer ▪ **Metal** ▪ **Semiconductor** ▪ **Superconductor** ▪ **Ferroelectric** ▪ **Hot Electron**	Change in electrical conductivity
Thermocouple/Thermopile	Voltage generation caused by change in temperature of the junction of the dissimilar materials
Pyroelectric	Change in spontaneous electrical polarization
Golay cell/gas microphone	Thermal expansion of gas
Absorption edge	Optical transmission of semiconductor
Pyromagnetic	Change in magnetic properties
Liquid crystal	Change in optical properties

The operation temperature of thermal detectors is around room temperature. Therefore, thermal detectors do not require cooling; thus, reduction in production cost is provided.

2.3.2. Photon Detectors

An interaction between an incoming photon and an active material electron, which can be either bounded to lattice atom or, if exists, impurity atom or free electron in material, sets up the main working principles of photon detectors.

With this interaction, energy is transferred from photon to electron, and it results in a change in the energy state of an electron. In other words, an incoming photon is absorbed, and the electron-hole pair is created in this type of IR detectors. Then, the electrical output is observed. In photon detectors, wavelength dependence is high since the photon energy should be enough to excite the electron to upper energy levels. From Equation (2.1), the energy of a photon can be obtained. Also, from this equation, the longer the wavelength of an incoming photon is, the less energy absorbed by an electron is, and in this case, the excitation requirement is not satisfied.

The output signal is gathered almost instantaneously in photon detectors since the lifetime of an excitation process is very fast. Besides with the optically excited electrons, the thermal excitation of electron takes place in photon detectors, especially for those working at lower energies ($\lambda > 2\ \mu m$). To suppress the thermal excitation of electrons, detectors should be cooled down. The cooling requirement of photon detectors makes them costly.

According to the energy transition modes, photon detectors can be divided into different groups such that extrinsic detectors, intrinsic detectors, and bandgap engineered detectors. The energy transition in extrinsic detectors takes place in between impurity states and conduction band with the absorption of an incoming photon. Extrinsic detectors are commonly fabricated by doping III or V group materials to create impurity states, and they are used for low background flux applications with very low operating temperature. The energy transition in intrinsic detector occurs in between valence band and the conduction band of the semiconducting material. An absorbed photon which has energy larger than the bandgap of semiconductor creates minority carriers and desired-electrical output obtained with the contribution of these minority carriers to conduction.

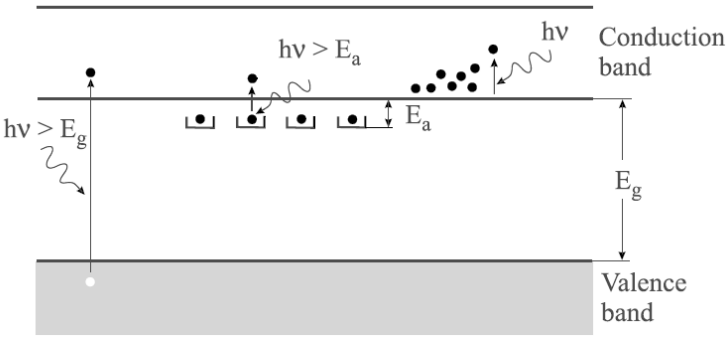

Figure 2.3. The energy transition in extrinsic and intrinsic detector structures [24]**.**

Besides with the fixed bandgap materials like InSb and InAs, the adjustable bandgap materials such as HgCdTe and InGaAs are common materials for intrinsic detectors

QWIP and Superlattice structures are the bandgap engineered intrinsic detectors which are structured by adding appropriate consecutive thin layers. In QWIP structures, the addition of multilayers creates confined energy states at conduction band. After absorbing an incoming photon, an electron is confined in these energy states. With the applicable operation, electrons are collected and contribute to the electrical output.

QWIP structures are one of the member superlattices. In superlattice structures; however, the artificial bandgap is created by deposition of multilayers consecutively. Superlattice structures are also divided into three groups:

Type-I Superlattice: QWIP structures. Commonly used materials for these structures are GaAs/AlGaAs.

Type-II Superlattice: Overlapping regions both in conduction and valence bands are artificially created. The thicknesses of layers are thinner than Type-I (QWIP) structures. Type-II Superlattice structures will be discussed in details in next chapter.

Type-III Superlattice: Commonly used materials for Type-III Superlattice are HgTe/CdTe. By flipping the valence and conduction band of semi-metal [8], these band-gap engineered structures are created.

Photon detectors are also divided into two main groups regarding the creation of electric field and the collection of a signal. The commonly used modes for photon detectors are photoconductive and photovoltaic modes. In the photoconductive mode, free carriers created by incoming radiation are collected by an externally applied bias voltage. Incoming radiation contributes to the conductance of a detector. The current generated by this way is called as photocurrent, and given as:

$$I_{photo} = q\eta w l \phi_s g_{photo} \tag{2.12}$$

where q is the charge of an electron, η is the quantum efficiency, w is the width of photoconductor, l is the length of photoconductor, ϕ_s is the incident photon flux density, and g_{photo} is the photoconductive gain, which is the material dependent property.

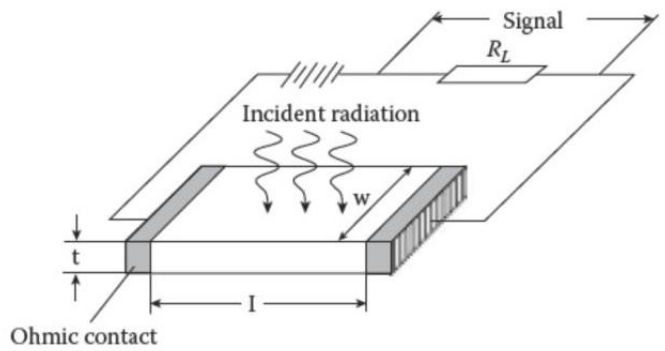

Figure 2.4. Photoconductor type detector operation [19].

In photovoltaic detectors, carriers, which are generated by absorption of an incoming photon, are collected by an internally created electric field like in p-n junction. In p-n junctions, while minority carriers generated in depletion region is swept one side of the junction by built-in electric field according to the polarity of charge (i.e., electron or hole), minority carriers generated within the diffusion length diffuse the other side of the junction. By this way, photo-generated carriers are collected, and they contribute to reverse leakage current.

The photocurrent in p-n junction can be given as:

$$I_{photo} = q\eta A\phi_s \tag{2.13}$$

where q is the charge of an electron, η is the quantum efficiency, A is the area of detector, and ϕ_s is the incident photon flux density. Figure 2.5 illustrates the schematic of p-n junction detection.

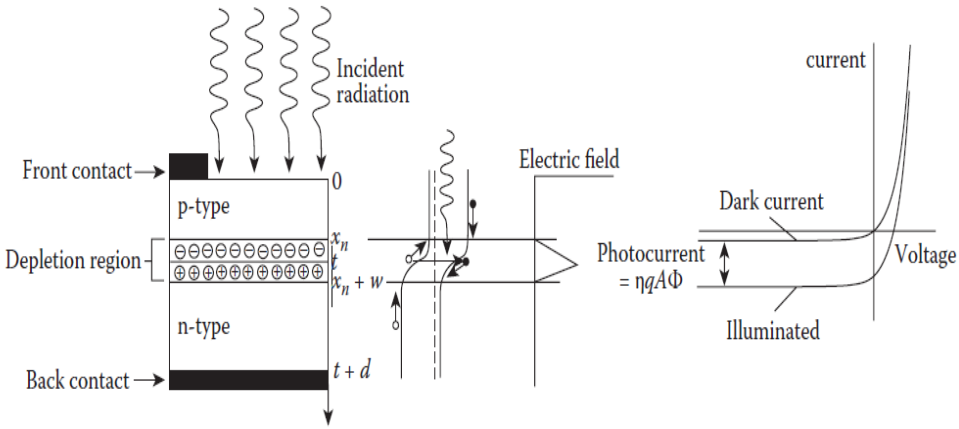

Figure 2.5. p-n junction photon detector operation [19].

After discussing detector types, infrared concepts that help to define characteristics and performance of IR detectors will be presented in next sub-section.

2.4. Figure of Merits

2.4.1. Quantum Efficiency (QE)

Quantum efficiency is the percentage of photons falling on the detector that can create electron-hole pairs (EHPs). It can also be thought as the electrical sensitivity of a detector to light. In the ideal case, quantum efficiency is 1 for all structures. However, in real cases, quantum efficiency is less than 1 due to the mechanisms which affect the absorbance of an electron and lead not to contribute photocurrent. Reflections from upper and lower surfaces of detectors and partially absorbance of incoming photons because of the inadequate thickness of absorption layer of detector lead to decrease in absorption of photons, even if the intensity of incoming photons remain

same. These mechanisms determine the external quantum efficiency of a sensor. Likewise, the generation-recombination mechanism, which causes the loss of EHPs before contributing photocurrent, and absorptions, which do not produce EHPs, are internally affecting mechanisms for quantum efficiency.

2.4.2. Noise

Noise is the undesired signal at the output. The existence of noise creates fluctuations in measured signal. Despite the fact that total elimination of noise is not possible, the primary focus is to keep the noise at a low level as possible such that Signal to Noise ratio (SNR) of the detector is high enough. $1/f$ noise, Johnson noise, shot noise, and generation-recombination (G-R) noise are some of the noise types experiencing on infrared detectors.

Johnson noise also called the thermal noise related to thermal fluctuations of the device when it is above the absolute zero temperature (0 K). It is represented as [22],

$$i_n = \sqrt{\frac{4kT\Delta f}{R}} \tag{2.14}$$

The optical and/or thermal generation processes create continuity in the generation-recombination process in semiconductor devices. This continuity and randomness of G-R process lead to fluctuations in output signals, and this is called Generation-recombination (G-R) noise. G-R noise current is defined as [22];

$$i_n = \sqrt{4qI_{total}g\Delta f} \tag{2.15}$$

where $I_{total} = I_{dark} + I_{photo}$. The photo current is given by;

$$I_{photo} = q\eta g\phi_p A \tag{2.16}$$

where ϕ_p is the photon flux density. The main goal of cooling a detector is to suppress the G-R noise.

The power spectral density of $1/f$ noise (also called pink noise) is inversely proportional to frequency. The origin of $1/f$ noise is not well understood yet. However, it is possible to encounter this type of noise in large variety of systems. The relation in between $1/f$ noise and dark current is discussed in many publications for low band gap semiconductors [25–27].

The randomness in the arrival of photons in a detector creates noise, and this noise is called as the shot noise. At low current levels, fluctuations in current due to random arrival of photons are comparable with average current [28]. In order to be shot noise observed, the device should be biased. It is independent of detector structure; and therefore, it can be considered as the lowest level of the detector noise.

When the shot noise is the dominant noise source, detector achieves its ultimate performance. That is to say, that noise level is limited only by background flux fluctuations. When detectors start to show this condition, the name "Background Limited Performance (BLIP)" is given for detector performance.

2.4.3. Responsivity (R)

Responsivity is the ratio of the output signal of the detector to input radiant power received by the detector. Responsivity can be shown as:

$$R = \frac{Signal\ Output}{Input\ Radiant\ Power} \tag{2.17}$$

It is possible to give the signal output either in amperes or volts. The radiant power is the total electrical power incident on the detector; and therefore, it is equal to

$$P = E.A_d \tag{2.18}$$

where E is the irradiance $\mathrm{Watt/cm^2}$, and A_d is the area of the detector (in $\mathrm{cm^2}$). The commonly used unit for responsivity is ampere/watt (A/W).

Even if having high responsivity is essential to reach high signal, it is not only phenomena to obtain good sensitivity for the system. The noise which is created by detector itself, meaning that internally, or externally (system related cases) plays a vital role in the goodness of sensitivity. The relation between the responsivity of a detector and incoming radiation wavelength, which detector is sensitive to, is summarized by the new form of spectral responsivity. The spectral responsivity is determined by a spectrum and a peak responsivity value. In the case that responsivity is characterized by a blackbody spectral radiant exitance, it is called blackbody responsivity. All the incident radiation is assumed to be absorbed by the detector for blackbody responsivity. However, the blackbody responsivity value should be stated by the blackbody temperature because spectral blackbody exitance depends on the temperature. Then, it is possible to give responsivity equation as follows,

$$R = q\eta g \frac{\lambda}{hc} \tag{2.19}$$

where q is the electron charge, η is the absorption quantum efficiency, and g is the photoconductive gain. Gain is defined as the ratio of the mean free path of the excited carriers to the total active layer thickness of the photoconductive detectors [8]. For photovoltaic detectors, gain is equal to 1.

2.4.4. Noise Equivalent Power (NEP)

The rise in radiant input power results in an increase in signal-to-noise ratio; thus, SNR is not constant. Therefore, defining the detector sensitivity with SNR is not exact means of it. The power equivalent to detector noise is the measure of detector sensitivity. The incident power required to produce SNR which equals to 1 is defined as Noise Equivalent Power (NEP).

$$NEP = \frac{i_{noise}}{R} \tag{2.20}$$

where i_{noise} is the noise of the detector, R is the responsivity of the detector.

2.4.5. Detectivity (D)

Detectivity is defined as the inverse of NEP. Physical parameters such as detector area and bandwidth of noise measurement affect detectivity (also NEP). These effects are coming from especially the existence of i_{noise}. The detectivity which is free from these kinds of physical parameters is called Specific Detectivity, and it is defined as;

$$D^* = \frac{R\sqrt{A_d \Delta f}}{i_{noise}} \tag{2.21}$$

The unit is $\mathrm{cm}\sqrt{\mathrm{Hz}}/\mathrm{W}$. This unit called with its inventor's name, Jones.

By assuming $I_{dark} << I_{photo}$, it is possible to interpret Equation (2.21) under BLIP conditions as

$$D^*_{BLIP} = \frac{\lambda}{hc}\sqrt{\frac{\eta}{\phi_{background}}} \tag{2.22}$$

2.4.6. Noise Equivalent Temperature Difference (NETD)

Responsivity and detectivity are generally used for characterization of single pixel performance. For an entire imaging system, a collection of pixels, a performance criterion is needed to emphasize the system performance. Therefore, new performance criterion is defined, Noise Equivalent Temperature Difference (NETD). NETD is the minimum temperature difference between an object and the background corresponding to noise in the system. The formula for the NETD can be shown as:

$$NETD = \frac{4\, f/\#^2 \sqrt{\Delta f}}{\sqrt{A}\int_0^\infty T(\lambda) D^*(\lambda) \frac{dM_{target}(\lambda)}{dT} d\lambda} \tag{2.23}$$

where

$f/\#$(f-number): The ratio of focal lens used in the imaging system to the aperture diameter.

Δf: The measurement bandwidth.

A: The area of detector.

$T(\lambda)$: The wavelength dependent atmospheric transmission.

$D^*(\lambda)$: The specific detectivity.

$M(\lambda)$: The spectral radiant power of the target.

2.4.7. Modulation Transfer Function (MRTD)

Modulation Transfer Function can be defined as the system resolution at its spatial frequency response. Like NETD, MTF is a system parameter. When imager resolves at a particular frequency, it should translate contrasts at that specific frequency. As the maximum resolvable spatial power getting higher, the sharpness of the image increases; hence, the image becomes sharper [19].

2.4.8. Minimum Resolvable Temperature Difference (MRTD)

Minimum Resolvable Temperature Difference is a system-level parameter that specifies not only spatial resolution but also the thermal sensitivity of the system. The standard test patterns standing over background are used in MRTD measurement for the minimum temperature difference which is visualized by an observer. Thus, MRTD measurements are observer dependent.

2.5. Imaging Concept

The imaging principles of each electromagnetic spectrum region differ from each other in terms of some fundamental features. Visible imaging depends on the reflection of light on surfaces in the scene, which external illumination and its reflection become important. However, an object having the temperature around

room temperature behaves like a source by itself, and any external illumination is not needed. This type of imaging is called thermal imaging, and it is passive. Systems which convert the electromagnetic radiation of a scene to electrical representation are defined as imagers [19]. The imaging flow can be summarized as incoming radiation is collected by optics and falls on a detector array which converts it to an electrical signal, and it is transported to readout integrated circuit (ROIC). Then, ROIC sends this signal to external electronics, and finally, the image is displayed. Each element of this flow shows different properties in accordance with which type of imaging is performed.

There are some relevant parameters that affect imaging regarding optics. The $f/\#$ defined as the ratio of the lens's focal length to the diameter of the image of the physical aperture stop in the entrance pupil. The amount of flux being transferred to the detector is determined by f-number. The relation between the radiant exitance M_e on the object plane and the irradiance E_e on the image plane is expressed as,

$$E_e = \frac{M_e}{4(f/\#)^2 + 1} \tag{2.24}$$

The minimum achievable spot size on the image plane is also determined by $f/\#$ according to following relation,

$$R_{Airry} = 1.22 \,.\, \lambda \,.\, (f/\#) \tag{2.25}$$

where R_{Airry} is the radius of the Airy disk, and λ is the wavelength of operation.

The concept of being resolved for the image is explained by the Rayleigh criterion which underlines that separation of two spots should be at least as the radius of the Airy disk. The f-number impacts on the imaging resolution by matching the spatial cut-off frequency of the optics to the Nyquist frequency of the FPA [29].

This requirement is met for an ideal pixel at

$$\frac{(f/\#)\,.\,\lambda}{d} = 2 \tag{2.26}$$

where d is the pixel pitch of FPA. However, diffraction plays an important role, and it determines the quality of image or imager. Moreover, the limit set by diffraction is a fundamental resolution limit, and systems operating at diffraction limit are called diffraction limited performance system. Aberrations, which are mostly related to design, material, and practical issues, are another resolution limiting factors. There is a trade-off between flux transfer and image quality since the effect of aberration on image quality decreases together with the decrease in f-number. Therefore, research and development studies are gathered around these limitations by optics designers in order to reach the diffraction limited performance.

2.6. Technology Comparison

Starting from the end of the 1940s and the beginning of the 1950s, attention to narrow bandgap semiconductors like InSb and HgCdTe (MCT) increased, and a lot of research was conducted on these semiconductors so as to understand the physical properties of them. After the first proposal of superlattice structures in 1970, QWIPs became another hot-topic-IR material. From those time to nowadays, these semiconductors finished their adolescence time, and their maturity age has started. Therefore, most of the commercially available FPAs are based on MCT, InSb, and QWIP for MWIR. In this section, comparisons of each technology in terms of their advantages and disadvantages will be discussed.

$Hg_{1-x}Cd_xTe$ (MCT) is the combination of HgTe and CdTe semimetals. MCT has a direct band gap, and the energy gap of this ternary compound semiconductor can be adjusted by changing the mole fraction of cadmium to mercury. Furthermore, the energy gap of it depends on operating temperature. Commonly used substrate for epitaxial growth of MCT is another ternary compound, Cadmium Zinc Telluride (CdZnTe or CZT). MCT and CZT have lattice constants which are very close to each

other. Moreover, change in Cd mole fraction to define operational wavelength do not significantly affect the lattice constant of MCT. MCT have large absorption coefficient resulting in high quantum efficiency. The recombination mechanism of MCT enables to operate higher temperatures. However, the dark current of MCT is relatively large due to small electron mass resulting in tunneling. Besides, the high cost of CZT, difficulty in reproducible growth, non-uniformity over the entire area, un-availability of large area substrates, and large defect densities limit the high-quality material production. Although alternative substrates like Si, CdTe buffered Si, and GaAs are tried to overcome these issues, their large lattice mismatch with MCT reveals other problems.

Another commonly used material for the mid-infrared spectral range is Indium Antimonide (InSb). InSb has a direct and fixed bandgap. Therefore, the operational infrared window is limited in between 3 to 5 μm interval. InSb can be grown on single InSb crystal. The p-n junction operation of InSb is provided by changing the ratio of In to Sb. Increase in In makes material p-type, while n-type material supplied by using more Sb. The energy gap of InSb varies with temperature. While it is equal to 0.23 eV at 77 K, which corresponds to MWIR response cut-off around 5.5 μm, it is equivalent to 0.17 eV at room temperature corresponding to LWIR response cut-off wavelength 7.0 μm. However, between 5.5 μm and 7 μm, there is no infrared radiation because of atmospheric transmission, mentioned in Section 2.2. Generally, the working temperatures of InSb detectors are below liquid nitrogen temperature (77 K), and they are around 60-80 K. However, InSb detectors are used in ground-base astronomy, and astronomical applications require low operation temperature like 4-7 K to lower noise. Because of the decrease in minority carrier lifetime in the n-type material at lower temperatures, they exhibit low quantum efficiency at those temperatures.

Quantum Well Infrared Photodetectors (QWIPs) are one of the branches of III-V material groups. High yield to low cost, mature material growth, and device processing techniques of QWIP technology besides with steady growth over large areas make them essential material for mid-infrared detection. Moreover, the energy

gap of OWIP can be adjusted for desired IR windows by differentiating consecutive layers' thicknesses. As this opportunity provides detection in MWIR and LWIR windows, QWIPs can be operated at both MWIR and LWIR with dual color operation designs. However, QWIPs are insensitive to surface to normal incident infrared radiations because of the polarization selection of electron-photon interaction. Hence, the quantum efficiency of QWIP is low. Diffraction gratings are generally used either on the bottom or the top of QWIPs to enhance quantum efficiency. The excited electrons are gathered under illumination by applying bias voltages which decreases the barrier potential, and photo-generated current is sensed. Relatively high dark current levels lower the operational temperature of QWIPS, and they work around 60 K. The necessity of low operation temperature increases the cost of the device.

Each detector technology has advantages and disadvantages according to own properties. To eliminate or to emasculate drawbacks and to enhance benefits, the pursuit for a new type of infrared devices which give higher performance than currently available ones has started, and Type-II superlattices are the strongest candidate for this position. Type-II Superlattice Technology will be investigated in following chapter, which begins with the history of them, followed by theoretical considerations, and finalized with recent developments in this technology.

CHAPTER 3

TYPE-II SUPERLATTICE TECHNOLOGY

The necessity to be named as the third generation of infrared detectors does not only depend on the type of material used in IR system but also detectors should provide some features. High thermal contrast, high sensitivity, large format detectors with high uniformity, small pixel size, high operability, high-temperature operation, low cooling and power requirements, multi-spectral operations, and low cross-talk are the requirements of the 3rd generation IR systems. Today, most of the commercial FPAs are either based on MCT, InSb or QWIP for entire infrared spectrum. However, as it is mentioned in Section 2.6, each of these technologies has unique drawbacks. High cost, unavailability of large area substrate, and difficulty in repeatability of material growth make MCT thrown the background even if its properties suits for the 3rd generation. Likewise, relatively low quantum efficiency and fixed energy band features of QWIPs and InSb, respectively; create requirements for an alternative material for the 3rd generation IR operations. Therefore, a new type of bandgap engineered devices should be provided.

The robustness of material, the ability to operate almost entire infrared region, the weak dependence of band gap with operating temperature, and having close lattice constants properties of Sb-based materials make InAs/GaSb Type-II superlattices suitable candidate for new generation IR systems.

By adjusting the thicknesses of individual layers, the cut-off wavelength of the device can be tolerated in T2SLs. Moreover, T2SLs gain advantages in terms of uniform performance over a large area and low cost. T2SL technology has matured over the years. The historical development of type-II superlattice structures will be given in next section.

3.1. History of Type-II Superlattices

After the proposal of superlattice by Esaki et al. [10] in 1970, the idea of broken bandgap and Type-II superlattices were considered as new infrared imaging approaches in between 1977-1979. The theoretical structure was in the form of bilayer superlattices, which have lower conduction band (CB) edge located in one material, while higher valence band (VB) edge located in other material. With this structure, the localization of the wave functions of the lowest conduction subband and the highest valence subband are in two different semiconductors. This gives opportunity that the conduction and the valence band edges can be tuned independently, shown in Figure 3.1. The closely lattice matched semiconductors InAs/GaSb or InGaAs/GaSbAs was the suitable candidates for this structure.

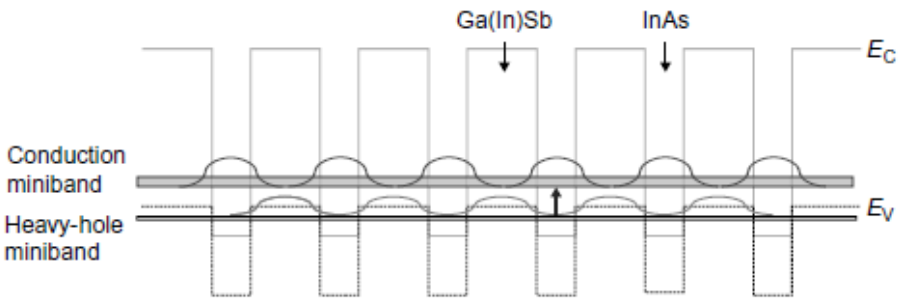

Figure 3.1. Schematic illustration of an InAs/Ga(In)Sb type-II broken-gap superlattice showing the spatial separation of the conduction band and the heavy-hole band wave functions. The infrared transition is indicated by an arrow [30]**.**

The broken-gap alignment between InAs and GaSb first noticed by W.Frensley [31], and the sophisticated theoretical model was suggested by Harrison in 1977 [32]. Although Harrison did not mention about the broken-gap alignment, W.Frensley pointed out the intersubband tunneling transport property. In following year, the

collaboration of Harrison, Sai-Halasz, and Esaki revealed that thin layered InAs/GaSb superlattices have well-defined energy band-gaps and behave like a semiconductor, whereas thick-layered superlattices of InAs/GaSb act as semimetals. This realization facilitates that the band gap of InAs/GaSb superlattice can be set up arbitrarily small, even smaller than each of InAs and GaSb.

Initial studies for infrared detection with superlattice structures were conducted on HgCdTe (MCT) material systems. In literature, MCT based superlattice structures, a combination of HgTe and CdTe, are sometimes called Type-III superlattices. Research on MCT based superlattices showed that some of their properties such as p-side diffusion current, reduced band-to-band tunneling, and weak dependence of cut-off wavelength to composition alloy were found in InAs/GaSb superlattice, as well. However, Chang and Schulman [33] calculated the optical properties of InAs/GaSb superlattices in 1985. They realized that the oscillator strength of optical transition was approximately proportional to $1/MN$, and it decreased rapidly with layer thicknesses, where M and N were the number of InAs and GaSb monolayers in each period, respectively. The meaning of this was that much of the volume was inactive in InAs/GaSb superlattices with long periods. Therefore, in 1987, the first strained layer superlattices was proposed by Smith and Maihiot [34]. They offered InAs/GaInSb strained layer superlattices by using tensile and compressive strains of InAs and GaInSb, respectively, in order to lower InAs conduction band edge and to raise GaInSb heavy-hole (HH) band edge resulting in deeper quantum wells for each band (Figure 3.2). They also stated that GaSb was well-chosen substrate for InAs/GaInSb superlattices growths. In 1990, Miles et al. experimentally showed LWIR absorption of InAs/GaInSb strained layer superlattices [35]. From 1991 to 1994, experimental studies were performed on the identification of electron mass and auger lifetime of strained superlattices. Moreover, some fundamental researches on InAs/GaSb superlattices including theoretical calculations about electronic and optical properties of InAs/GaSb were performed. In 1998, Prof. Razeghi and her group published an article about InAs/GaSb superlattice [36].

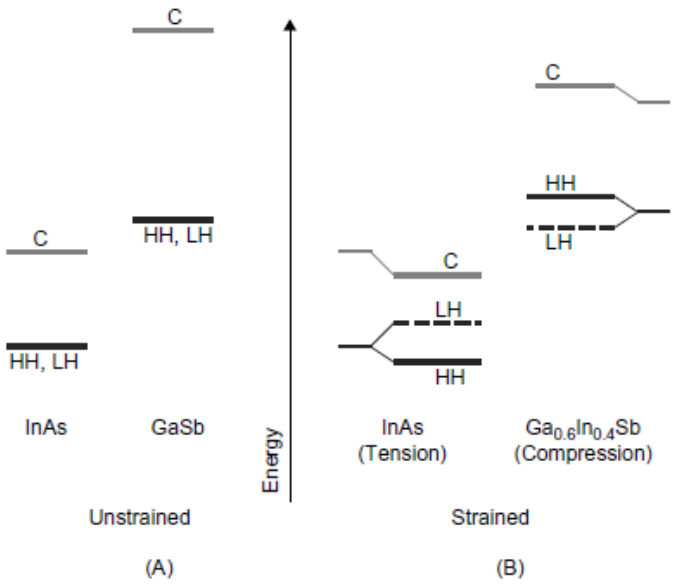

Figure 3.2. Band edge energy positions for (A) unstrained InAs and GaSb and (B) strained InAs and $Ga_{0.6}In_{0.4}Sb$ in a free-standing InAs/GaInSb superlattice [30]**.**

They stated that because of the higher joint density states than bulk semiconductors, InAs/GaSb superlattices had a sufficiently large absorption coefficient even if they had weak oscillator strength. Although InAs/GaSb superlattices consist of unstrained or minimally strained layers, caused by the slight lattice mismatch (0.6%) between InAs and GaSb, they also have advantages over strained ternary semiconductor GaInSb.

From 1996 to 2005, superlattice technology development period started to alter its form, and first-generation high-performance detectors and FPAs had been fabricated. Fuchs's et al. [37] and Johnson's et al. [38] works triggered the new development period of superlattices. In this period of time, growth, design, fabrication, and characterization techniques for superlattices improved, and significant progress was recorded. In order to optimize and understand the growth conditions, lots of experiments were done, and it was one of the major achievements during this period [39–42]. There were also studies related with alternative substrates like GaAs since commonly used GaSb substrates, having closely lattice matched to InAs/GaSb superlattices, suffered from high defect density, poor surface morphology, high cost,

and limited size [43,44]. In addition to this, studies about material property and characterization with new methods were analyzed [36,45].

The recent developments from 2006 and up to now have focused on reducing dark current, increasing quantum efficiency, and fabrication of large format, small pixel size arrays. Heterojunction detector designs have been dramatically effective for improving detectors performance. The nBn [46], pBp [47] and Xbn [48] designs were suggested. Moreover, besides with the single band nBn detectors [49], dual-band nBn detectors [50] and pBn detectors [51], double heterojunction structures like in Nguyen et al. [52] and in Vurgaftman et al. [53], p-π-M-n detectors [54], PbIbN structure [55], and CBIRD design [56] have been popular designs for superlattice structures. The complex superlattice cell designs have combined with heterojunction designs, either as a barrier or as an absorber, and they were named as W and M shapes. Since superlattices are still hot topic and promises higher performance, lots of studies have been conducting on these structures; thus, it is impossible to give the details of these large numbers of studies individually.

There has been continuous effort to improve T2SL detector performances all over the world even T2SL structure has revealed remarkable results. FPA level performance of fabricated T2SLs by different groups and their detector's results will be presented in Section 3.3.

Before starting latest developments in T2SL, it is more convenient to give some of the significant features of type-II superlattices. Therefore, in the following section, the basic properties of T2SLs will be handled.

3.2. Basic Properties of Type-II Superlattices

The InAs/GaSb T2SL structures are defined by a broken-gap type-II alignment as stated in the previous section. The schematic illustration of band alignment of type-II superlattices is shown in Figure 3.3.

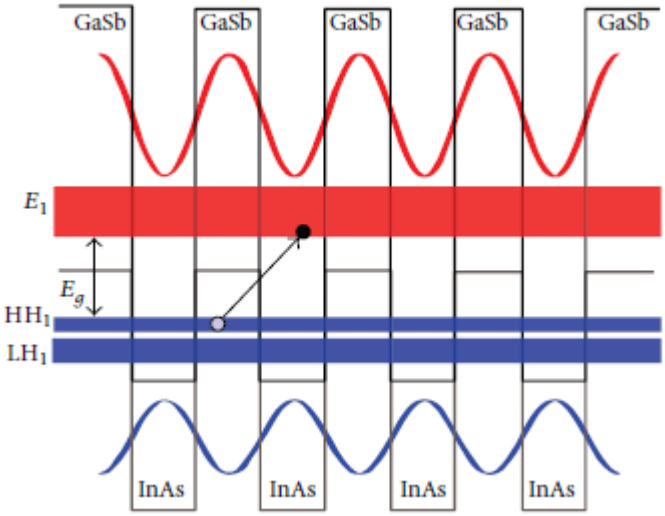

Figure 3.3. The schematic illustration of broken-gap type-II alignment [57].

As shown in Figure 3.3, electron and hole wavefunctions have maximas in InAs and GaSb, respectively. Electron and hole minibands are formed by the overlapped electron and hole wavefunctions between consecutive InAs and GaSb layers. Infrared radiation is sensed by the optical transitions between the highest; that is, heavy-hole miniband and the lowest conduction miniband. The decrease in the layer thicknesses increases the wavefunctions overlapping; hence, it causes more favorable optical absorption. When thicknesses exceed 5 nm, the wavefunction overlap is reduced with the corresponding decrease in the optical coupling. Moreover, cut-off wavelength is adjusted by varying the thicknesses of InAs and GaSb layers. The working principle of T2SLs depends on the transition of electrons in depletion region from the valence band to conduction band, by absorbing energy from incident infrared radiation, and transportation of these electrons by the built-in electric field to the n-type electrode while holes are transported to the p-type electrode.

3.2.1. 6.1Å Material System

In 2004, Kroemer [58] referred closely lattice matched materials like InAs, GaSb, and AlSb as the 6.1 Å material system since they have lattice constants approximately equal to 6.1 Å (Figure 3.4).

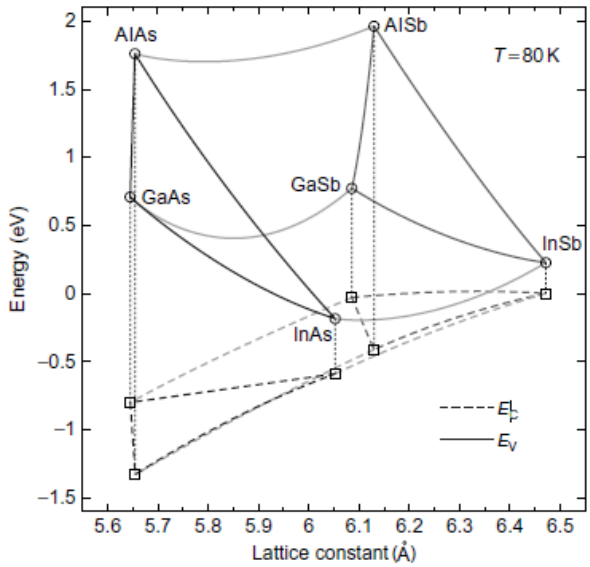

Figure 3.4. Zone center (Γ-point) conduction and valence band edge positions plotted against lattice parameter for antimonide, arsenide and arsenide-antimonide III-V semiconductors [30]**.**

The members of this material system show similar properties and occupy a strong position in the infrared world. Despite their intermediate material robustness, they have an ability to show strong normal-incidence to bulk GaSb resulting in band-to-band absorption for high quantum efficiency. GaSb has a direct band gap in SWIR, InAs in MWIR, and InAs/GaAs superlattices in SWIR, MWIR, and LWIR. Furthermore, the phonon scattering caused by intersubband absorption mechanisms in the detector is avoided with the valence-to-conduction band infrared absorption mechanisms. In addition to this, having close lattice constants decreases the number of impurities, which are another important phonon scattering sources, in the crystal. Therefore, phonon scattering is less in InAs/GaSb type-II superlattices. Phonon scattering limits the operating temperature of the detector. The property of showing less phonon scattering increases the operating temperature of T2SLs.

3.2.2. Tunneling Effect

It is known that the tunneling effect in infrared photodiodes is under the control of evanescent waves in the band gap. This case is also valid for InAs/GaSb T2SLs. Intentionally created strain InAs layer to GaSb substrate cause slight splitting of

heavy and light hole bands of InAs. The evanescent waves or states responsible for tunneling leakage are connected to conduction band edge and light hole band edge. There have been different models to explain or to investigate this situation resulted merely in that the evanescent waves propagate in accordance with $e^{(-|k_z|z)}$ or $e^{(|k_z|z)}$, where $|k_z|$ is an imaginary quantity. In general, the magnitude of the imaginary wave vector is larger in semiconductor with larger band gaps. That is to say that, reduction in tunneling can be obtained with larger conduction band effective mass. In addition to this, the smaller imaginary wave function is the main tunneling related problem in small band gap structures. As a result, the larger electron effective mass is crucial for reduction of tunneling effects like band-to-band tunneling and trap-assisted tunneling.

3.2.3. Auger Recombination

Auger recombination is the recombination of an electron and a hole in band-to-band transition in which released energy is transferred to another electron and hole. It differs from band-to-band recombination because of involving the third particle, which affects the recombination rate. There are different types of Auger process, and one of them is the Auger 1. The Auger 1 process, which occurs in n-type material, is the recombination of an electron and a minority carrier hole. In this process, energy and momentum are conserved by transferring them to another conduction band electron. The Auger 7 process, which is the primary Auger process in p-type materials, is the recombination of a heavy hole and a minority carrier electron. In Auger 7, the conservation of energy and momentum is provided by trading them with a light hole. In T2SL structures, the Auger 7 process is suppressed in n-type by the band splitting of the heavy hole (HH1) and light hole (LH1) because of intentionally induced strain. Auger 7 process materializes as the excitation of a hole from HH1 to LH1 for the rule of energy and momentum conservation, in p-type material. However, the occupation of hole state of LH1 in the low energy band gap T2SLs is infrequent because its location is just below the valence band maximum in 50-100 meV interval. Thus, the Auger recombination is constrained in InAs/GaSb T2SLs, and this provides to have longer carrier lifetime and higher quantum efficiency.

3.2.4. Dark Current Mechanism

The dark current mechanisms for an infrared detector can be expressed as

$$I_{total} = I_{diff} + I_{gr} + I_{btb} + I_{tat} + I_{shunt} \tag{3.1}$$

where I_{diff} is the diffusion current; I_{gr} is the generation-recombination current; I_{btb} is band to band tunneling current; I_{tat} is trap-assisted-tunneling current, and I_{Rshunt} is the dark current that is due to the shunt resistance of semiconductor. Shunt current originates from surface and bulk leakage currents which are valid in reverse bias region. Except for I_{Rshunt}, the others are the main mechanisms.

In previous sections, the effect of tunneling and Auger mechanisms discussed, and it is clarified that the band-to-band tunneling, trap-assisted tunneling, and Auger recombination mechanisms are constrained in type-II superlattices. Therefore, in this section, the main purpose is to give basic properties of other dark current mechanisms encountered in T2SL structures.

The diffusion current originates from thermally generated carriers within un-doped or un-intentionally doped SL region of the detector. The contribution of minority carriers is larger than majority carrier's concentrations under reverse bias operation. The diffusion current density (J_{diff}) can be expressed as [59]

$$J_{diff} = n_i^2 \sqrt{q k_B T} \left(\frac{1}{N_D} \sqrt{\frac{\mu_h}{\tau_h}} + \frac{1}{N_A} \sqrt{\frac{\mu_e}{\tau_e}} \right) \left(e^{\frac{qV}{k_B T}} - 1 \right) \tag{3.2}$$

where n_i is the intrinsic carrier concentration; q is the electron charge; k_B is the Boltzman constant; N_A is the p-type doping concentration; N_D is the n-type doping concentration; μ_e and τ_e is the mobility and lifetime of electrons, respectively; μ_h and τ_h is the mobility and lifetime of holes, respectively. The diffusion current can be suppressed by cooling the detector. In fact, this is the reason for cooling requirements of infrared detectors.

The generation-recombination current originates from thermally activated transitions via Shockley-Read-Hall (SRH) defects in depletion region [60]. Under reverse bias, the generation-recombination current density based on SRH can be given as [61]

$$J_{gr} = \frac{qn_i w}{\tau_{gr}} \frac{2k_B T}{q(V_{bi} - V)} \sinh\left(-\frac{qV}{2k_B T}\right) f(b) \tag{3.3}$$

where $f(b) = \int_0^\infty 1/(x^2 + 2bx + 1)\, dx,$ where $b = \exp(-qV/2kT)$, w is the depletion width; τ_{gr} is the carrier generation recombination lifetime in depletion region, V_{bi} is the built-in voltage of detector, and V is the applied voltage.

When the detector is cooled down; diffusion current decreases faster than G-R current. As a result, G-R current starts to dominate the dark current at certain temperatures. The suppression of G-R current can be obtained by designing unipolar barrier structures in T2SLs. A larger band gap material is inserted to depletion region of the p-n diode. By this way, the SRH dark current generation is eliminated because G-R current is proportional to $\exp(-qV/2kT)$, and this factor is dramatically reduced by inserting larger band gap material as a barrier. Today, most of the T2SL detector structures include barrier design. Due to suppression of G-R dark current, detectors can operate at higher temperature with higher sensitivity; and thus, cooling power and consequently cost are reduced.

The trap-assisted tunneling under uniform electric field can be expressed as [52]

$$J_{tat} = \frac{\pi^2 q^2 m_T M^2 N_T V}{h^3 (E_g - E_T)} \exp\left(-\frac{8\pi\sqrt{2m_T (E_g - E_T)^3}}{3qhE(V)}\right) \tag{3.4}$$

where N_T is the activated trap density; E_T is the trap energy location below the effective conduction band edge (generally $E_T = 1/2E_g$), and M^2 is the matrix element associated with the trap potential.

The direct tunneling of carriers from the valence band to the conduction band of heterojunction from one side to other side is called band-to-band tunneling current. It is generally observed at large reverse bias voltages due to the higher probability of band alignment. The band-to-band tunneling current density can be expressed as [52];

$$J_{btb} = \frac{q^3 E(V) V}{h^2} \sqrt{\frac{2m_T}{E_g}} \exp\left(-\frac{8\pi\sqrt{2m_T E_g^3}}{3qhE(V)} \right) \tag{3.5}$$

where $E(V)$ is the electric field; h is the Planck's constant; m_T is the tunneling effective mass, and E_g is the bandgap.

Band-to-band and trap-assisted tunneling dark currents are reduced in T2SL structures, which is mentioned in Section 3.2.2, briefly by having larger electron effective mass.

The last dark current mechanism is the shunt resistance current. It commonly expressed as the addition of surface leakage current and ohmic shunt current. The common expression for J_{shunt} is as follows;

$$J_{shunt} = \frac{V}{R_{shunt} A} \tag{3.6}$$

where V is the applied voltage; R_{shunt} is the detector shunt resistance, and A is the junction area.

It is possible to reduce the shunt dark current component with mature process techniques. To illustrate, adequately formed mesas, which significantly affect the leakage current due to the increased number of bonds over mesa sidewalls, can decrease shunt current. In fact, the shunt dark current can be reduced by properly isolated mesas.

After given fundamental properties of Type-II Superlattices, the recent developments on these structures will be presented in next section.

3.3. Recent Developments

The first superlattice FPA was demonstrated in 2005 by Walther et al. [62]. It was 40 μm pitch 256 x 256 MWIR FPA having cut-off wavelength 5.4 μm. Moreover, FPA yielded quantum efficiency of 30 %, detectivity values exceeding 10^{13} Jones at T=77 K, and NETD of 11.1 mK for an integration time of 5 ms using $f/2$ optics. In 2007, Fraunhofer IAF showed their 4.9 μm-cut-off-wavelength array with 27.9 mK NETD [63]. Again in 2007, NWU illustrated 25 μm pitch 320 x 256 FPA having 12 μm cut-off wavelength with 340 mK NETD [64]. Same year JPL and Raytheon presented 256 x 256, having 10.5 μm cut-off wavelength p-i-n detectors [65]. In 2008, 256 x 256 MWIR FPA based on a type-II InAs/GaSb superlattice detector with an nBn design was exhibited by Kim et al. [66]. In the same year, Plis et al. manifested 24 μm pitch 320 x 256 FPA which has 4.2 μm cut-off wavelength, 23.8 mK NETD with 16.3 ms integration time, and $f/4$ optics.[67], shown in Figure 3.5.

Figure 3.5. Thermal image of 320 x 256 InAs/GaSb SLs nBn design at 77 K with 16.3 ms integration time [67]**.**

In 2011, Walther et al. validated their dual color (dual band) FPAs in 288 x 384 format and 40 μm pitch [68]. While one channel, which works in a wavelength range 3-4 μm, gave 18 mK NETD at 84 K with 1.5 ms integration time and $f/1.5$ optics, the other channel, which works in 4-5 μm wavelength interval, revealed 10 mK NETD at same conditions. The image acquired by this FPA is shown in Figure 3.6.

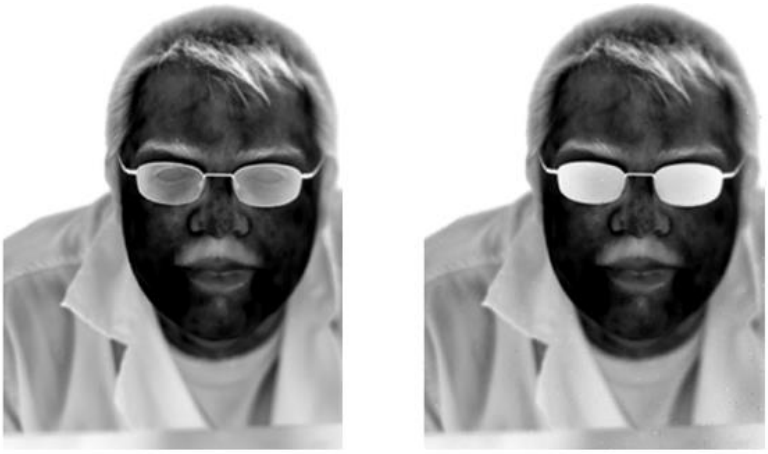

Figure 3.6. Left image 3-4 µm channel, right image 4-5 µm, white indicates colder region [68].

The heterojunction designed 640 x 512, 15 µm pitch FPA was fabricated in 2013 by Martijn et al. [69]. Their FPA had 5 µm cut-off wavelength, and it had 65 % quantum efficiency without anti-reflection coatings. Furthermore, their dark current density at 120 mK was relatively acceptable when it was compared to literature, and it was equal to $3x10^{-6}$ A/cm^{-2} at -0.05 bias. The NETD value that they obtained was not impressive according to the results reported in literature, 41 mK at 90 K with 21 ms integration time, and $f/4$ optics (Figure 3.7).

Figure 3.7. 640 x 512 15 µm pitch FPA images at 90 K [69].

In 2014, Katayama and others showed their FPA which had 6 µm cut-off wavelength [70]. The FPA was in 320 x 256 format with 30 µm pixel pitch. They obtained higher NETD value than Martijn FPA, 250 mK with $f/2.3$ optics and 200 µs integration time at 77 K (Figure 3.8).

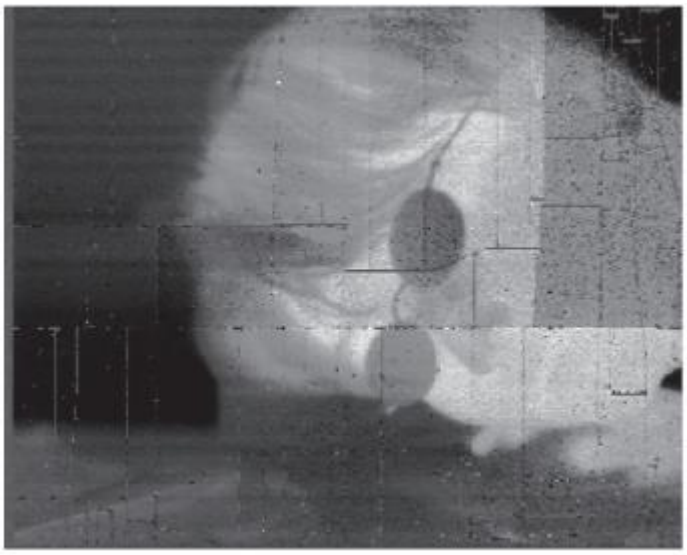

Figure 3.8. Image of 6 µm cut-off wavelength [70]**.**

Razeghi and co-workers, in 2015, presented pMp design T2SL FPA having 27 µm pitch in 320 x 256 format. They obtained peak responsivity at 4.2 µm with a value of 2.4 A/W, and their quantum efficiencies at peak responsivity was 68.6 % [71].

Figure 3.9. The images taken at different temperatures, from 81 K to 150 K [71]**.**

Their detectivity value was equal to 3.5 x 10^{11} Jones, and their NETDs were 11 mK at 81 K and 15 mK at 110 K (Figure 3.9). In 2016, Miura et al. published an article

about their last FPA (Figure 3.10). Their FPA had following properties: p-i-n design, 320 x 256 format, 30 μm pitch, 4 x 10^{-7} A/cm^{-2} dark current at 77 K with -20 mV bias, 31 mK NETD at 77 K with $f/2.3$ optics and 1.2 ms integration time [72].

Figure 3.10. 320 x 256, 30 μm pitch p-i-n FPA image [72]**.**

They reached 99% operability and 1.2 A/W responsivity at 4.1 μm wavelength. They obtained 4.1 x 10^{12} $cm/Hz^{1/2}$ detectivity, as well. In 2017, Jenkins et al. [73] and Sharifi et al. [74] showed their works.

Figure 3.11. 1156 x 2040, 5 μm pitch FPA images at 150 K [73]**.**

Jenkins'[73] work was the demonstration of 2.4-megapixel format FPA having properties that 5.1 µm cut-off wavelength, small pitch 5 µm, operating at high temperature with low dark current and high operability. Their median dark current was 2.3 x 10^{-5} A/cm^{-2} with operability larger than 99.9 % and quantum efficiency > 60 % (Figure 3.11).

Figure 3.12. 10 µm pitch 2k x 2k FPA images at 120 K and 150 K with $f/3.9$ [74].

Sharifi et al. presented 10 µm pitch 2k x 2k FPA having 3 x 10^{-5} A/cm^{-2} dark current with 5.11 µm cut-off wavelength and 2.2 x 10^{-6} A/cm^{-2} with 4.6 µm cut-off wavelength. They also reported 5 µm pitch FPA results which are 6.3 x 10^{-6} A/cm^{-2} at 150 K with 5 µm cut-off wavelength having ~50 % quantum efficiency with 20 mK NETD at 150 K (Figure 3.12).

After giving recent studies about T2SLs, design and fabrication details of 640 x 512, 15 µm pitch MWIR Type-II Superlattice FPA fabricated with this thesis will be presented in the following chapter.

CHAPTER 4

FABRICATION OF MWIR InAs/GaSb FOCAL PLANE ARRAY

Starting with epilayer growth, an infrared device is fabricated with consecutive process steps. Fabrication processes are simply forming a detector structure in order to get the electro-optical signals from a device. An infrared detector undergoing numbers of fabrication steps are ready to operate for desired applications. The well-establishment and feasibility of fabrication steps determine the performance of a device. Moreover, the more feasible fabrication steps, the utmost performance one get from the device.

In this thesis study, the fabrication of large format (640 x 512) 15 µm-pitch, MWIR T2SL FPA, the process approaches which affect the device performance, and results of these approaches are the main focus points. Beginning with the regular flow of the process, different methods to reach optimum device performance are handled in this study. Different process techniques were performed on same epilayer design to compare effects of them on device performance individually. The specifications of process methods to compare with one another are as follows:

- Comparison of mesa formation methods: wet etching and dry etching
- Determination of ohmic contact metals
- Effects of different passivation materials and methods

- In bump formation
- Fixing flip-chip bonding and underfilling parameters
- Substrate thinning investigations.

Even if the details of device design and fabrication processes are kept secret by most of the manufactures and developers because of the strategic importance, the information about fabrication and device design of T2SLs FPA will be presented in this work, in a certain extent. The application procedures of process steps and the morphologic investigation of these methods are discussed in this chapter. The brief information about epilayer design, the standard flow of fabrication process, and individual details of each step will be studied separately. The practiced different approaches' results and their effects on device performance will be worked up next chapter.

4.1. Type-II Superlattice Epilayer Design

It is well-known that Type-II Superlattice devices are artificially created structures in accordance with their application areas. Moreover, they are called 'The Bandgap Engineered Devices". The design of them alters from one manufacturer/developer to other. The rivalry in between different groups to reach the ultimate device performance and make an impact on literature with own investigations, urge to be kept some information in secret. Therefore, the epilayer, which may be the most important part of the device, is becoming more valuable for manufacturers/developers.

Before designing the structure, not only for the T2SL structures but also any semiconducting devices, some issues should be taken into account in such a way that the lattice constants should match and that the thicknesses of the layer should be enough for the operation of interest. In T2SL structures, main materials are InAs and GaSb which have very close lattice constants [75]. Some III-V semiconducting materials band gaps and respective wavelength that they have sensitive as a function of lattice constants are given in Figure 4.1 [75].

The lattice constants of InAs and GaSb are equal to 6.0585 Å and 6.0955 Å, respectively. The matching in lattice parameters reduces the possible formation of micro-voids and stress in crystals during epitaxial growth.

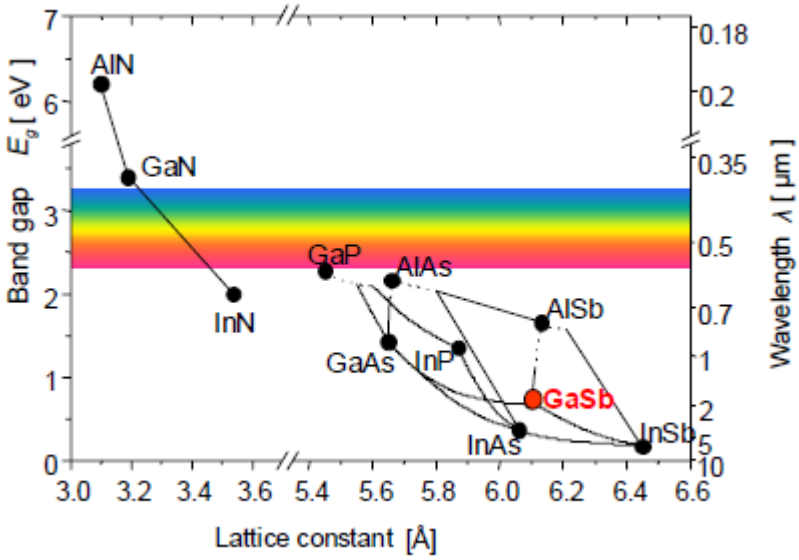

Figure 4.1. Band gap and respective wavelength as a function of lattice constants for III-V semiconductors [75]**.**

However, some other materials can also be used to create smooth transition some material to another one. In T2SL structure, InSb and AlSb are also used for these purposes besides with the electro-optical benefits. In Table 4.1, the lattice constant and bandgap energy values are shown.

Table 4.1. Lattice constants and bandgap for selected III-V compound semiconductors [75]**.**

Semiconductor compound	Lattice constant a* [Å]	Band gap E_g* [eV]
AlSb	6.1355	1.63
GaSb	6.0955	0.72
InAs	6.0585	0.35
InSb	6.4788	0.16
* at $T = 300$ K		

The epilayer processed in this thesis study is our structure, and it is shown in Figure 4.2. The epilayer is in the form of p-i-B-n design. It is grown on n-type GaSb substrate.

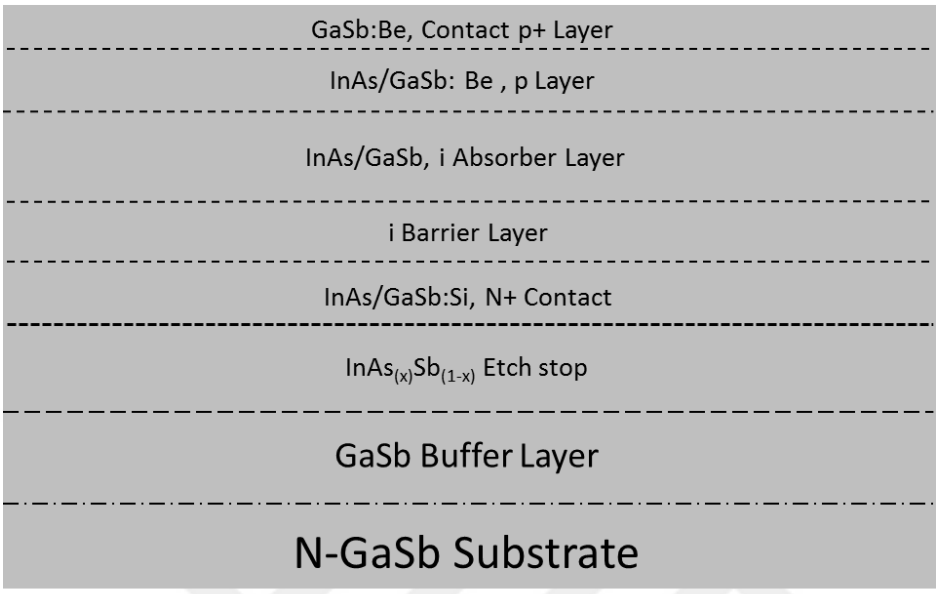

Figure 4.2. T2SL epilayer design used in this thesis (not to scale).

The graded GaSb buffer layer is grown on the substrate in order to reduce the lattice mismatch in between InAsSb and GaSb. InAsSb layer is designed as etch stop layer in order to use etchants selectivity between InAs/GaSb layer and InAsSb in mesa etching and substrate thinning steps. The standard p on n junction approach is applied, and heavily doped GaSb layer is adopted at the top the epilayer structure to get easy contact.

4.2. Type-II Superlattice Focal Plane Array Fabrication

The standard flow of detector fabrication process starts with mesa formation and continues with ohmic contacts, passivation, In bump formation, etc. The whole steps are shown in Figure 4.3

Once the fabrication cycle, shown in Figure 4.3, is completed, T2SL infrared device is ready for characterizations. The final form of an individual pixel is shown in Figure 4.4, before FCB bonding.

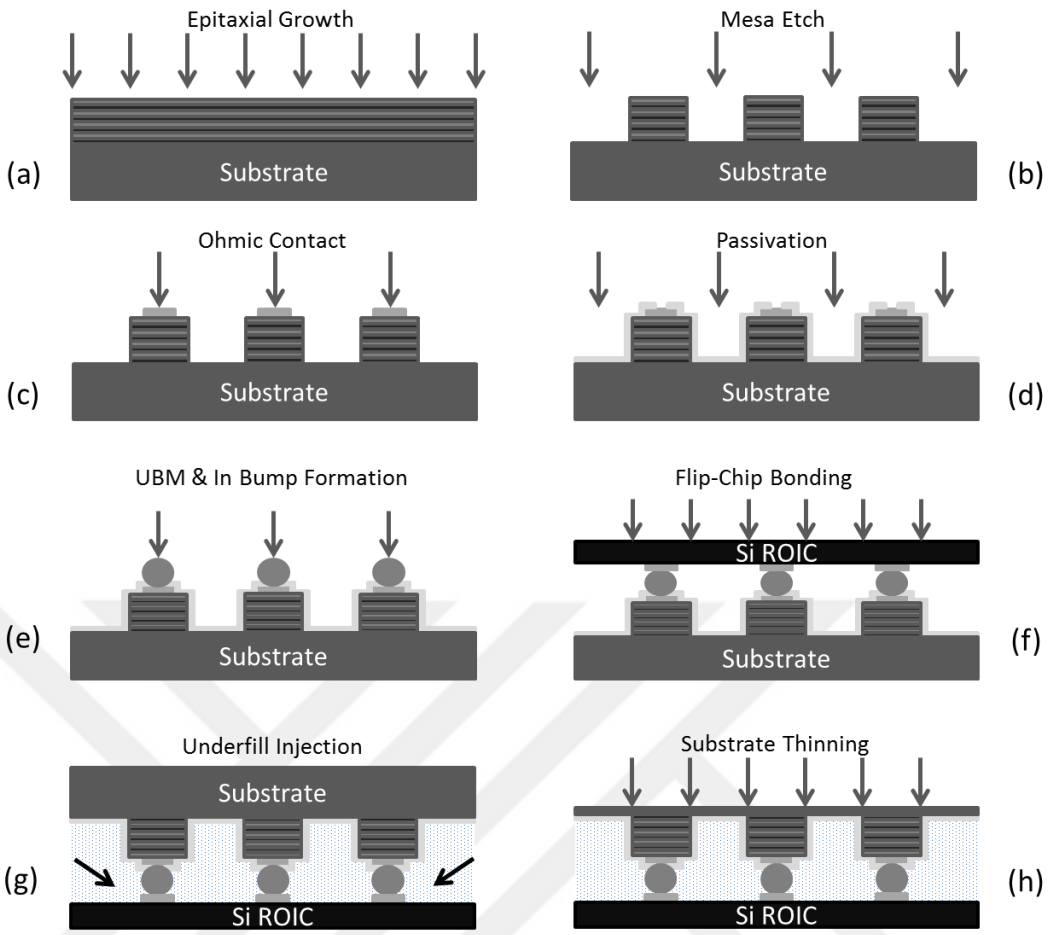

Figure 4.3. T2SL FPA fabrication steps (not to scale).

Each fabrication steps will be discussed in following sub-sections in accordance with the order of original flow.

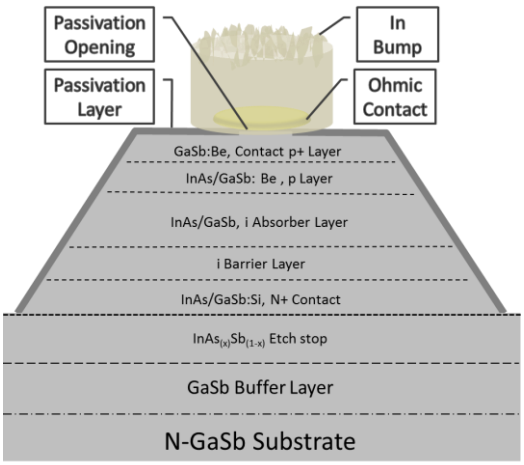

Figure 4.4. Illustration of the T2SL pixel after fabrication processes completed (not to scale).

4.2.1. Mesa Formation

In this work, detector structure is adapted to mesa-type pixels because it offers some advantages in terms of process compatibility such as offering simplicity and high control. The aim of formation of mesa structure is the isolation of p-n junction, and it is performed by basically etching down T2SL layers up to n-type layer, like in our p-on-n design. Two fundamental etching mechanisms, wet etching and dry etching, were performed, and their effects on device performance were analyzed.

4.2.1.1. Wet Etching

Wet etching, it is also called wet chemical etching, fundamentals depend on chemical reactions in between etching agent and being etched materials. Whether wet etching offers advantages or disadvantages depend on the type of material that being etched. For example, its property of being selective or less selective or material dependent etch rate can be interpreted as an advantage for some of the semiconducting material etching, whereas it can be disadvantages for other etching aims. However, it is absolute for wet etching that it offers damage free surface. The typical drawbacks for wet etching can be listed as:

- Isotropic etching
- Difficulty in uniformity
- Repeatability problems

However, these drawbacks are also material dependent. Anisotropic etching with highly repeatable ratios can be achieved. To illustrate, Si etch with KOH is orientation dependent, and anisotropic etch profile can be provided in this case.

Wet etching of InAs/GaSb T2SL structures is performed with different etchants such as $C_6H_8O_7$ and HCl based acidic solutions. Some etchants for GaSb and InAs are reported in the literature as indicated in Table 4.2 [76].

Table 4.2. GaSb and InAs etching solutions [76]**.**

Citric Acid Based	$C_6H_8O_7$: H_2O (citric acid solution)	1 g : 1 ml
	Citric acid solution : H_2O_2	2 ml : 1 ml
KNa – Tartaric Acid Based	$C_4H_4KNaO_6$: H_2O_2 : HCl : H_2O_2	15 g : 200 ml : 160 ml : 14 ml
Hydrochloric acid Based	HCl : H_2O_2 : H_2O	100 ml : 1 ml : 100 ml

The etch rates of etchants which are listed in Table 4.2 are also given in Table 4.3 [76].

Table 4.3. Etch rates for different materials where A, B, and C are citric acid based solution, tartaric acid based solution, and hydrochloric acid-based solutions, respectively.

Etch Rate (nm/min)	**InAs**	**InAsSb**	**GaSb**	**AlSbAs**
A	92.8 ± 2.8	88.9 ± 3.0	0.84 ± 0.04	-
B	75.3 ± 12.3	26.1 ± 2.4	449.5 ± 6.3	> 2000
C	176.8 ± 14.5	51.2 ± 7.9	281.2 ± 25.4	1371.2 ± 13.6

There are also different types of etching solutions for T2SL structures. Addition of phosphoric acid to citric acid solution creates another etchant for T2SL [77].The mixing ratio for $C_6H_8O_7$ / H_2O : H_2O_2 changes the etch rate of the solution [78].

In this work, the citric acid based solution is used for wet mesa etching. However, different types of citric acid based solutions with different mixing ratios and combination of them with phosphoric acid were analyzed. Some of the etchants used for mesa etching of T2SL is explained in following sub-sections.

$C_6H_8O_7$ / H_2O : H_2O_2

In the early stage of thesis study, $C_6H_8O_7$ / H_2O : H_2O_2 is used to check etching and to examine the etch rate. The systematic experiments were conducted for different mixing ratios for strict $C_6H_8O_7$ / H_2O ratio and altering H_2O_2 ratios. Even if results were not detailed in this work, it was noted that the etch rate of $C_6H_8O_7$ / H_2O : H_2O_2 solution for any mixing ratio was so slow that it was not desired to put samples in time intervals ranging from several hours to days.

H_3PO_4 : H_2O

The second part of mesa formation experiments was conducted with H_3PO_4 : H_2O_2 solution. 15 µm pitch samples are prepared with standard lithography methods, and samples are etched by phosphoric acid solutions with different ratios. Change in ratios is applied to adjust the etching time for the acceptable and reasonable duration. In Figure 4.5, Scanning Electron Microscopy (SEM) images of one of the samples etched by phosphoric acid solutions can be found.

As it can be seen from Figure 4.5, the sidewalls of the mesas are not smooth enough even if the sidewall angles of the mesa are applicable for this work. The smoothness of sidewalls provides easy and complete passivation, and this provides opportunities for the reduction of dark currents related to surface leakages. Therefore, smoother surfaces are needed for better performance.

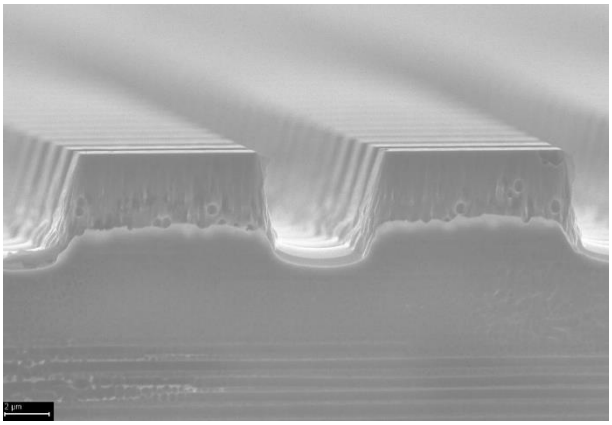

Figure 4.5. The SEM image of H_3PO_4 : H_2O (3:1) etched sample.

$C_6H_8O_7$ / H_2O : H_3PO_4 : H_2O_2

Citric acid solutions failure to fulfillment in suitable etch rate and deficiency of phosphoric acid in providing smoothness in mesa sidewalls steer us towards to try different etchant for mesa wet etching. For this reason, another etchant, which is the combination of $C_6H_8O_7$ / H_2O : H_3PO_4 : H_2O_2 with a ratio of 10:1:1, is examined for T2SL structures. 15 µm pitch samples are prepared with same lithography techniques on the pieces of the same wafer on which other etching experiments performed. The etch rate is calculated as 8 nm/s. To investigate the smoothness of mesa sidewalls and surface, SEM images are taken (Figure 4.6).

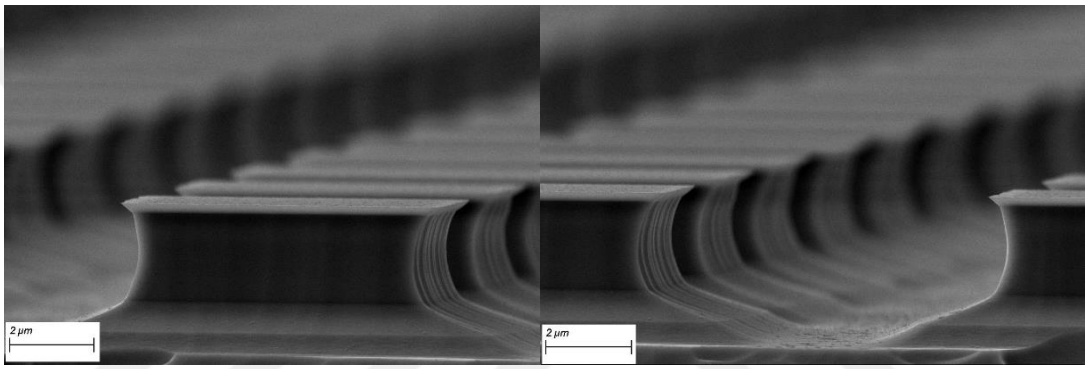

Figure 4.6. SEM images of mesa etched sample with $C_6H_8O_7$ / H_2O : H_3PO_4 : H_2O_2.

From Figure 4.6, the smoothness and cleanness of mesa sidewalls/surfaces are easily seen. Even if sidewall angles are not at the desired level, the feature of providing the damage free surface makes $C_6H_8O_7$ / H_2O : H_3PO_4 : H_2O_2 solution be a better choice for wet etching of T2SL structures.

4.2.1.2. Dry (Plasma) Etching

The more anisotropic feature of dry etching method than wet etching makes this method more suitable when the high aspect ratio is required, especially for small pixel pitch or deeper etch cases. However, surface damage is generally higher in dry etching than wet etching. To overcome this problem, Inductively Coupled Plasma Reactive Ion Etching (ICP-RIE) which provides low surface damage with high-density plasma with low ion densities, resulting in smoother surfaces, is adopted to mesa formation steps through other dry etching methods, such as standard reactive

ion etching. Besides with the low damage property, dry etching provides anisotropic etch resulting in high aspect ratio for active area designs. In ICP-RIE method, etchants are the mixtures of some gases, and etching profile is determined by adjusting ratios of these gas mixtures, which is performed merely by changing ion density and ion energies in plasma environment or heating the sample. In other words, numbers of parameters affect etching profile in ICP-RIE method. Although most of the groups and developers prefer wet etch in mesa formation, some of them use dry etching in mesa formation step [67]. Different types of gas mixtures are used in dry etching of InAs/GaSb T2SLs like chlorine based [79], halogen gas mixtures [80], and CH_4 based [81]. As it mentioned before, the common drawback of all chemistries is to leave damaged surfaces, besides with the specific drawbacks of each. Therefore, depending on the previous experiences, some of the chemistries such as CH_4 and $SiCl_4$ are excluded from dry etching experiments of T2SL mesa formation because CH_4 leaves behind carbon-contaminated surfaces, and $SiCl_4$ is corrosive. In this thesis study, one of the chlorine-based mixture (BCl_3/Cl_2) and post-treatment procedure are investigated for dry etching of T2SLs.

BCl_3/Cl_2 Mixture:

It is well-known that chlorine chemistry is cleaner than other dry etching chemistries like CH_4. Being a common dry etching gas BCl_3, which etches most of the binary and compound materials, is combined with Chlorine (Cl_2) for etching recipe. In this mixture Ar also used for a carrier gas, to dilute gas mixture, and to use its' sputtering feature. The mixing ratio for BCl_3, Cl_2, and Ar are developed after several experiments to optimize etch rate and etching profile. As soon as determining ion densities and energies with the light of carefully conducted trials, dry etching recipe for T2SLs is obtained.

In Figure 4.7, SEM image of the dry etched sample with the initial recipe is shown. As it can be seen from Figure 4.7, trenches at the bottom of mesas which are foreseen to cause passivation difficulties and even breakages in mesas are observed.

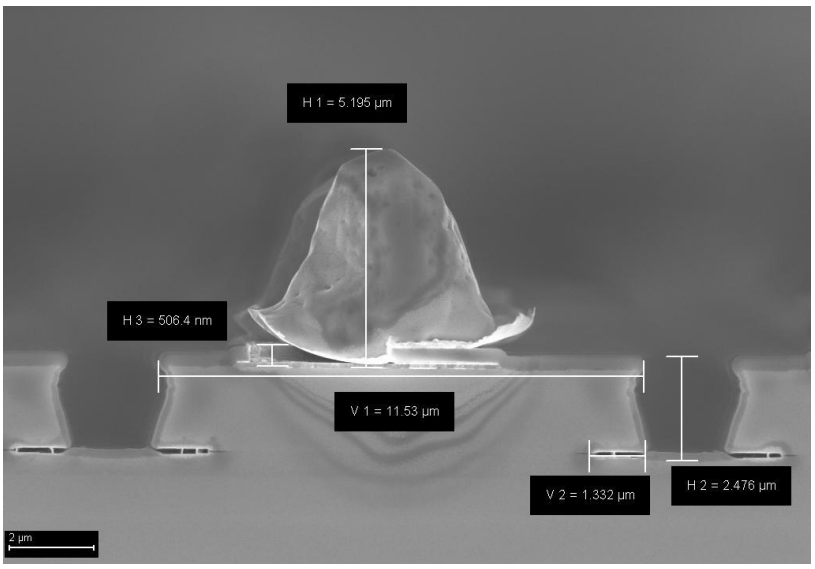

Figure 4.7. The initial result of dry etching of T2SL.

To overcome this trench issue, we try to optimize our dry etching recipe, and we reach the result shown in Figure 4.8 Trenches are not seen even deeper etch. The optimization is provided by not only adjusting gas ratios and ionic properties of plasmas but also heating up the sample.

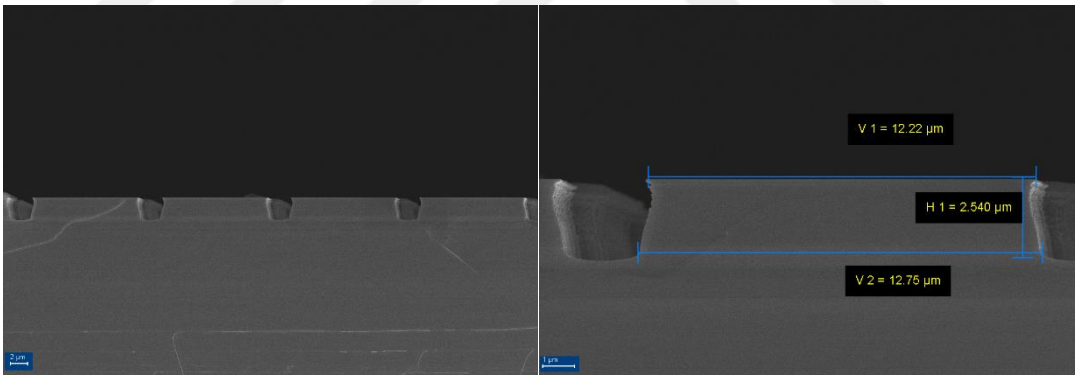

Figure 4.8. The optimized dry etching recipe results in mesa structures.

However, damaged mesa sidewalls can easily be seen in Figure 4.8. Sidewalls are needed to be enhanced to avoid possible reductions in device performance which can occur by causing leakage currents. Also, the angle of the mesa sidewalls is too sharp to passivate them conformally even if our passivation capabilities can tolerate.

Hence, the final optimization is performed on sidewall morphologies. After some specifications on dry etching recipe, the final dry etched mesa profile is obtained, and it is shown in Figure 4.9.

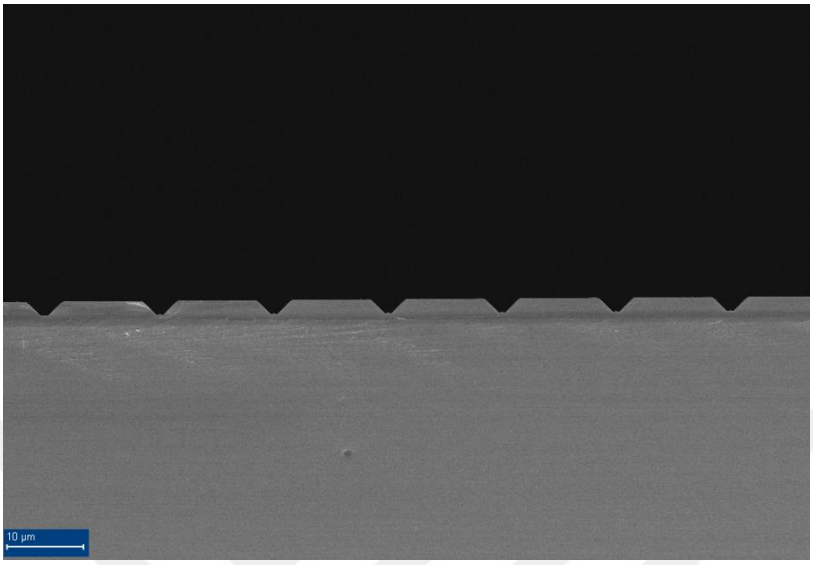

Figure 4.9. The enhanced dry etching recipe result in mesa structures.

Sidewalls of mesas are enhanced, and the angle of them is optimized for better and more comfortable passivation. Post-treatment procedure provides this enhancement. The damaged surfaces are exposed to low energy Ar plasma after mesa etch. Ar plasma provides physical etch and ensures smoother sidewall profile.

Even if both wet and dry etching methods are improved for mesa formation, wet etching surpasses dry etch because of the advantages that it provides. Therefore, in FPA level fabrication processes, the wet etching method is preferred; nevertheless, both methods are compared in large area pixel level regarding their performance. This comparison of wet and dry etching will be discussed in next chapter.

4.2.2. Ohmic Contact

Ti, Pt, and Au are used as ohmic contact metals by many groups [67,82]. As it is mentioned in Section 4.1, epilayer structure is finalized with highly doped GaSb layer to take ohmic contact easily. Additionally, ohmic contact formation is not separated for n-type and p-type layers. In other words, top and bottom contacts are deposited at

the same time. The initial approach for ohmic contact metals is to use standard Ti, Pt, and Au, and early FPA fabrications are made with these metals by using electron beam technique. However, the difficulty in evaporation of Pt canalizes us to change Pt with a metal which has same property or to discard it. Then, Pt is discarded from ohmic contact metals. Any reduction in device performance related to this change is not observed. Therefore, the final fabrication procedure for ohmic contact includes only Ti and Au metals.

4.2.3. Passivation

Among the other FPA fabrication steps, passivation may be the most performance affecting one. Otherwise, surface passivation is a performance limiting factor. Therefore, the general trend for this step is to keep details as proprietary information by detector manufacturers. Large numbers of passivation methods and materials are available in the literature for T2SL structures, including dielectric coatings and electrochemical depositions without details. However, most of the manufacturers and researchers agree with using SiO_2 as a passivation material. In this thesis study, numbers of passivation methods and materials are used as well as SiO_2. Pre-passivation-treatment is also studied. The details of passivation step are kept secret.

Due to the improvement in device performance that it creates, polyimide is chosen as passivation material for T2SL structures. Polyimide has low stress. It also provides a conformal coating. Likewise, it is possible to create planar surfaces, to a certain extent, with polyimide. These opportunities that polyimide provides makes following fabrication steps easier than no others do. In following sub-sections, passivation materials and a pre-treatment used in this work will be given with some application notes. Their effects on device performance will be discussed in next chapter.

4.2.3.1. SiO_2

As it is mentioned in the previous section, SiO_2 is widely used passivation material for T2SL structures. However, high-grade SiO_2 demands a temperature minimum 250℃ or over. These temperatures can harm the raw material of T2SLs. In other words, the temperature reaching 250℃ and over may affect the device performance

by harming the raw material. Therefore, the general trend is to deposit SiO_2 at low temperatures. However, the deposited SiO_2 quality highly depends on the deposition temperature among other deposition parameters.

Due to the aforementioned necessities of SiO_2, initial experiments for passivation with SiO_2 start with the deposition of it at low temperature with high quality.

SiO_2 Deposition with PECVD

It is well-known that SiO_2 at high quality is deposited by using Chemical Vapor Deposition (CVD) method, and most of the manufacturers and developers widely use it. The optical and dielectric properties of SiO_2 are satisfied with this method more effectively. Also, CVD methods differ from each other depending on the deposition environment and the physical parameters which are used in deposition operation. Among the other CVD methods, Plasma Enhanced Chemical Vapor Deposition (PECVD) method requires lower temperatures than others. Therefore, for the method of deposition of SiO_2, PECVD method is chosen in this work.

For passivation applications, the conformal coating of surfaces and depositing SiO_2 at low temperature are crucial parameters rather than optical parameters, such as the index of refraction. However, for understanding the quality of deposited material, this parameter gives an idea about it. Beginning with dummy samples, PECVD SiO_2 films are deposited, and deposition parameters are adjusted for the value of reactive index equal to 1.42 ($n = 1.42$) which is the outmost value for SiO_2 found in literature. All depositions are performed in same temperature, 200℃. SiO_2 coated samples refractive index measurements are performed with Spectroscopic Ellipsometry method. After deposition parameters are fixed for necessities, and the reproducibility of deposition is achieved, real samples having mesa structures, which are same with T2SL FPAs, is coated with PECVD SiO_2. In Figure 4.10, PECVD SiO_2 coated samples are shown. The sidewalls of mesa structures are coated with SiO_2 film successfully. In other words, conformal coating is achieved successfully with this method.

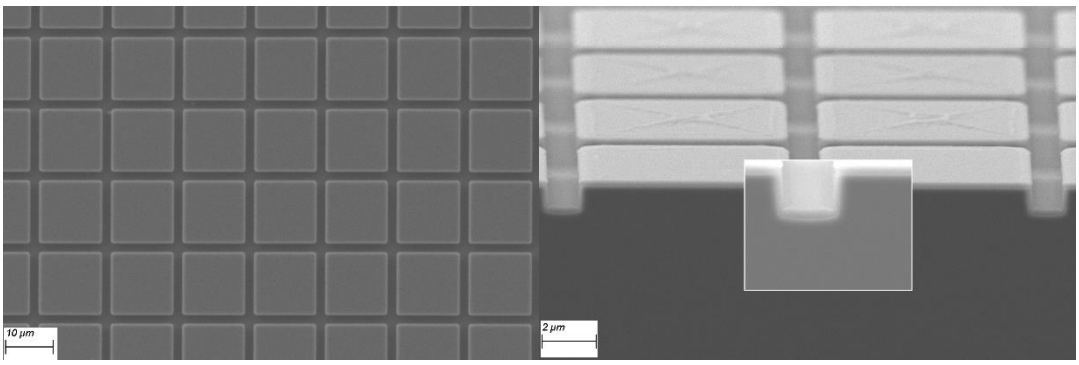

Figure 4.10. SiO_2 coated mesa structures with PECVD method.

In this type of deposition of SiO_2 films, the deposited film should be patterned to reach ohmic contact points. Patterning is done simply by a standard lithography method, and holes are opened by using either dry etching or wet etching. Using wet etch technique to open holes on deposited film may create undercuts, or under-etches which results in the larger hole than the desired ones because of its isotropic etch profile. Therefore, passivation openings are opened by dry etching, having anisotropic etching feature, with CHF_3 chemistry.

Even if PECVD method meets requirements, we seek for different a way for deposition of SiO_2 to create an alternative. For this reason, Electron Beam Deposition method is used for passivation with SiO_2.

SiO_2 Deposition with E-beam

SiO_2 pellets are evaporated and deposited on a sample by using e-beam in this technique. Thicker depositions can be achieved since the quality of the film is independent of temperature, and temperature does not reach critical values in this technique. Moreover, passivation openings can be opened either by using dry etching or wet etching after patterning with lithography, which is same in PECVD deposition of SiO_2. However, lift-off method can also be used in this type of deposition of SiO_2 to open contact holes. A sample is patterned by lithography, deposition is performed, and the photoresist is removed. In this work, because of its simplicity, SiO_2 is deposited on lithographically patterned samples, and then SiO_2 over holes is lifted-off.

In Figure 4.11, SEM images of SiO_2 deposited samples can be found. Mesas are formed by using dry etch method for these samples. As it can be seen from images, contact holes are opened. These opening are performed by lift-off method.

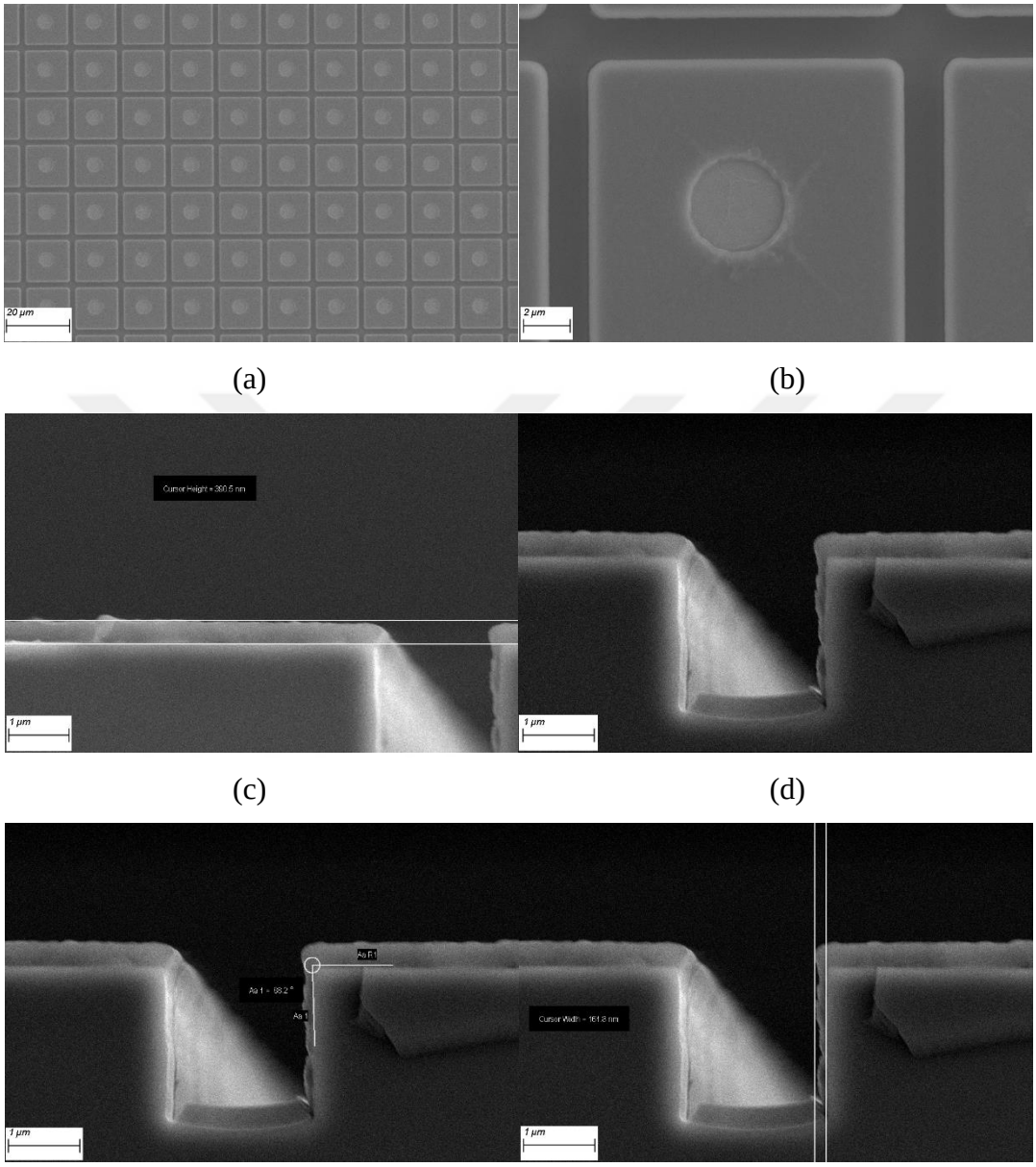

Figure 4.11. SEM images of e-beam SiO_2 coated samples with passivation openings.

Before the deposition of SiO_2, the thickness of SiO_2 film is adjusted in between 390 nm and 400 nm intervals. In part c of Figure 4.11, the thickness of SiO_2 film is about 390 nm. The 89° angle of mesas affects the thickness of SiO_2 at the sidewalls. However, ~200 nm film thickness is achieved at sidewalls, shown in Figure 4.11, part e.

Refractive index measurements of SiO_2 films, which are deposited by the e-beam method, are also performed. The refractive index value is equal to 1.41 which is close to reported value SiO_2 in literature, and it is acceptable as a passivation material in terms of quality. As it is mentioned before, the results of electro-optical measurements and comparison of passivation materials and methods will be discussed in next chapter.

4.2.3.2. Photoresist

The standard usage of photoresist is generally for lithographic applications. However, polymeric and dielectric features of photoresist make it a suitable candidate for passivation material. It has the ability to cover all surfaces to which it is applied. Spin-coated photoresist makes surfaces smoother even if some structures such as mesas and contact metals exist. Therefore, the usage of photoresist as a passivation material is also investigated in this part of thesis study.

Passivation with photoresist is simply done by spin coating photoresist and patterning it just in passivation-opening-lithography. However, it is known that abnormal use of photoresist, unlike in lithography applications, create some difficulties in passivation step such that it can dissolve in other photoresist used in following fabrication process steps and that it could not stand for the cryogenic temperatures. Therefore, the feasibility tests should be performed before applying it for passivation of T2SL structures. Initial tests are focused on the dissolution problem of photoresist in other photoresists. Accordingly, the photoresist is spin coated on dummy samples, hard-baked appropriately at different temperatures, and its dissolution in others is investigated.

After determining proper parameters for photoresist dissolution problem, liquid nitrogen tests are conducted to check its attitude at cryogenic temperatures. All tests were passed successfully by photoresist.

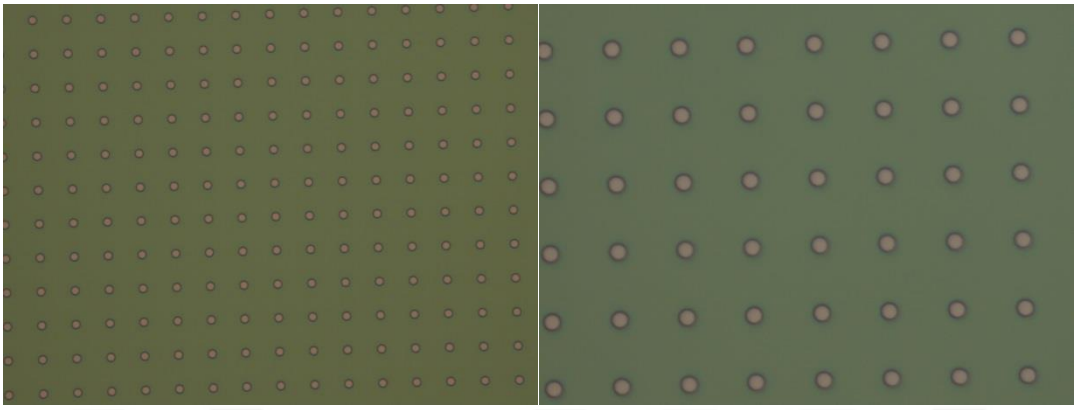

Figure 4.12. Microscope image of photoresist coated wafers with passivation openings.

In Figure 4.12, microscope images of a wafer which is passivated with photoresist and its passivation openings are given. Besides with the excellent morphology of the surface, planarization is also provided with photoresist passivation. Thus, passivation with photoresist can be treated as an alternative method for passivation of T2SLs.

4.2.3.3. Polyimide

Polyimide is another passivation material for T2SL structures. Even if features and advantages that it provides are similar to photoresist, polyimide differs from photoresist in some specific aspects such as its hardness and being photo-definable or non-photo-definable. To benefit from its capabilities, polyimide is also studied in this thesis work.

It is known that there are lots of commercial polyimides and their derivatives. The polyimide which will be used for passivation should satisfy following requirements:

- Conformal coating
- Low stress
- Application at low temperature

Polyimide gains its hardness after reaching a temperature value which fully polymerizes itself. However, patterning fully polymerized polyimide is rather tricky. Therefore, initial experiments are based on two different uncured polyimides. Passivation holes of uncured polyimides are opened just after passivation-opening-lithography by using the same chemical, which is used for developing the exposed part of photoresist in the lithography step. In Figure 4.13 and Figure 4.14, images of polyimide coated samples which are passivated with different polyimides (they are called poly-b and poly-a from now on) are shown. Polyimides are cured in this samples. In Figure 4.13, poly-a is used, and holes are not good enough to provide uniform opening property.

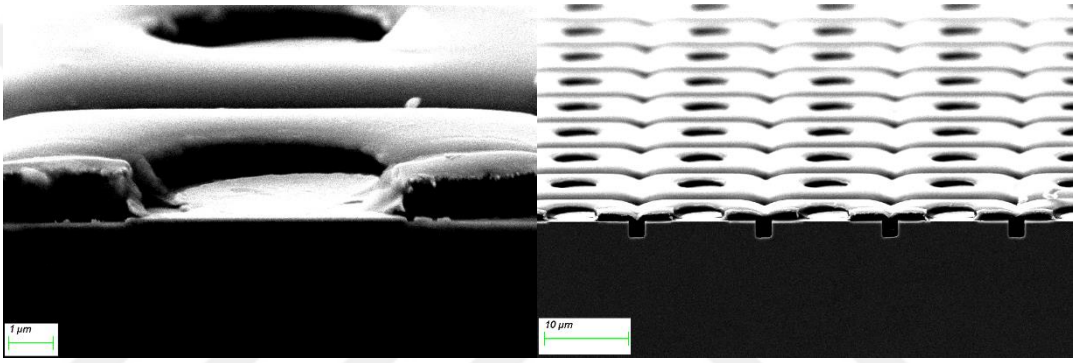

Figure 4.13. SEM images of uncured Poly-a and its passivation openings.

Microscope images of poly-b are shown in Figure 4.14. Opening profile is not worth to deal with. SEM images are not taken. From these figures, uncured polyimides do not work well. Hence, the second part of polyimide studies is about cured polyimides.

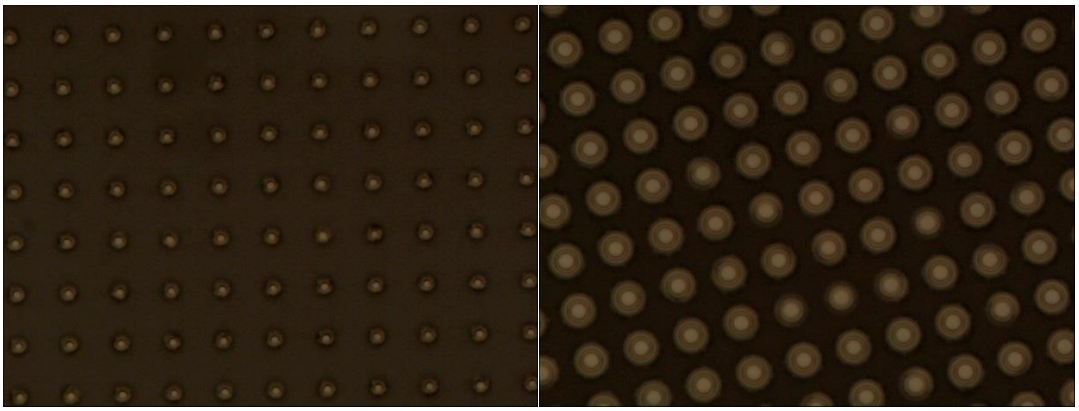

Figure 4.14. Microscope images uncured Poly-b and its passivation openings.

As it is mentioned before, patterning the cured polyimides is rather difficult. Moreover, cured polyimides are patterned either by using long-term plasma ashing with O_2 or dry etching with hard chemistries like CH_4 and CHF_3 [83,84]. It is not desirable to have undergone samples with solid chemistry. Therefore, initial experiments on cured polyimides are shaped over O_2 plasma ashing. After curing polyimide, passivation lithography is performed, and O_2 plasma ashing discards polyimide in holes. In Figure 4.15 and Figure 4.16, SEM images of similarly processed samples which differ each other only from applied polyimides are shown. poly-a and poly-b polyimides are used for these samples, respectively. Even if passivation openings enlarge due to the long-term O_2 plasma ashing, surface morphology is quite favorable than uncured ones.

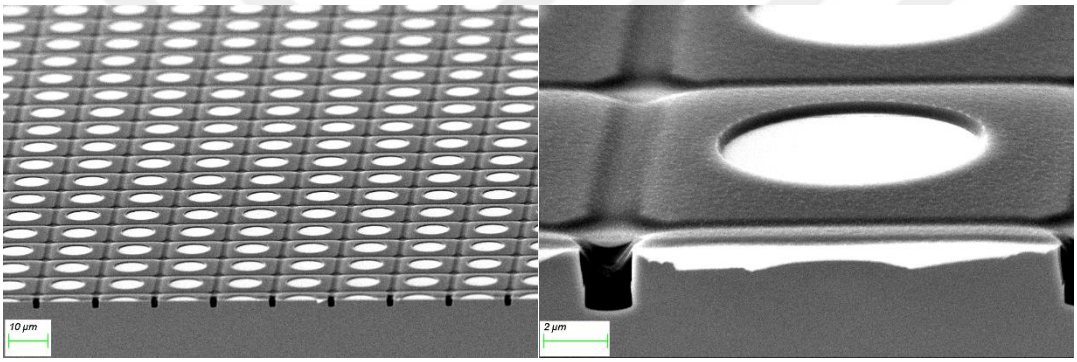

Figure 4.15. SEM images of cured Poly-a and its passivation openings.

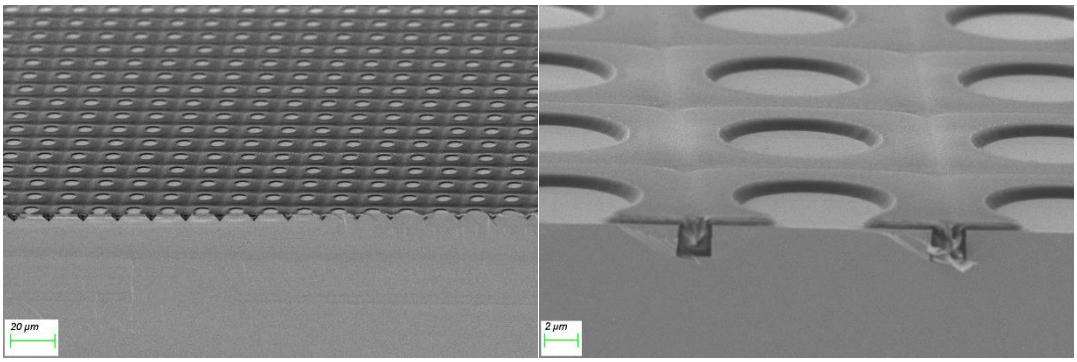

Figure 4.16. SEM images of uncured Poly-b and its passivation openings.

The difference between cured poly-a and poly-b is that poly-a expands in three dimensions which naturally cause stress on samples. In addition to this, there is a slight difference on surfaces between both polyimides in terms of smoothness.

Contrary to poly-a, the expansion in poly-b is not observed. In other words, even it expands; it is not at observable level. Therefore, poly-b is chosen as a passivation material for T2SL structures.

The issue of long-term O_2 plasma ashing can cause problems or create difficulties in fabrication processes; hence, time that samples being exposed to O_2 should be reduced. In other words, the ashing/etching rate should be increased. This problem is handled by using ICP-RIE method with low energy but high ion density. With the help of ICP-RIE method, exposing time to O_2 is reduced from over 20 minutes to several minutes. Consequently, the application procedure of polyimide passivation includes curing polyimide and opening of holes by using O_2 plasma with ICP-RIE method.

4.2.4. Pre-treatments

By etching the surface to form mesa structures, broken bonds are unintentionally created, and some molecules easily make a bond with them. Generally, O_2 molecules tie these bonds; in this way, the surface is oxidized. Therefore, it is essential that passivation which covers those broken bonds should be performed immediately after mesa etching. However, some fabrication processes do not flow consecutively for mesa formation and passivation. In other words, any other step can be taken place in between mesa formation step and passivation step. In this case, broken bonds are tied with other molecules, which cause a reduction in devices performance or difficulties in following fabrication process steps. Hence, samples have been etched for a short time before passivation. In this work, all passivation methods are performed immediately after short wet etching of samples. In addition to short time etching, some researchers and developers use additional treatment before passivation. Some groups examine ammonium sulfide treatment, and it is sometimes called ‘wet passivation’ [85,86]. Their claims involve that broken bonds tie with sulfide, and the surface is sulfurized instead of being oxidized; as a result of this, some improvements are recorded in device performance. Therefore, the ammonium sulfide treatment is also studied in this thesis.

Samples being etched for mesa formations are treated with $(NH_4)_2S$ solution. Ammonium sulfide is diluted with H_2O by the ratio of 1:20 ($(NH_4)_2S$: H_2O), and samples have been soaked with this solution for 2 minutes.

In Figure 4.17, $(NH_4)_2S$ treated surfaces are presented. Any morphologic improvement is not noticed after $(NH_4)_2S$ treatment, the treatment effect; however, is claimed to be seen in device performance.

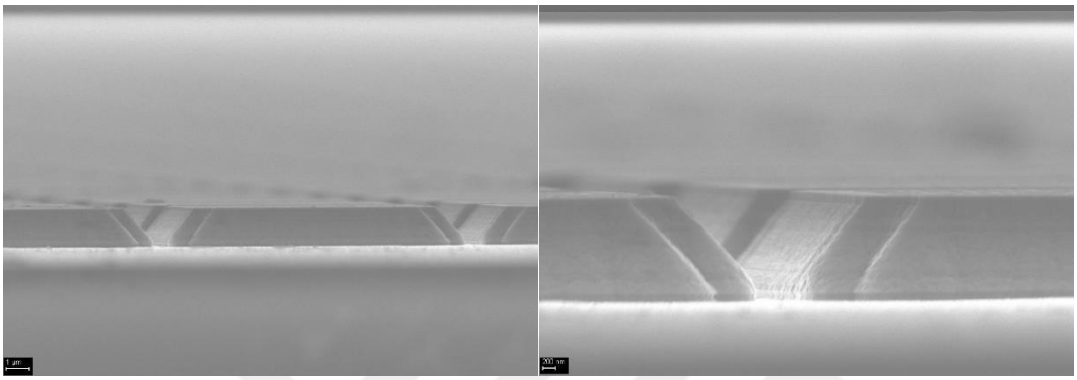

Figure 4.17. SEM images of $(NH_4)_2S$ treated surfaces.

In next chapter, results of electro-optical measurement of aforementioned passivation and pre-treatment methods will be given, and the final decision for passivation material and method will be explained.

4.2.5. Under Bump Metallization (UBM) and In Bump Formation

It is known that under bump metallization (UBM) is performed just before In bumps are formed. One way of proceeding in fabrication is that once UBM lithography, metallization, and lift-off are completed, In bump formation lithography is applied, and In bumps are formed by using different techniques such as electro-plating and physical vapor evaporation. In this case, two lithography steps should be done for each step. However, it is possible to perform both steps under the same lithography. While combining two steps into the same lithography brings some advantages such as avoiding one lithography step and its possible problems like alignment issues,

two-step-lithography is necessary for differently sized UBM and In bumps which is crucial for reflowed In bumps. In this work, reflow of In bumps is not studied; thus, the one-lithography operation is enforced.

Under bump metals are Ti, Ni and Au which are used to increase adhesion, to play a role as a barrier for In leakage, and having good interaction with In, respectively. These metals are evaporated by using electron beam physical vapor deposition method. The critical part of this step is the formation In bumps. As pixel pitches get smaller, especially for pitches smaller than 25 µm, the uniformity in the shape of In bumps become more significant. To get proper bump profile, photoresist thickness should be adequately large, and sidewalls of the photoresist should be smooth and free from deficiency. In addition to these, the more natural the lift-off is, the more uniform bumps are created. Irregularities in In bumps may create difficulties in hybridization to ROIC. For 15 µm pixel pitches, having 5-6 µm In bump thickness is enough for flip-chip bonding. Therefore, initial experiments are related to the investigation of the different photoresist profiles. In Figure 4.18 and Figure 4.19, photoresist profiles are shown for positive and negative photoresists, respectively. In Figure 4.19 the effect of post-exposure bake temperature on photoresist profile is given, as well. The positive photoresist profile is like a bucket. Also, the bottom of the patterned photoresist is smaller than the top of it; and hence, it is obvious that the lift-off will not be easy, and probably result in broken or non-uniform bump profiles.

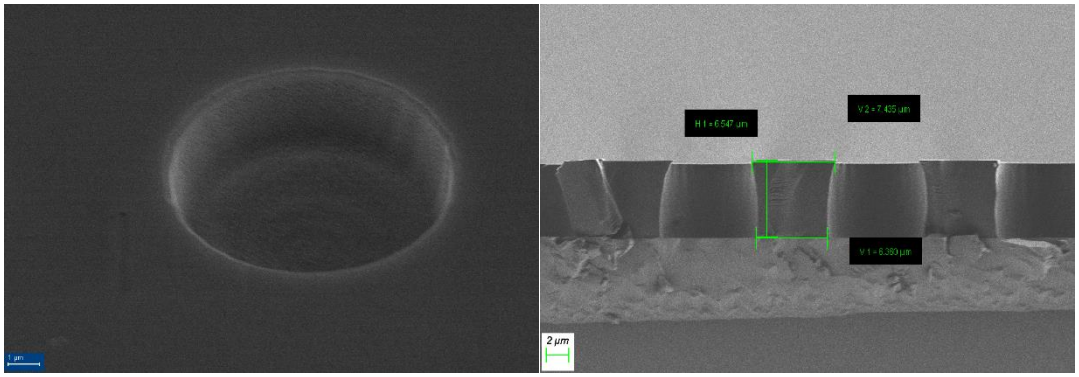

Figure 4.18. SEM images of positive photoresist develop profile.

In Figure 4.19, contrary to positive photoresist profile, shapes are like horizontally inversed buckets. Furthermore, increasing the post-exposure bake temperature provides more perpendicular resist sidewalls. Put differently, undercuts decrease with increasing post-exposure bake temperature.

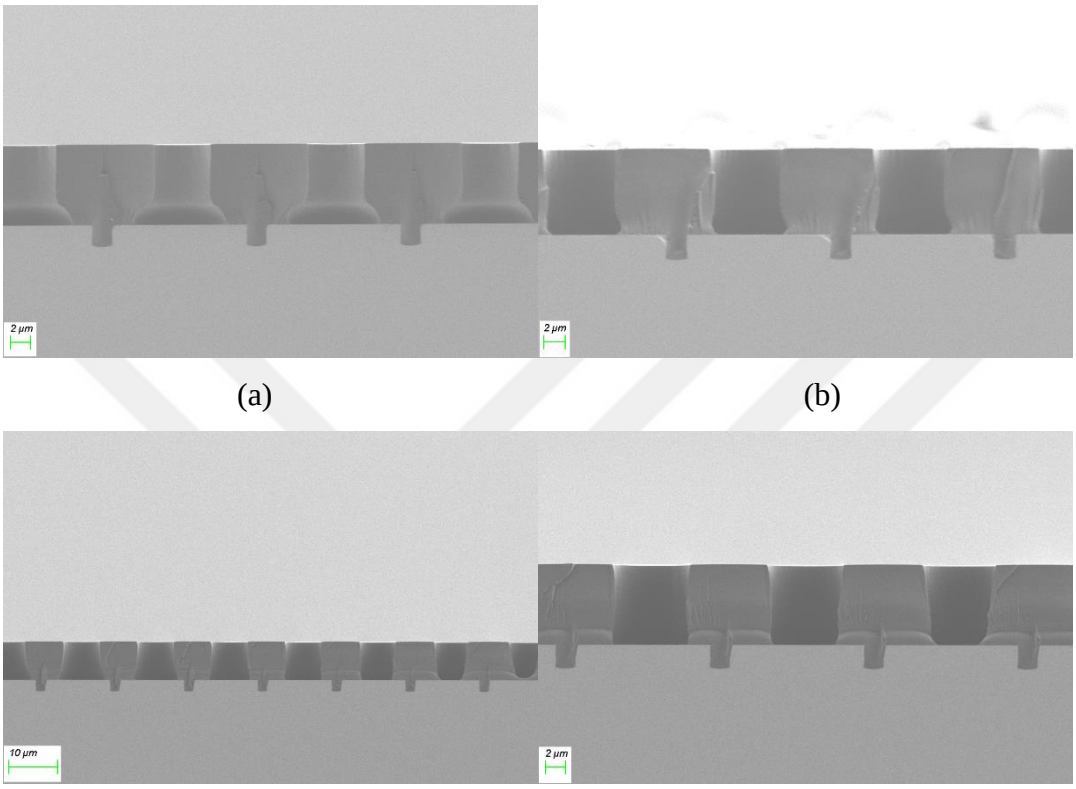

Figure 4.19. SEM images of negative photoresist develop profile with different post-exposure bake temperatures, (a) at 115 ℃, (b) at 120 ℃, (c) and (d) at 125 ℃.

Even if having sufficiently large undercut helps lift-off, In bump profile is sharper when the temperature of post-exposure bake is increased to some extent. Additionally, having large undercut causes In droplets alongside with In bumps. It is also observed that increasing the post-exposure bake temperature reduces In droplets. Thus, the highest post-exposure bake temperature among others is chosen for negative photoresist applications.

After photoresist profiles were investigated, Indium is deposited on same samples by thermal evaporation system. When photoresists are removed meaning that lift-off, the formation of In bumps are completed. In Figure 4.20 and Figure 4.21, SEM images of In bumps which are formed by using positive and negative photoresist are shown.

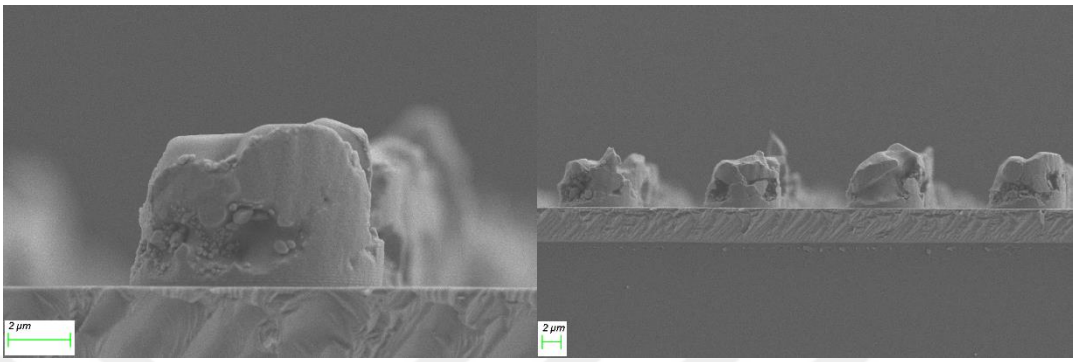

Figure 4.20. SEM images of In bumps formed with positive photoresist.

In bumps of positive photoresists (Figure 4.20) are neither uniform nor unbroken shapes. Although inside of bump is full, which a common problem that inside of bumps is empty, and their heights are as expected, non-uniformity in their shapes can cause In bumps to be broken in flip-chip bonding which can result in being gotten indiums to other bumps. Therefore, In bump profile needs improvement. However, indium bump profile of negative resist (Figure 4.21) is better than positive photoresist in terms of uniformity and fulfillment. Their shape and fullness satisfy the pre-requirements of flip-chip bonding. Therefore, in T2SL fabrication processes, In bump formation will be performed by using negative photoresists with developed lithography and deposition parameters.

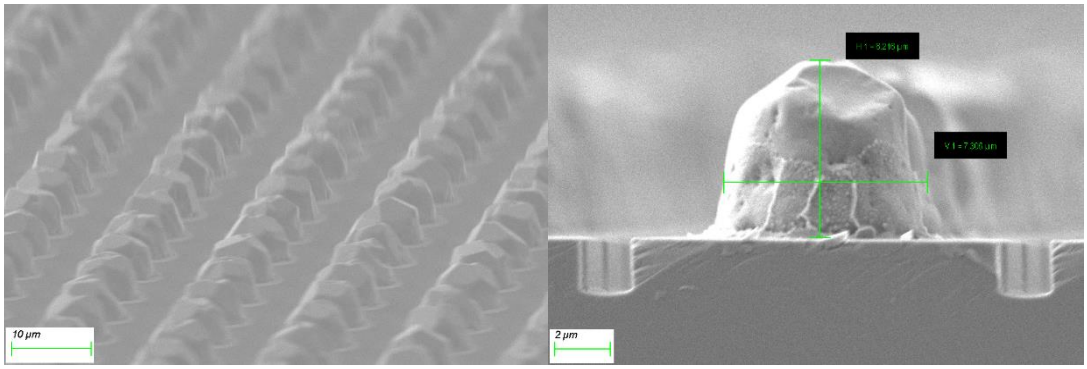

Figure 4.21. SEM images of In bumps formed with the negative photoresist.

Before hybridization process, ROIC should be processed. ROIC needs only In bump structures; hence, its process is quite more straightforward. It is obvious that under bump metallization should also be performed for the same reason with FPAs.

The procedure improved for FPA can also be used for ROIC. In Figure 4.22, SEM images of dummy ROIC processed with same parameters with FPA are shown.

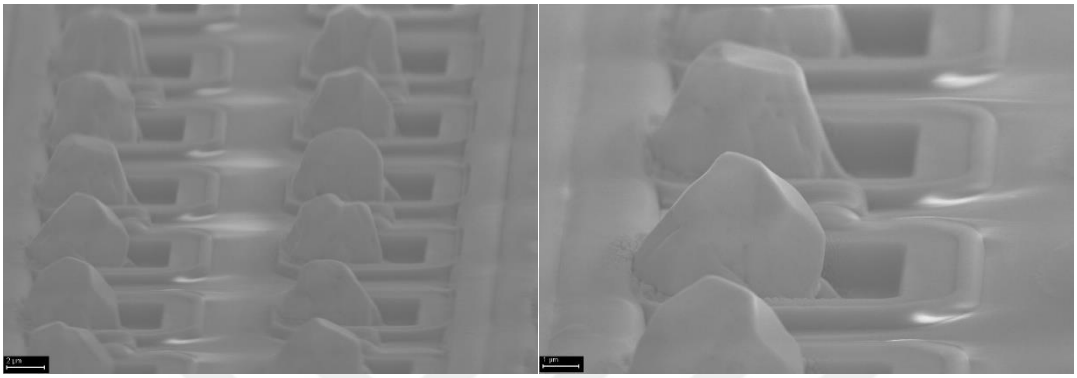

Figure 4.22. SEM images of ROIC In bumps formed with a negative photoresist.

Except for the alignment problem, bumps are as expected. For 15 µm pitch size, 5-6 µm FPA In bump height and ~2 µm ROIC In bump height are enough for good FCB.

4.2.6. Dicing, Flip-Chip Bonding, and Injection of Underfill

The fabrication steps up to In bump formation (including it) can be thought as the first part of the T2SL process. Following steps are named as ‘post-process’ from now on. After completing the first part of the T2SL process, samples are diced according to the ROIC size and requirements. The diced samples and ROIC, whose process is also completed, will be hybridized. Hybridization process can be performed in two ways: cold compression and hot compression. ROIC, which is made of Si, is heated below the melting point of In and slightly above room temperature in cold compression. The temperature of the FPA is kept at room temperature or heated less than ROIC. Generally, this technique is used for materials that are very sensitive to temperature, and ones that these temperatures can destroy their characteristics. Contrary to cold compression, both ROIC and FPA is heated up to just below the melting temperature of In, ~156℃, or to that temperature to increase the sticking of

In bumps of both sides. The slight stress is introduced in bumps in cold compression method whereas relatively large stress is introduced in hot compression method. This relatively large stress is originated from different thermal expansion coefficients of Si (ROIC) and FPA (InAs/GaSb T2SL grown on GaSb substrate) during cooling down in hot compression method. Furthermore, these stresses can be hidden in bump structures, and they can come out at cryogenic temperatures. In fact, slight heating of ROIC in cold compression is performed to compensate the introduced stress which reveals at cryogenic temperatures. In T2SL hybridization processes, both compression methods can be used. In this thesis, both compression methods are used, and their stress analyses are performed.

After FCB operation, underfill epoxy is injected to FPA-ROIC hybrid to protect In bumps which can be broken or be deformed during cooling down at cryogenic temperatures. Moreover, this epoxy fills gaps in between ROIC, FPA and In bumps, and it creates the supported ground for substrate thinning operations. Therefore, an underfill should have stand cryogenic temperatures, have low stress at cryogenic temperatures, and have sufficiently enough viscosity to fill gaps. Three different underfill epoxies which meet requirements are used in this thesis work, and one of them is chosen because of its better performance than others.

4.2.7. Substrate Thinning

InAs/GaSb T2SLs are usually grown on GaSb because of close lattice constants of substrate GaSb and epilayer. Epilayer used in this theses is grown on GaSb substrate. The backside illumination of hybridized FPA-ROIC can cause serious problems. The relatively large absorption caused by GaSb substrate in infrared region decreases the sensitivity of device [87]. Moreover, the difference in between thermal expansion coefficients of Si ROIC and T2SL FPA reduces the reliability of FPA by applying stress to In bumps at operation-temperatures below 100 K. Therefore, the substrate should be thinned or removed to avoid these problems. The substrate thinning process is hard to operate due to the fragile nature of both T2SL FPA and Si ROIC, which is relatively more rigid than FPA.

There are some methods used in literature for substrate thinning such as lapping, grinding and chemically etching. In this thesis, the substrate of T2SL FPA is thinned by grinding below 20 μm. The thickness of the GaSb substrate is 625 ± 15 μm in our case.

The chemical etching of the substrate is also performed after grinding it around 20 μm. The substrate is removed completely by chemical etching. In Figure 4.23, SEM images of the grinded substrate are presented. In grinding process, the surface of the substrate is inevitably scratched.

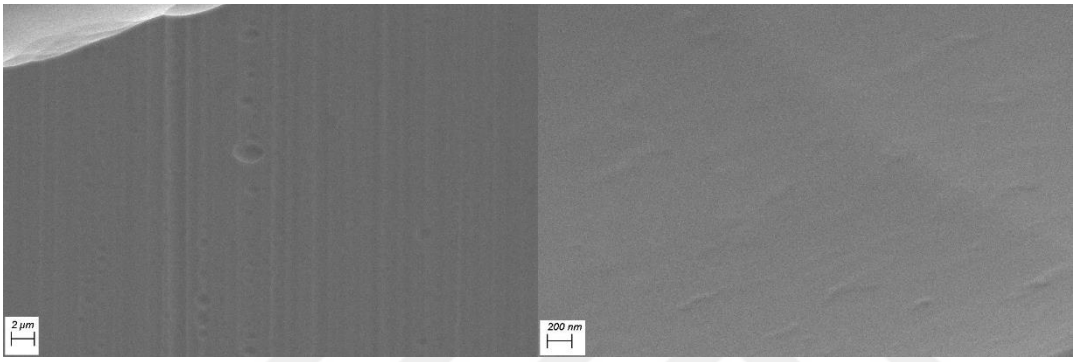

Figure 4.23. SEM images of the grinded substrate.

In Figure 4.24, chemically etched substrate surface after grinding is also presented. In this case, GaSb substrate is not completely removed. The voids formed at grinding cycle expand in such a way that chemicals attack these voids 3-dimensionally.

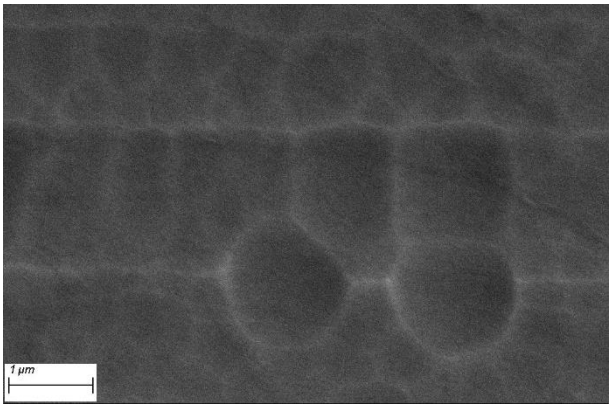

Figure 4.24. SEM images of chemically etched but not completely removed substrate.

The stress issue is not concerned only with the thickness of the FPA, but also it is related to the thickness of the ROIC. For this reason, some detector manufactures thin ROIC, as well. In the case of not to thin ROIC, the thin FPA can crack when it cooled down to cryogenic temperatures due to the difference in thermal expansion coefficients. Thus, ROICs are also thinned in this thesis study.

As thinning operations are completed, T2SL FPA-ROIC hybrid is mounted on LCC sockets, and Au wire connections are performed. The wirebonding process is the final step of the post-process of T2SLs. The hybrid which is connected LCC socket is ready for characterization measurements. All characterization measurements are operated in the LN_2 cooled dewar. In Figure 4.25, the image of LCC in dewar is shown.

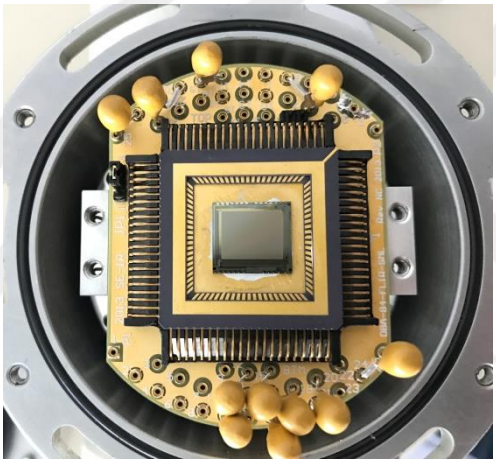

Figure 4.25. FPA-ROIC hybrid on LCC in the dewar.

In this chapter, the fabrication process of T2SL structures is investigated. In this thesis work, the deep research on optimum fabrication is performed, and final fabrication procedure is conducted besides with the investigation of all experiments performed in each step. To sum up, the fabrication procedure of T2SL structure is as follows:

- Mesa structures are formed by using wet etching method with a suitable mixing ratio of H_3PO_4, H_2O_2, and H_2O.
- Ti and Au are used as ohmic contact metals.
- Pixels are isolated from each other and passivated by polyimide with short time wet etching pre-treatment.

- After under bump metallization, deposition of Ti, Ni, and Au, In bumps are formed with a height of about 5.5 μm.
- The same UBM and In bump formation procedure is applied to ROIC with smaller In bump height.
- FPA and ROIC are hybridized with cold compression method.
- The cryogenic underfill is injected.
- GaSb substrate is thinned by grinding up to ~20 um, and chemically etched until the substrate is completely removed, respectively.
- ROIC of the hybrid is thinned about 50 μm, as well.
- The whole proses end up with mounting the thinned hybrid on LCC socket and taking wire bonds.

In the following chapter, the results of different process method, and the characterization of fabricated samples will be presented.

CHAPTER 5

CHARACTERIZATION OF TYPE-II SUPERLATTICE

Starting with the raw material, an infrared detector is obtained with the completion of fabrication steps. Each step of growth and fabrication has effects on device performance either providing enhancement or causing reduction. Therefore, proper characterization should be performed on fabricated detectors in order to understand effects of applied methods on detector performance and to find out possible solutions for problems.

This thesis study focuses on the comparison of fabrication methods over large area diodes in terms of current-voltage characteristics. Moreover, measured dark currents are analyzed by modeling. After the determination of most powerful process scheme according to the characterization results, FPA level characterizations are performed on fabricated FPAs in terms of responsivity, NETD, and acquired images. Specific comparisons that will be presented in this chapter are:

- Comparison of mesa etching methods; wet etching and dry etching
- Etch depth investigation
- The determination of passivation method and material
- Effects of pre-treatment before passivation
- The importance of substrate removal

Large area detector fabrication for fast and easy comparison of the applied procedure is also explained in this chapter. The first three of these experiments were conducted on large area detector structures. The results of the final experiment will be given over images, which are acquired by fabricated samples.

This chapter will cover characterization methods, the I-V performance comparison of applied fabrication steps with large area detector fabrication procedure, the final decision of fabrication process of this thesis study, the dark current modeling, and demonstration of images acquired by fabricated detectors, respectively.

5.1. Performance Comparison of Different Fabrication Methods

In this section, results of previously mentioned fabrication methods will be compared. These comparisons will base on the investigation of I-V characteristics of each method. Before starting the comparisons, it is more convenient to explain large area detector fabrication and I-V measurement setup and conditions.

5.1.1. Large Area Detector Fabrication

The expected pixel dark current level for 15-µm-pitch-MWIR T2SL detectors are around several femtoamperes (fA). I-V measurement systems can be strained to measure those current levels. Thus, larger area detectors are fabricated to obtain reliable and consistent results.

Each large area detector is fabricated with same fabrication procedure. The difference between samples is provided by changing only one parameter that will be compared. For example, mesa formation comparison is performed on samples which differ only by a method of etching. The other parameters such as etch depth, pixel size, and ohmic contacts are kept same. Likewise, for the comparison of passivation methods/materials, samples are fabricated with the same procedure. They are separated each other only by passivation. For the sake of these large area detectors, it is possible to obtain a quick idea about the applied procedure by not needing to complete whole fabrication. In this thesis study, large area detectors size is assigned as 220 µm x 220 µm for all experiments.

5.1.2. I-V Measurement Setup

It is well-known that I-V measurement of T2SL detectors is performed at operational temperature of the detector or at least around that temperature, except for high operating temperature sensors. Therefore, in this thesis study, I-V characteristics of all samples are analyzed at liquid nitrogen temperature (at 77 K). Large area samples are wire-bonded and placed into LN_2 dewar like shown in Figure 4.25. After cooling down dewar, by adding LN_2, the dewar is connected to Keithley 6430 source and measurement unit according to its pin-outs.

5.1.3. I-V Comparison of Applied Fabrication Methods

In this section, I-V characteristics of applied etching methods and passivation methods/materials will be investigated, respectively. All large area detectors are fabricated with same size mesa structures. They differ from each other in terms of the etching method, etch depth or passivation procedures.

5.1.3.1. I-V Comparison of Mesa Etching Methods and Etch Depth Analysis

Both dry and wet etching methods are experimented for mesa formation in this thesis study, as details of them given in Chapter 4. Two large-area-pixel detectors, which have same size mesas, are fabricated with dry and wet etching methods, separately. While an optimized gas mixture of BCl_3, Cl_2, and Ar is used for dry etching as well as Ar plasma post-treatment, $C_6H_8O_7$ / H_2O : H_3PO_4 : H_2O_2 solution with a ratio of 10:1:1 is used for wet etching. Samples are etched up to 2.6 – 2.7 µm depth. The same ohmic contact formation procedure is applied to both samples. After mounting them into LCC, they are wire-bonded separately. In other words, the only difference between two samples is just the etching method used for formation of mesas. I-V measurements are performed at 77 K in the dewar.

The results of this measurement are given in Figure 5.1. While wet etched sample gives $1.3\ x\ 10^{-11}$A dark current at -0.1 V bias, dry etched sample gives $2.5\ x\ 10^{-10}$A dark current at same bias voltage.

Even if dark currents of each sample coincide around -0.05 V bias voltage, dark current of dry etched sample is $10^1 - 10^2$ orders of magnitude larger than the wet etched sample. In addition, the reasons related to why wet etching is chosen are mentioned in Chapter 4. Therefore, wet etching is more suitable etching method for T2SL detectors. However, the dry etching method is not an ignorable method for mesa etching because of advantages that it provides. Further improvements/optimizations should be done to overcome larger dark current that it yields with regard to wet etching.

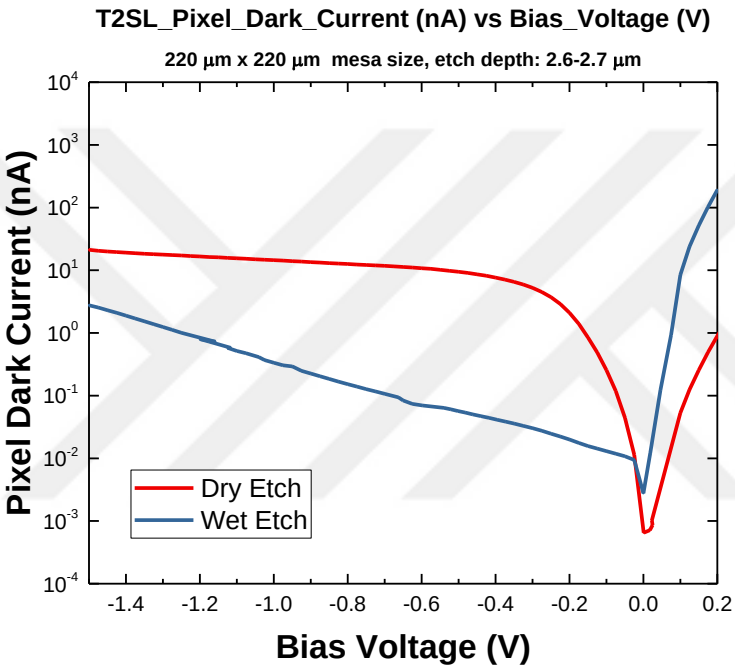

Figure 5.1. Dark currents of 220 µm x 220 µm pixel area samples, etched dry and wet at 77 K.

The design of the T2SL structure is in the form of a p-i-n diode. To investigate the behavior of intrinsic absorber region, etch depth analysis is also conducted. The same large-area diodes are fabricated with same wet etching solution at different etch depths. While one sample is etched up to the n-type region (2.6 – 2.7 µm), the other sample is etched just slight into the intrinsic absorber region (0.6 – 0.7 µm). Remember that intrinsic region starts at 0.5 µm while n-type region starts at 2.5 µm in our design. After the formation of mesas, same ohmic contacts are formed on both samples. The result of I-V measurement is shown in Figure 5.2.

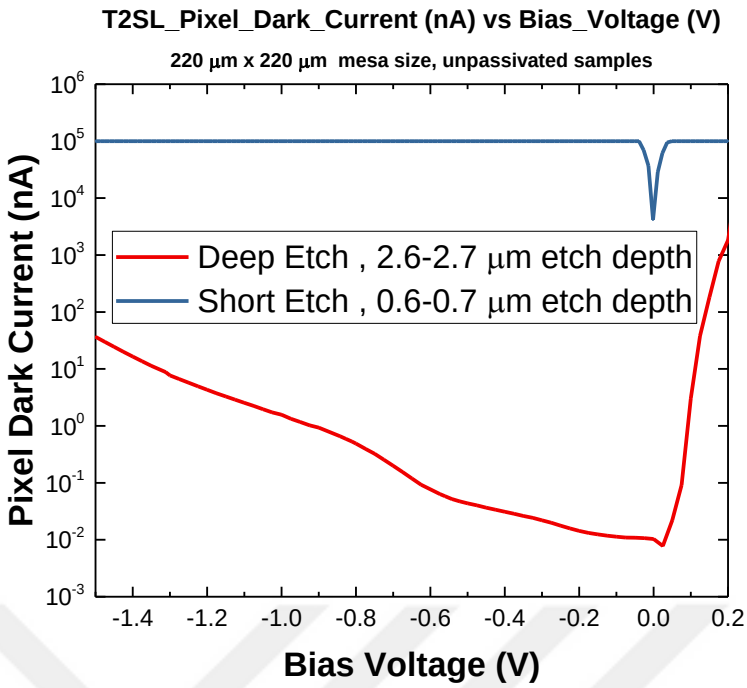

Figure 5.2. I-V characteristics of deep and short etch-depth samples sized 220 µm x 220 µm at 77 K.

Differently etched samples are not passivated. It can easily be seen from Figure 5.2 that there are not diode characteristics in short etched sample. This means that the behavior of intrinsic absorber is p-type. Because of the p-type behavior of absorber region (here, contacts are taken as if it is an n-side of the circuit), current corresponding to applied bias voltage cannot be measured. As a result of this investigation, T2SL detectors fabricated in this work should be etched up to n-type region.

5.1.3.2. Determination of Passivation Method and Material

The fabrication details of passivation methods/materials are given in Chapter 4. Current-voltage characteristics of these methods/materials are also studied in this work. I-V characteristics are measured on large pixel area samples. All samples are fabricated with the same procedure. Specifically, they are etched with a same wet etchant at same etch depth, and ohmic contacts of each sample are formed in the same way. The only difference between them is the passivation method or material.

Also, all measurements are performed at 77 K. The results of I-V measurements are shown in Figure 5.3. In order to compare the effect of $(NH_4)_2S$ pre-treatment, I-V measurement results of this sample are also given in Figure 5.3.

PECVD SiO_2 coated and $(NH_4)_2S$ pre-treated plus PECVD SiO_2 coated samples' passivation openings are performed with same dry etching chemistry (CHF_3). Holes are opened in photoresist passivated sample just by developing exposed parts of photoresists. This method is used for uncured polyimide samples, as well. O_2 plasma ashing is used to open cured polyimide samples' contact holes. E-beam SiO_2 sample openings are obtained by using lift-off technique, which is mentioned in Chapter 4.

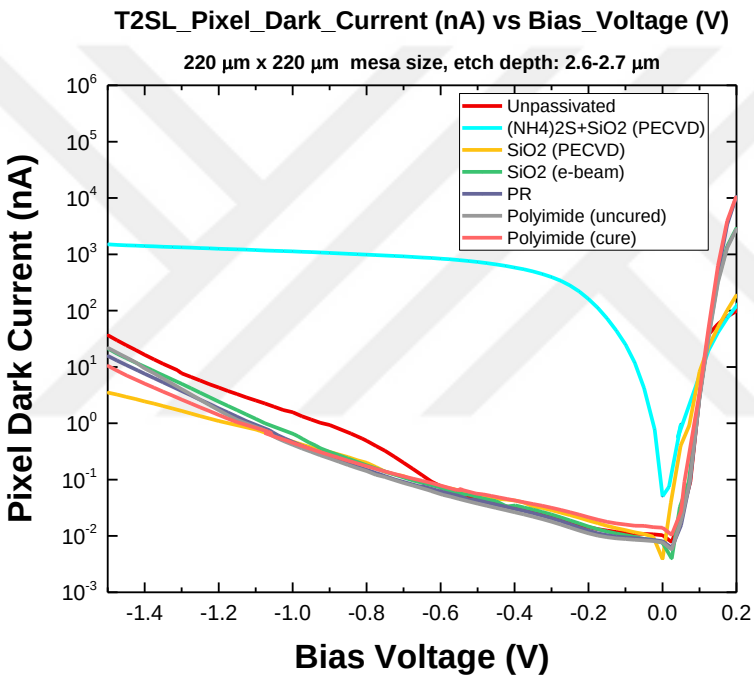

Figure 5.3. The dark current comparison of different passivation methods/materials at 77 K.

From Figure 5.3, $(NH_4)_2S$ pre-treated sample gives highest dark current. Actually, its dark current is $2\ x\ 10^3$ times larger than SiO_2 PECVD sample. The only difference between two samples, whose one-to-one comparison given in Figure 5.4, is $(NH_4)_2S$ pre-treatment.

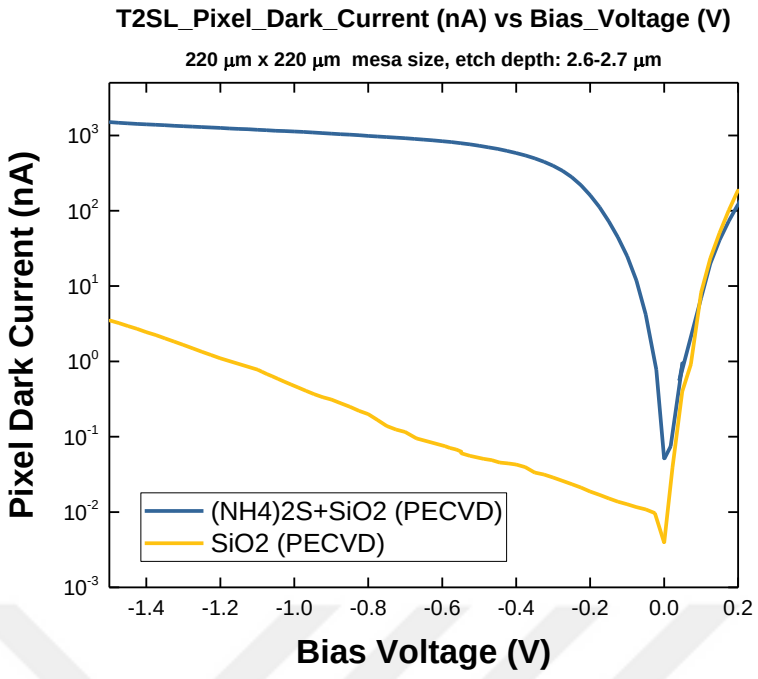

Figure 5.4. The dark current comparison of $(NH_4)_2S$ pre-treated sample with SiO_2 PECVD sample at 77 K.

The time which samples are exposed to $(NH_4)_2S$ is vital to obtain proper treatment [86]. When exposing time exceeds some limit, this solution starts to etch sample. Moreover, the concentration of ammonium sulfide, which is generally diluted with H_2O, in solution affects the dynamic resistance of sample at almost all bias voltages [86]. As it is stated in Section 4.2.4, pre-treated sample is soaked with $(NH_4)_2S$: H_2O (1:20) for 2 minutes. The reason for this high dark current can be either concentration of the solution or soak time. Therefore, for $(NH_4)_2S$ pre-treatment optimization can be performed to lower dark current. Reduction in FPA image quality caused by high dark current of ammonium sulfide pre-treatment will be shown in Section 5.4. Moreover, FPA images of PECVD SiO_2 passivated and PECVD SiO_2 passivated plus $(NH_4)_2S$ pre-treated will be compared.

In Figure 5.5, dark current results of passivation methods at lower biases are given. $(NH_4)_2S$ pre-treated samples' I-V curve is omitted from this figure, because of the highest dark current value of it. The dark current values at -0.1 V are given in Table 5.1.

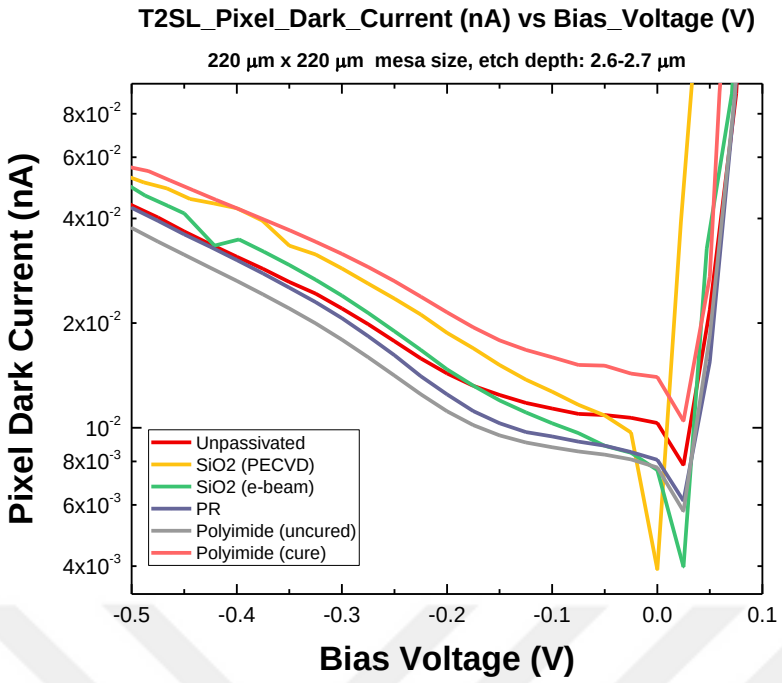

Figure 5.5. The dark current comparison of different passivation methods/materials at 77 K.

Table 5.1. Dark Current values of passivation methods/materials at -0.1 V at 77 K.

Passivation Method/Material	**Dark Currents of 220 µm x 220 µm pixel at -0.1 V at 77 K (A)**	**Calculated Dark Currents of 10 µm x 10 µm pixel at -0.1 V at 77 K (A)**
Un-passivated	1.1×10^{-11}	2.27×10^{-14}
SiO2 (PECVD	1.2×10^{-11}	2.48×10^{-14}
$(NH_4)_2S + SiO_2$ (PECVD	2.5×10^{-8}	5.2×10^{-11}
SiO2 (E-beam)	1×10^{-11}	2.06×10^{-14}
Photoresist (PR)	9.4×10^{-12}	1.94×10^{-14}
Polyimide (Uncured)	8.7×10^{-12}	1.8×10^{-14}
Polyimide (Cured)	1.5×10^{-11}	3.1×10^{-14}

As it can be seen from Figure 5.3, Figure 5.5 and Table 5.1, except for $(NH_4)_2S$ pre-treated sample, dark currents for all methods are almost at the same level. To illustrate, cured polyimide passivated sample yields $1.5\,x\,10^{-11}$A dark current whereas PECVD SiO_2 passivated samples gives $1.3\,x\,10^{-11}$A at same bias voltage of -0.1 V. It is also observed that polyimide gives relatively low dark current result regardless of being cured or uncured. Its ability to yield low dark current makes polyimide the best choice for passivation material. Moreover, the surface of FPA consists of mesa structures which means surface is wavy. Polyimide provides opportunity to compensate this wavy surface. In other words, it provides surface planarization besides with conformal coating.

From the measured dark currents, it is possible to obtain dark current densities of these passivation methods/materials. The dark current densities of applied passivation methods/materials are shown in Figure 5.6 and Figure 5.7. It is good to state that the polyimide results which are shown in Figure 5.3, Figure 5.5, Figure 5.6, and Figure 5.7 is for Poly-b.

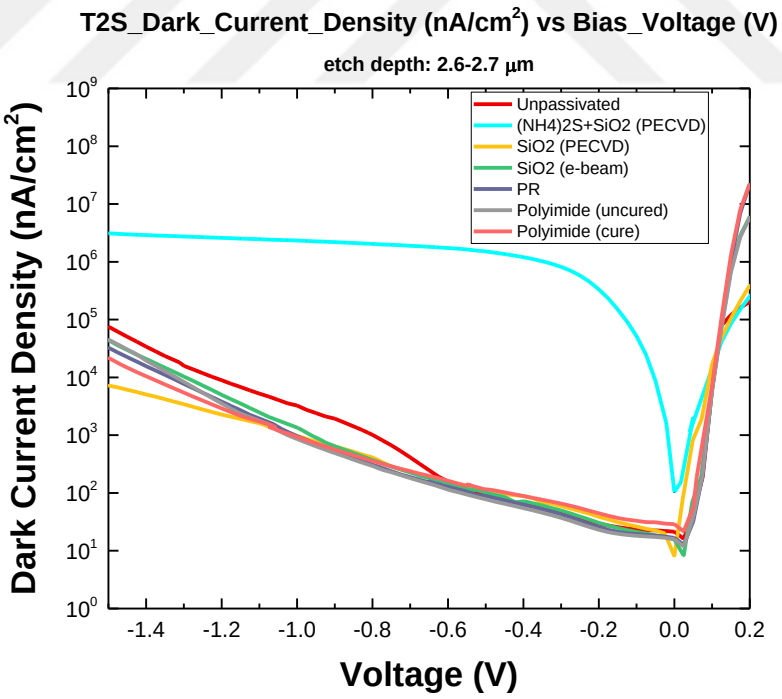

Figure 5.6. Dark current densities of passivation methods and materials.

As it is expected, $(NH_4)_2S$ pre-treated sample gives the highest dark current density. It is almost 10^3 times higher than others at larger reverse bias voltages. At lower biases, difference increases almost up to 10^5 times. In Figure 5.7, dark current densities of these passivation methods/materials are given at lower reverse bias voltage.

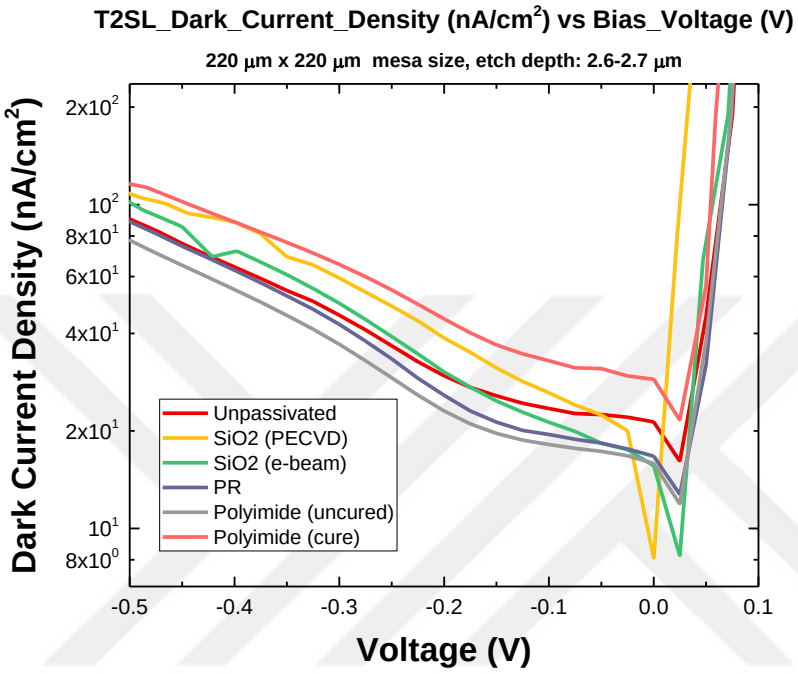

Figure 5.7. Dark current densities of passivation methods and materials.

I-V curve of $(NH_4)_2S$ pre-treated sample is omitted from Figure 5.7 because of its highest dark current density. Similar to dark current results, all samples yield almost same dark current densities. For instance, the dark current density is 3.2×10^{-8} A/cm^{-2} for cured polyimide at -100 mV.

As it is stated above, polyimide results shown in previous figures belong to poly-b. To investigate the differences between two polyimides which are used in this work, their dark currents are measured. The dark current comparison of these polyimides is given in Figure 5.8 and Figure 5.9. For this measurements, samples are fabricated with the same procedure, and polyimides are spin coated on these samples. Same curing procedure is applied to these samples.

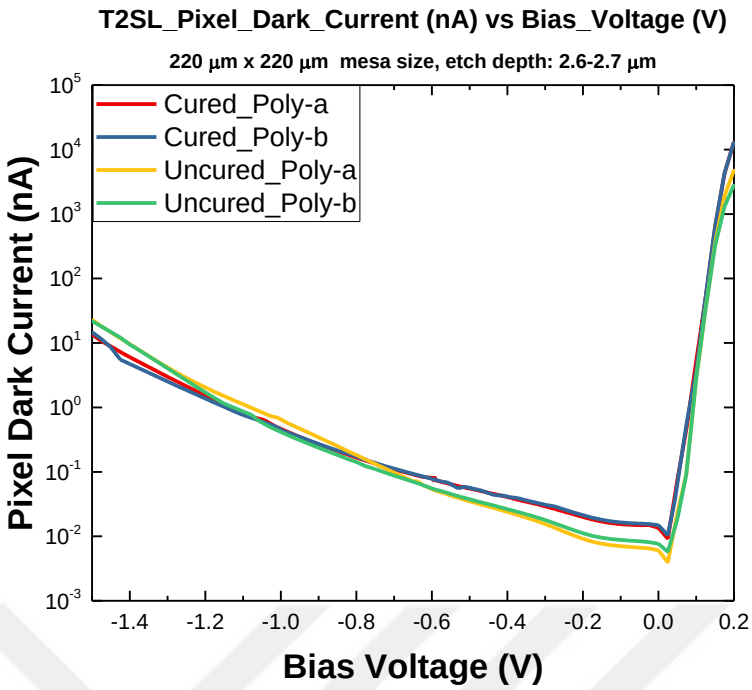

Figure 5.8. Dark current comparison of cured and uncured polyimides.

For both cured and uncured polyimides, dark current levels are almost same. However, when dark currents are investigated, varying dark current properties can quickly be seen concerning cured and uncured polyimides. While dark currents of uncured polyimides are higher than cured ones at larger bias voltages, cured polyimides show larger dark currents at lower reverse bias voltages. They coincide with each other around -0.8 V. However, their behavior at low bias region is more important than any other bias regions since the operational bias voltage for T2SL detectors is around -50 mV. When their dark currents are compared at a low bias voltage, they are very close to each other. To illustrate, dark currents are equal to $8.7\ x\ 10^{-12}$A and $7\ x\ 10^{-12}$A for uncured poly-b and poly-a, respectively. Cured poly-b and poly-a yields $1.64\ x\ 10^{-11}$A and $1.54\ x\ 10^{-11}$A, respectively. All values are for 0.1 V reverse bias voltage. However, Poly-b is chosen as a passivation material of this work since expansion of Poly-a in 3-dimension causes stress and disturbance in conformal surface which is stated in Section 4.2.3.3.

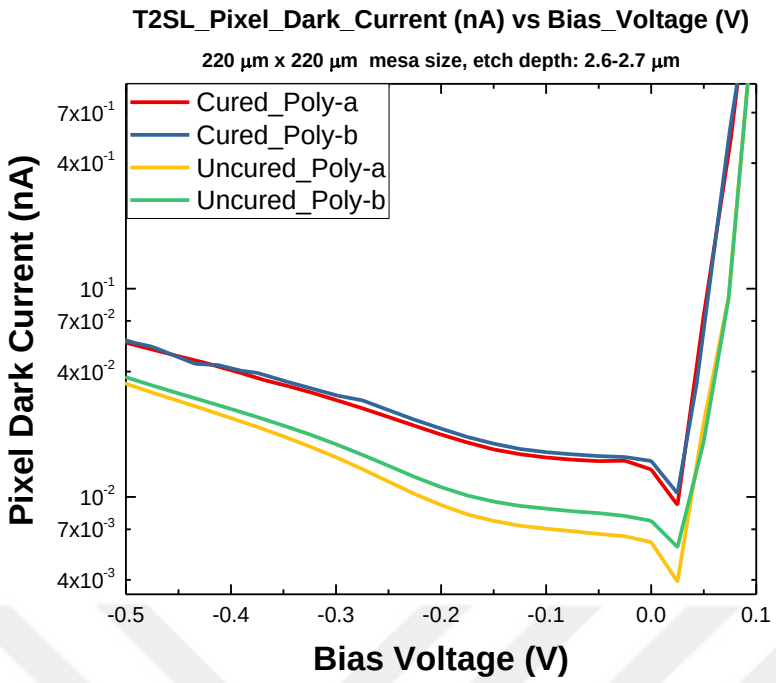

Figure 5.9. Dark current comparison of cured and uncured polyimides.

In Figure 5.10 and Figure 5.11, photo-currents of differently passivated samples are compared. Photo-current given in this graph for polyimide is for Poly-b. These measurements are performed at 77 K. All samples are illuminated at the front side of each.

As it can be seen from Figure 5.10, $(NH_4)_2S$ pre-treated samples' result differs from others like in dark current measurements. Also, the photo-current of $(NH_4)_2S$ pre-treated sample changes its slope around -0.2 V. This is unexpected behavior for photocurrent. Generally, the photocurrent of an ideal detector does not alter much with changing bias. The reason for this unexpected behavior can be understood by comparing dark current and photocurrent figures of $(NH_4)_2S$ pre-treated sample. Once they are compared, it can be easily seen that photocurrent is almost suppressed by dark current especially at high voltages. Actually, results that are seen in photocurrent measurement belong to dark current at larger bias voltages. In other words, since dark current suppresses the photocurrent up to -0.2 V, it is impossible to observe photocurrent of the ammonium sulfide pre-treated sample at large reverse bias voltages.

However, with the decrease in dark current around -0.2 V, the photocurrent of this sample start to show itself. When getting closer to 0 bias region, the effect of dark current on photocurrent lowers. Results that are seen in between -0.2 V to 0 V interval are the sum of dark and photocurrents for the ammonium sulfide pre-treated sample.

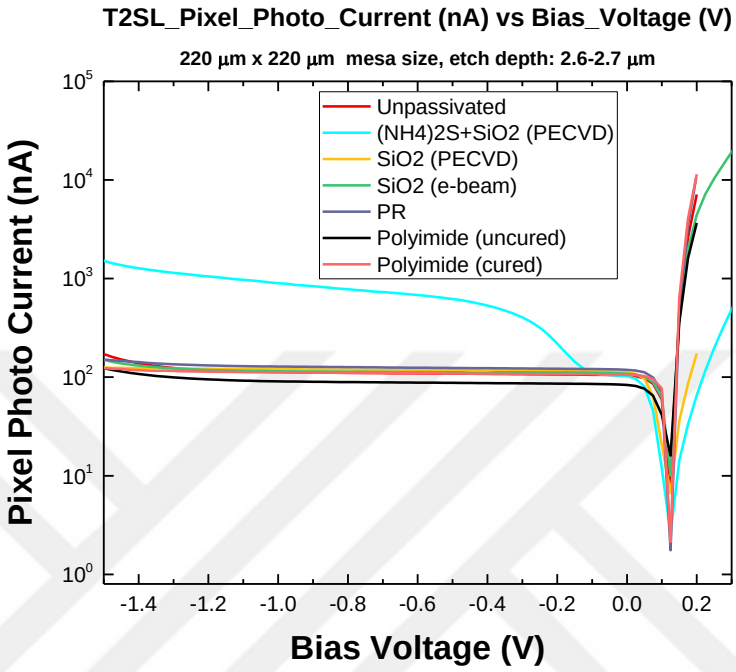

Figure 5.10. Photocurrent of differently passivated samples at 77 K.

However, there is no significant difference between other samples. In Figure 5.11, photo-currents of all samples are shown at lower bias voltages. All samples have $\sim 1.0\ x\ 10^{-7}$A photo-current at 0.1 V reverse bias voltages. Photoresist passivated sample yields highest result whereas uncured polyimide sample shows lowest photo-current at these low bias voltages. However, the difficulty in photoresist passivation process makes it less favorable. Remember that photoresist can dissolve other photoresists which are applied in following fabrication steps. When polyimide results are investigated, it can be easily seen that curing the polyimide increases the photo-current of polyimide around 1.2 times than without curing applications. Even if photo-current of polyimide seems to be lower than photoresist and SiO_2, this decrease can be tolerated in order to get smoother and more planar surfaces, and stable passivation layer, which is provided by polyimide passivation.

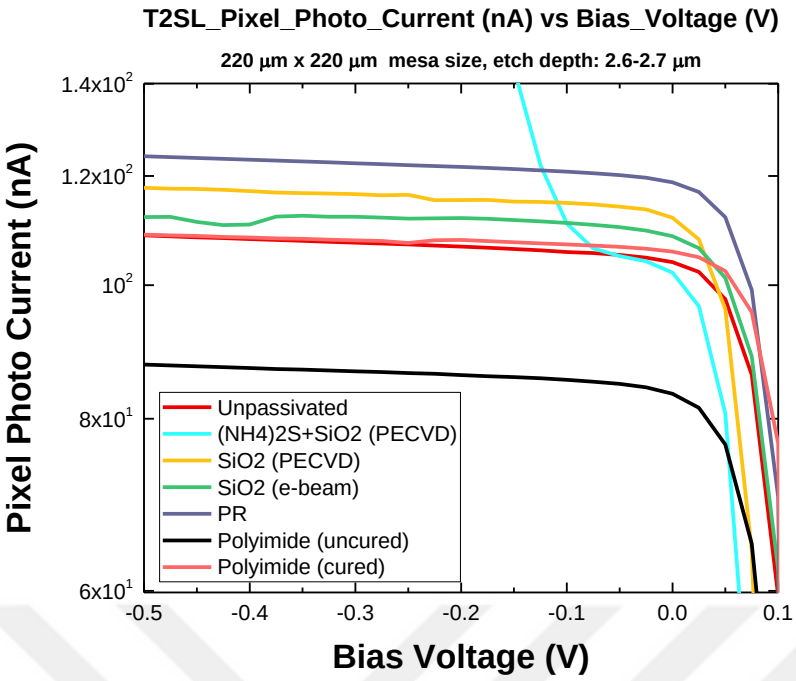

Figure 5.11. Photocurrent of differently passivated samples at 77 K.

In Figure 5.12, the ratio of photo-current over dark current of each sample is given for related bias voltages. From Figure 5.12, the photo-current to the dark current ratio of $(NH_4)_2S$ pre-treated sample is the lowest one. This is not an unexpected outcome since the dark current of ammonium sulfide suppresses photo-current up to around -0.2 V, as it is explained before. In fact, photo-current is suppressed entirely by dark current especially at high voltages. Photoresist and SiO_2 e-beam passivated samples give the highest ratio among others. Their ratio is equal to 12805 and 10772 for photoresist and SiO_2 e-beam, respectively. However, the quality of SiO_2 films, deposited by e-beam technique, is suspicious. The difficulty in the fabrication process for photoresist passivation namely possibility of dissolution of photoresist in the following step of fabrication may create obstacles and undesired consequences. Moreover, it is known that SiO_2 passivation behaves like an anti-reflection coating, which provides a reduction in reflection of photons, whereas polyimide layer absorbs some of the incoming photons before reaching the diode in front side illumination. Thus, photo-current of polyimide passivation reduces in for front side illuminations. It is estimated that photo-current will have increased in back-side illumination.

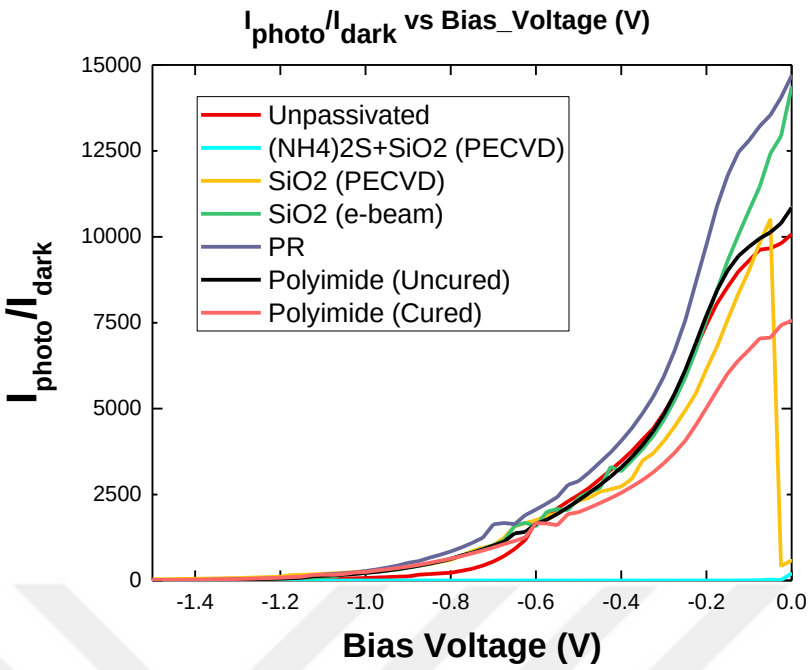

Figure 5.12. The photo-current over the dark current ratio of differently passivated samples with varying bias voltage.

Therefore, for the sake of stability and repeatability of fabrication, the choice of polyimide for passivation step is still the best one for this application. This is valid even though its photo-current over dark current ratio, which equals to 6710, seems to be relatively lower among some others.

Another comparison is about dynamic resistances of passivation methods/materials. The $R_0.A$ products of differently passivated samples are given in Figure 5.13. It is well-known that the physical meaning of this product is to give idea about where the detector is biased. As it is seen from this figure, the highest value of $R_0.A$ is obtained with un-passivated sample. Otherwise, $(NH_4)_2S$ pre-treated sample yields the lowest result. In fact, it is not easily seen in the level of others. Therefore, it value is multiplied by a factor of 10^3 to make comparison easy. Its actual value is 10^6-10^7 order lower than the others. Moreover, $(NH_4)_2S$ pre-treatment peak value of $R_0.A$ shifts towards larger, even positive, bias regions.

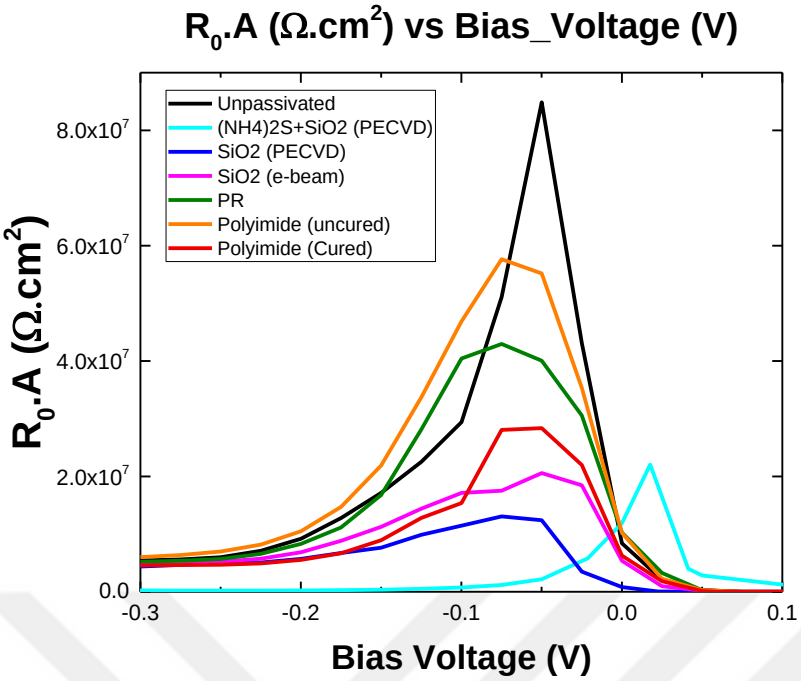

Figure 5.13. R_0. A product of differently passivated samples.

From inside of passivation applied samples, polyimide passivation without curing gives the best result. Likewise, cured polyimide passivation has un-ignorable $R_0.A$ product value even if curing the polyimide lowers the value of $R_0.A$ product. Furthermore, cured polyimide passivation gives the highest $R_0.A$ value of itself at 0.05 reverse bias voltage, which is the typical biasing value for infrared devices. Actually, this corresponding bias voltage for highest $R_0.A$ value is our bias voltage value which T2SL detectors operate.

5.2. Dark Current Modeling of T2SL

The dark current mechanisms observed in an infrared device are given in Chapter 3. The main dark current mechanisms for T2SLs are diffusion current, generation-recombination (G-R) current, band-to-band tunneling current and trap-assisted tunneling current. In this section, the dark current of polyimide passivated sample will be modeled in accordance with the dark current mechanisms generally observed in the T2SL devices. Modeling will be performed on dark current results which are measured at 77 K.

Before starting, some critical parameters used in this modeling will be demonstrated besides with fundamental equations and assumptions.

The equation of diffusion current is stated in Equation (3.2). However, the material dependent parameters such as n_i and E_g should also be given for T2SL modeling. The equation for n_i can be given as [88],

$$n_i = 2\left(\frac{2\pi k_B T}{h^2}\right)^{3/2} (m_e^* m_h^*)^{3/4}\, exp\left(-\frac{E_g}{2k_B T}\right) \tag{5.1}$$

where h is the Planck's constant, E_g is the band-gap of T2SL, and $m_{e,h}^*$ are the effective masses of electron and hole. The band gap of T2SL is interpreted as [89],

$$E_g = 0.234 - 3.1x10^{-4}\left(\frac{T^2}{T + 270}\right) \tag{5.2}$$

Effective masses of electron and holes are calculated with the following relation;

$$m_{e,h}^* = \sqrt[3]{\left(m_{e,h\parallel}^*\right)^2 m_{e,h\perp}^*} \tag{5.3}$$

where $m_{e\parallel}^* = 0.0235m_0$, $m_{e\perp}^* = 0.0275m_0$, $m_{h\parallel}^* = 0.0342m_0$ and $m_{h\perp}^* = 79.8m_0$ [90].

The G-R current formula is given in Equation (3.3). However, for $T = 77$ K, the term $k_B T = 6$ mV. With the assumption of $\tau_e = \tau_h \neq \tau_{gr}$, Equation (3.3) can be re-written as,

$$J_{gr} \approx \frac{q n_i w}{\tau_{gr}} \frac{V}{V_{bi} - V} \tag{5.4}$$

where w is the depletion region width, τ_{gr} is the generation-recombination lifetime of electron-hole pair, and V_{bi} is the built-in voltage.

w and V_{bi} can also be given as [28],

$$w = \sqrt{\frac{2\varepsilon_s}{q}\left(\frac{1}{N_A} + \frac{1}{N_D}\right)(V_{bi} - V_a)} \tag{5.5}$$

and

$$V_{bi} = \frac{k_B T}{q} ln\left(\frac{N_A N_D}{n_i}\right) \tag{5.6}$$

where ε_s is the static dielectric constant and V_a is the applied voltage.

The equation for trap-assisted tunneling current is given in Equation (3.4). By assuming of energy level of trap is located in mid gap of energy band gap of T2SL meaning that

$$E_t = \frac{E_g}{2} \tag{5.7}$$

At this point, $E(V)$ is at its maximum value. The equation for $E(V)$ can be written as,

$$E(V) = \frac{qN_D}{\varepsilon}\chi_n \tag{5.8}$$

where χ_n is the width of depletion region being into n-side of junction which is assumed to be $\chi_n = w/2$.

The expression of the band to band tunneling is given in Equation (3.5). The assumptions of trap-assisted tunneling are also valid for band-to-band tunneling.

After giving assumptions, simplifying dark current equations, and calculating the other parameters in accordance with equations given in this section, parameters used in this modeling are listed in Table 5.2.

Table 5.2. The fitting parameters for simulating dark current of the InAs/GaSb T2SL detector.

Parameter	Value	Unit	Parameter	Value	Unit
n_i	$3.671x10^9$	cm^{-3}	w	$variable$	cm
q	$1.602x10^{-19}$	C	τ_{gr}	4.2	ns
k_B	$1.38x10^{-23}$	J/K	V_{bi}	0.227	V
T	77	K	ε_s	15.42	$-$
N_D	$1x10^{17}$	cm^{-3}	π	3.14159	$-$
N_A	$1x10^{17}$	cm^{-3}	m_T	$0.035m_0$[91]	kg
μ_h	1000 [60]	$cm^2/V.s$	M^2	10^{23}[92]	eV^2cm^3
μ_e	10000 [60]	$cm^2/V.s$	N_T	$7.9x10^{13}$[60]	cm^{-3}
τ_h	0.02 [60]	ns	h	$6.62x10^{-34}$	$J.s$
τ_e	0.02 [60]	ns	$E_T = E_g/2$	0.1143	eV
V=V_a	$variable$	V	$E(V)$	$variable$	V/m
m_e^*	$0.0247m_0$	kg	ε	15.7	F/m
m_h^*	$0.454m_0$	kg	χ_n	$variable$	cm
E_g	0.2287	eV	m_0	$9.11x10^{-31}$	kg

In this model, the primary dark current mechanisms namely diffusion current, generation-recombination current, trap-assisted tunneling current, and band-to-band tunneling current is used as it is stated before. The measured dark current is treated as the total dark current. Therefore, total dark current is expressed as,

$$J_{measured} \equiv J_{total} = J_{diff} + J_{G-R} + J_{TAT} + J_{btb} + J_{shunt} \tag{5.9}$$

However, after initial calculations, it is found out that trap-assisted tunneling and band-to-band tunneling current is so low that they cannot contribute to total current efficiently. Hence, they are omitted from the calculation. Also, the additional current mechanism is added into modeling. Since perfect isolation of detector from external radiation sources is not possible, there always exist some amount of photo-current. This additional current source is named as $J_{backgorund}$, and it is assumed to be constant through whole bias sweep except for near 0 zero bias.

The last current mechanism is the shunt current. The shunt current is treated as if it has ohmic contact behavior. The change in shunt current with varying bias voltages strongly depend on the dynamic resistance of a detector at corresponding biases. In Figure 5.13, $R_0.A$ products of differently passivated materials were presented. The dynamic resistance values for cured polyimide sample are extracted from this figure. The relation between voltage and resistance is expressed with basic relation as,

$$V = I \cdot R \tag{5.10}$$

where V is the applied voltage, and R is the dynamic resistance. After re-ordering and converting current to current density, Equation (5.10) becomes,

$$J_{shunt} = \frac{V}{R_0 A} \tag{5.11}$$

where A is the area of detector.

Consequently, total current can be expressed as,

$$J_{measured} \equiv J_{total} = J_{diff} + J_{G-R} + J_{background} + J_{shunt} \tag{5.12}$$

Using defined parameters and assumptions, the dark model for InAs/GaSb Type-II Superlattice is obtained, and it is shown in Figure 5.14, Figure 5.15, and Figure 5.16. The modeling figure divided into three parts for easy visualization.

In Figure 5.14, the simulation result is shown in between -1.5 V to -1 V. As it can be seen from this graph, measured dark current and model fitting matches perfectly at higher reverse bias voltages. When dark current mechanisms are investigated, diffusion current and background current are invisible in this range. It means that their contribution to total dark current is low. In fact, they do not effectively contribute to dark current at high bias voltages. It is good to remind that trap-assisted tunneling and band-to-band tunneling currents are discarded from graph showing because of their so low values that do not affect total dark current. In other words, these two mechanisms are suppressed in our T2SL structure with proper band-gap engineering design.

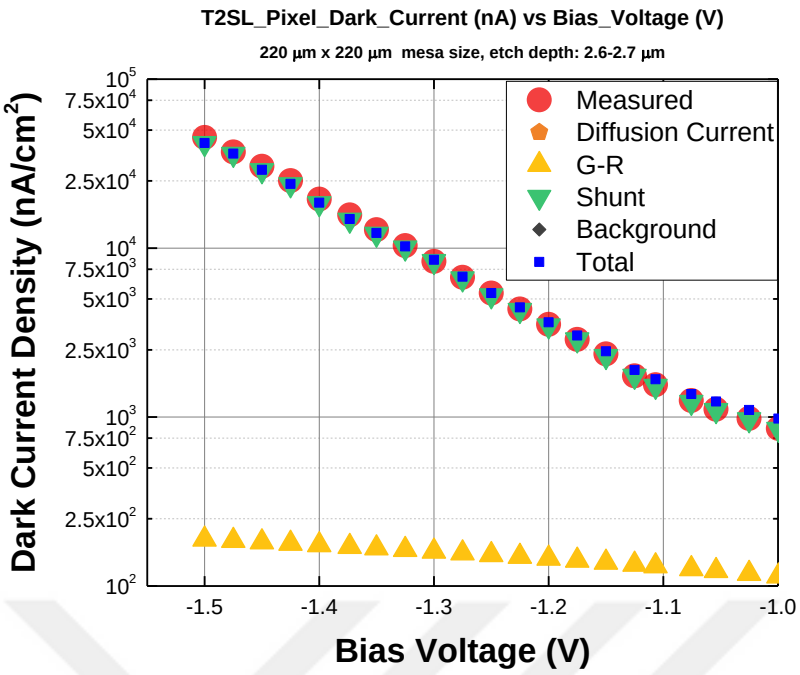

Figure 5.14. The result of dark current simulation in between -1.5 V and -1.0 V.

The main dark current mechanism is the shunt current for this bias range even if G-R current seems to be valid in the graph. G-R current is around $2\ x\ 10^{-7}$A at -1.5 V while shunt current gives almost $5\ x\ 10^{-5}$A dark current at same voltage. Therefore, total dark current is dominated only by shunt current at higher reverse biases. The contribution of G-R current to total dark current is neither ignorable nor significantly considerable. Especially, getting closer to -1 V, G-R current affects total current more than that affects at higher voltages. However, the dominant source is still shunt current. The superior behavior of shunt current at this bias range is totally expected due to low dynamic resistance of detector at this bias range.

In Figure 5.15, the result of modeling in a range of -1 V to -0.2 V is given. As it can be seen from Figure 5.15, the affectivity of shunt current continues up to near -0.8 V. However, the contribution of G-R current is considerably high at this bias range. In other words, the dominant dark current mechanisms in between -1 V and -0.8 V is the combination of shunt current and G-R current. The effectiveness of this combination proceeds up to -0.6 V.

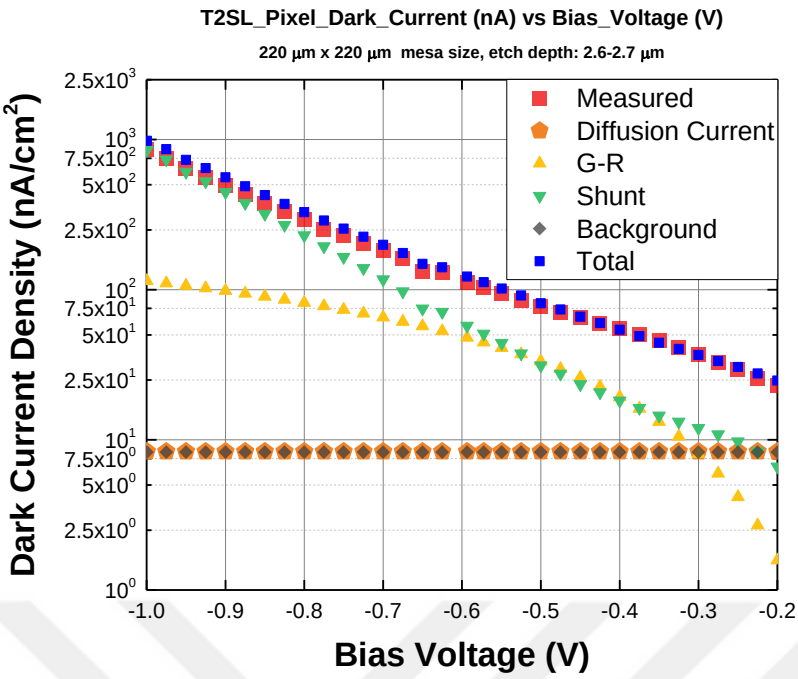

Figure 5.15. The result of dark current simulation in between -1 V and -0.2 V.

Diffusion and background currents are at same level as shown in the figure. Beginning at -0.6 V, they start to get involved in the total current. Around -0.5 V, G-R passes through the shunt. However, together with the decrease in shunt and G-R currents at -0.5 V, the contribution of diffusion and background increase. After a dramatic decrease in G-R around -0.3 V, diffusion and background lift their effectiveness. However, the effect of the shunt on total current is still high. Therefore, while total current is the combination of shunt current and G-R current in between -1 V and -0.6 V, the total current is effectively made up of diffusion current, background current and shunt current in between -0.6 V and -0.2 V.

Figure 5.16 demonstrates the simulation results starting from -0.8 V to 0.05 V. For easy visualization and to compare dark current mechanisms continuously, the graph is started at -0.8 V even though -0.8 V to -0.2 V interval is already shown in Figure 5.15. Effective dark current mechanisms in the region of -0.8 V to -0.2 V has already explained. -0.2 V to 0.05 bias region will be investigated with this figure.

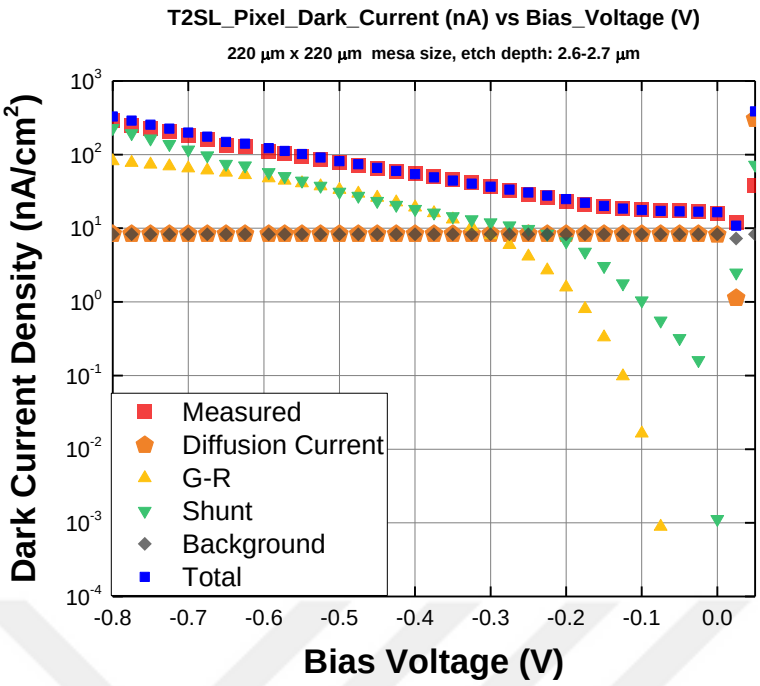

Figure 5.16. The result of dark current simulation in between -0.8 V and 0.05 V.

The decrease in G-R current is firstly observed at -0.3 V, and it gets sharper by getting closer to lower bias voltages. With this decrease, it loses its effect on the total dark current. Likewise, shunt current also reduces after -0.2 V even if its slope is not as sharp as G-R currents'. In near 0 bias voltages, dark current is dominated by background current and diffusion current. Therefore, the current modeling can be summarized as;

- Shunt current dominates dark current at higher reverse bias voltages. Its domination continues individually up to -1 V.
- In between -1 V and -0.8 V, G-R current starts to contribute total dark current efficiently.
- In reverse bias 0.8 V – 0.6 V interval, shunt current and G-R current are decisive.
- Diffusion current and background current begins to contribute total dark current in between -0.6 V and -0.3 V.
- After a sharp decrease in G-R and a relatively high decrease in shunt, diffusion and background currents dominate total dark current from -0.3 V to 0.05 V.

The level of total dark currents is so low that they cannot significantly affect the total performance of the entire system. These low levels of dark currents were expected since the design of T2SL used in thesis study is engineered to subdue the tunneling currents like it is restrained in the nature superlattice structures. Moreover, cooling down the detector at liquid nitrogen temperature reduces the diffusion and G-R dark currents, which they decrease due to the dependence of them to intrinsic carrier concentration (n_i) that directly depends on T. Actually, the diffusion current decreases faster than G-R current since it depends upon n_i^2, while G-R is related to n_i. Therefore, it is safe to state that the detector is only limited by the shunt current which is already at acceptable level when dynamic resistance results are compared to literature. This modeling also proves that the T2SL detectors fabricated in this thesis study can operate higher temperature.

5.3. NETD and Responsivity Measurements

After giving the current-voltage characteristics of large area detectors, the FPA level characterizations will be presented in this section. There are lots of performance characterization methods at FPA level. However, the most fundamental ones are NETD and responsivity. In Chapter 2, the physical meanings of these facts are given. Thus, the results of their measurements will only be presented in this section.

5.3.1. Responsivity and NETD Measurement Setups

NETD and responsivity measurements are performed using a blackbody, a dewar, and a software. Computer records images of two scene which have different temperatures, and Octave script, which was written for this measurement and given in Appendix A, calculates their values regarding digital levels. The script also finds out responsivity, noise, NETD, and bad pixel mappings in terms of being high or being low according to pre-defined threshold values for each. Moreover, the operability, which is another important criterion for infrared detectors that demonstrates the ratio of working pixel to total pixel, can also be calculated by this script.

5.3.2. NETD and Responsivity Measurements

NETD measurement results for T2SL FPA which is fabricated at the early stage of thesis study will be presented in this section. NETD measurements are performed at two different-scene temperatures 300 K and 310 K. Also, $f/2.3$ optics is used. The integration time for this measurement is 2 ms. As it is stated in previous section, the result of this measurement includes some other performance criteria such as high and low noise mapping, NETD mapping, responsivity mapping, hot and cold frame averages, total bad pixel mapping, and high NETD mapping. In this script, threshold coefficients are defined as 0.5, 2, 3 and 3 for low responsivity, high responsivity, bad NETD and bad noise, respectively. Pixels yielding results that are lower than the product of mean responsivity and low responsivity threshold are marked as low response bad pixels. This condition is also valid for other parameters. Specifically, pixels having value that higher than product of mean responsivity value and high responsivity threshold are marked as high response bad pixel. The same idea can be modified for bad NETD and bad noise definitions. The results of FPA level mapping is given in following figures.

In Figure 5.17, cold and hot frame averages are demonstrated. The x and y-axis of mapping correspond to pixel locations. In other words, the mapping shows (x , y) coordinated pixels frame averages. This feature is valid for all mappings demonstrated in this thesis study.

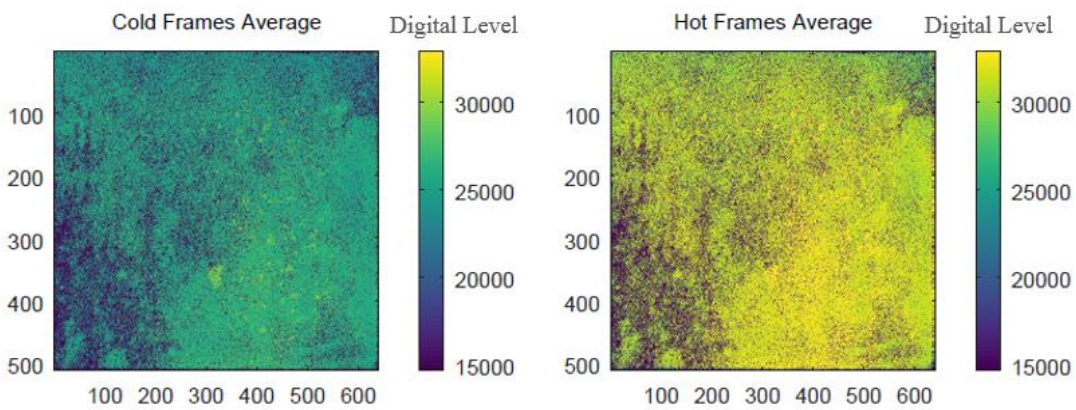

Figure 5.17. Cold and hot frame averages for 640 x 512 T2SL FPA.

The non-uniformity over entire FPA is observed. The reasons for this uniformity problem will be explained later. In a region which belongs (0 , 0) to (200 , 300) coordinated pixels locations, the rise in uniformity draws attention. Most of the pixels located in this region are open pixels. In this region, either In bumps of FPA and ROIC do not touch each other or one (maybe both) of the In bumps are broken in FCB proses. This region gives almost zero response for cold and hot scene radiations. In fact, this is one of the reasons to be named as open. These pixels are treated as bad pixels, and this location is called as 'bad location' from now on. Moreover, these pixels yield higher noise than other regions of FPA, and this feature is shown in Figure 5.18 in terms of noise and high noise mapping.

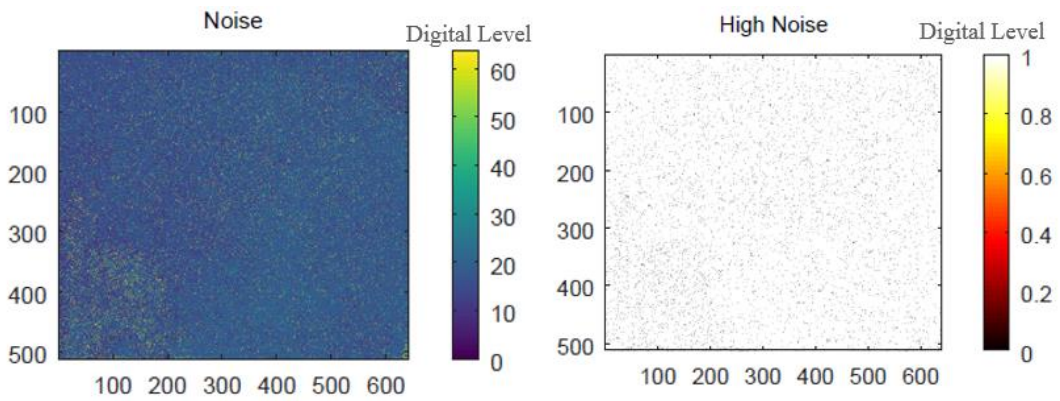

Figure 5.18. Noise and high noise mappings for 640 x 512 T2SL FPA.

It can be easily observed in Figure 5.18 that the pre-defined bad pixel location yields higher noise than any other location, even if some small group or single pixels gives high noise. The comparison scale for noise is in the digital level unit. In addition to their high noise property, this location also gives different NETD and responsivity values compared to other parts of FPA. NETD and responsivity mappings are shown in Figure 5.19. The scale bars represent NETD value in mK and responsivity value in digital level. When this location is investigated according to the scale bar, they yield almost 0 K NETD. This also proves that they are open pixels. The responsivity feature of this location is also different than others. In fact, they do not give any response.

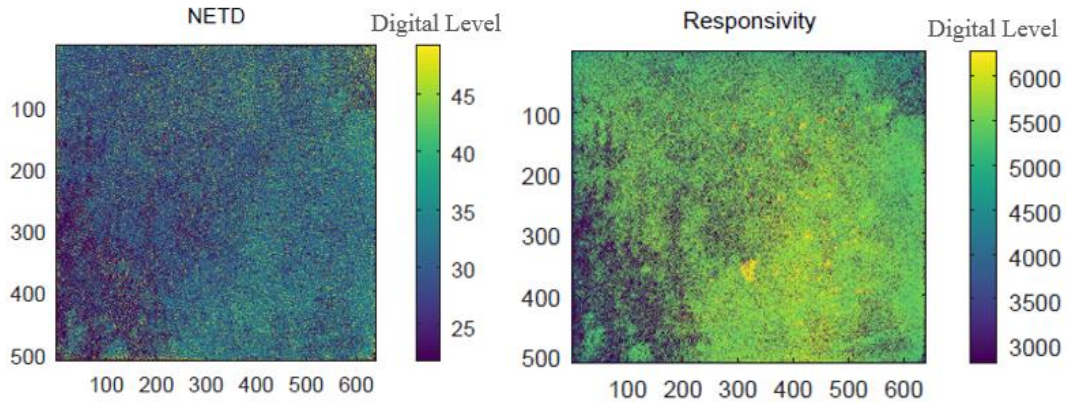

Figure 5.19. NETD and responsivity mapping for 640 x 512 T2SL FPA.

In responsivity mapping of Figure 5.19, some locations yield high responsivity at almost middle of FPA in small groups. These regions are also seen in cold and hot frame averages mapping figures (Figure 5.17). The reason for this type uniformity is related to underfill injection. Gaps in between bonded In bumps are filled with an epoxy to protect bumps and to create a dielectric region between ROIC and FPA. It is known that underfill epoxies used for cooled detectors generally lead non-uniformity problems, and this is the typical problem for most of the manufacturers and developers. Moreover, some underfill epoxies reduce the responsivity of pixels. Same problems are encountered in our T2SL FPAs. Regions, where filled by an underfill, give a response which strictly depends on filling ability or property of underfill. How much uniform filling is or how much filled by an epoxy are decisive mechanisms for showing a uniform response. The region, where underfill cannot reach, yields higher response since the reduction in responsivity by underfilling is not valid in this case. If FPA consist of bobbles between FPA and ROIC in which regions are un-filled by epoxy, these bobbled regions yield higher response. Returning to small regions which give a higher response in our FPA, unintentionally created bobbles blocks reduction of responsivity which is caused by underfill, and these regions give higher responses than other regions. As a result of this, the uniformity of FPA is disturbed. This problem can also be seen in Figure 5.20 which demonstrates low and high responsivity pixel mapping.

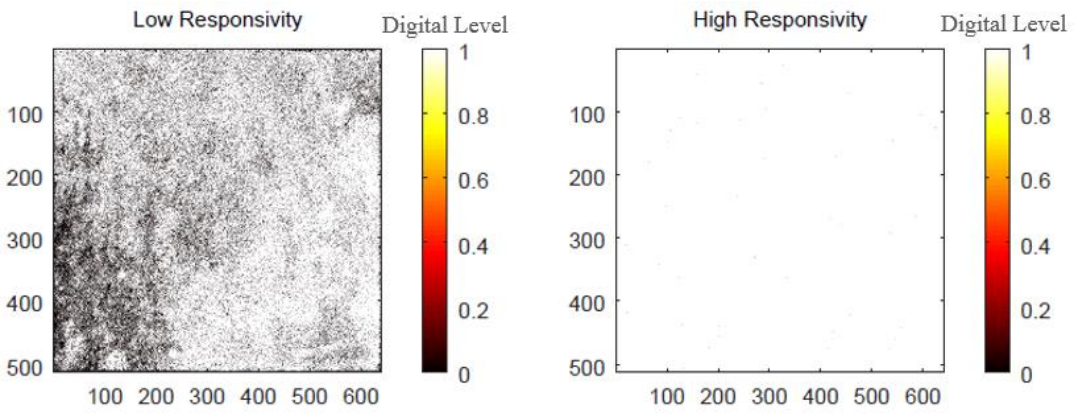

Figure 5.20. Low and high responsivity mapping for 640 x 512 T2SL FPA.

The scale for low responsivity figure is that shiny spots correspond to pixels having accepted responsivity values, and dark spots correspond to pixels yielding low responsivity. Contrary to low responsivity scale, dark spots show pixels giving high responses. As it is expected, pre-defined bad pixel location gives a low response like in Figure 5.20. The non-uniformity, caused by underfill, is unfolded with these mapping figures. Bobbled regions where underfill cannot reach can also be seen in high responsivity graph as a narrowed region. This narrowing depends on the definition of high responsivity in the script. Actually, the real point in here is that pixel located in the bobbled region; in other words, regions, where underfill cannot reach, yield responsivity value that relies on pre-defined responsivity range. Therefore, it is concluded that underfill epoxy significantly reduces the response of pixels.

The last parameter for a pixel to be named as bad or good is high NETD definition. Thus, high NETD and sum of pre-defined bad pixels' mappings are also analyzed, and they are shown in Figure 5.21. Scale for high NETD mapping is that dark spots represent pixels yielding low NETD. The non-uniformity in pre-defined bad pixel location is observed in high NETD mapping as it is expected. The scale for bad pixel map is that darker-blue spots represent pixels marked as bad either high noise, low responsivity, high responsivity or high NETD whereas yellowish spots correspond to accepted pixels.

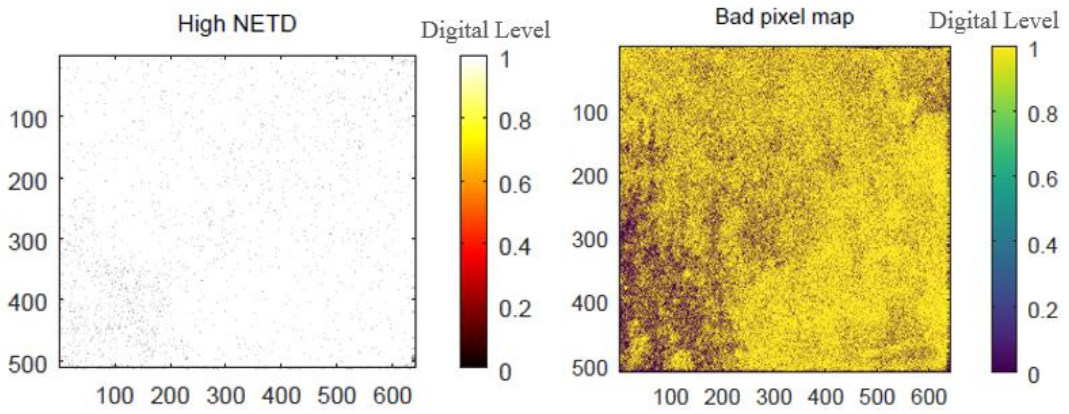

Figure 5.21. High NETD and total bad pixel mapping for 640 x 512 T2SL FPA.

The bad pixel mapping, shown in Figure 5.21, clearly exhibits that FCB and underfill problems disturb the uniformity of FPA and create bad pixels. The last result of these characterizations is NETD histogram presented in Figure 5.22.

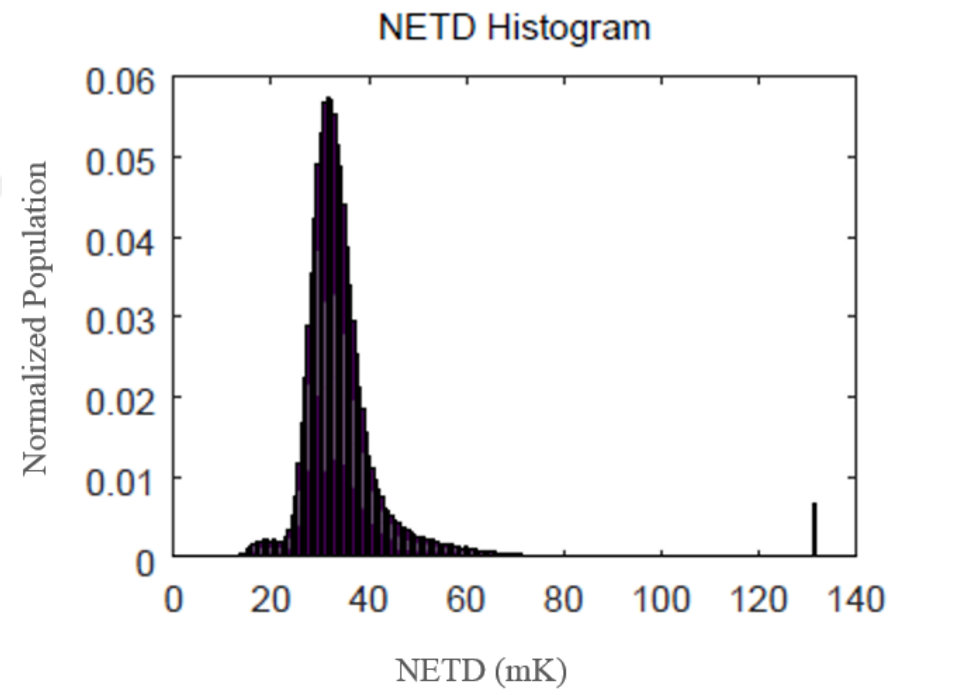

Figure 5.22. NETD histogram for 640 x 512 T2SL FPA.

The x-axis of NETD histogram is the normalized population of pixels yielding corresponding NETD value. FPA gives 30 mK NETD value at 2 ms integration time. This level of NETD for such FPA is comparable to values reported in literature, and it is the very promising result. However, almost 1 % of the population of pixels yields higher NETD value at around 130 mK. This is the value that bad pixels are in charge.

The last characterization is performed by measuring the spectral response of the fabricated detector. In Figure 5.23, the responsivity spectrum for different bias voltages is demonstrated.

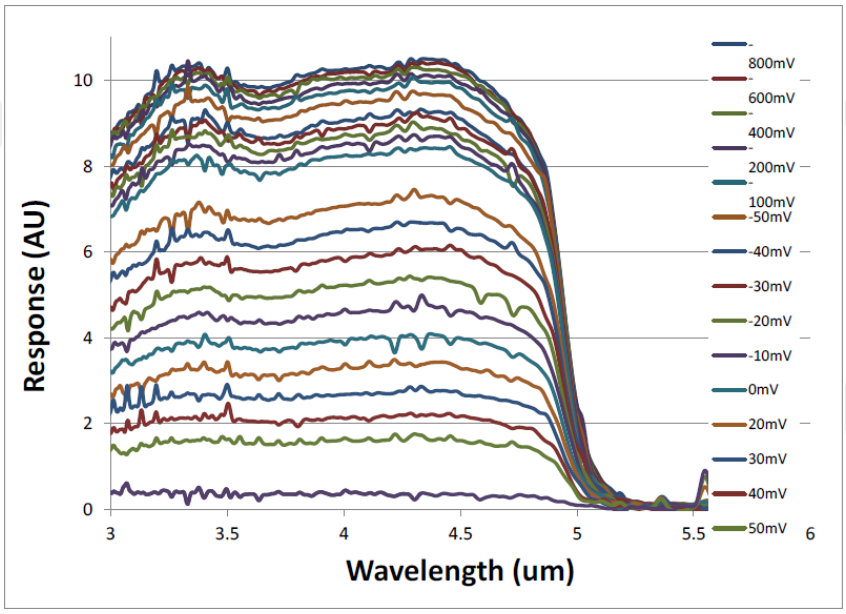

Figure 5.23. Responsivity spectrum for the T2SL FPA for varying bias voltages.

From the graph of responsivity spectrum, the cut-off wavelength, which is the wavelength that peak responsivity value drops 50 % of itself, is calculated as 4.92 µm.

The responsivity value is not calculated for this FPA since it was the initially-fabricated FPA, and it contains lots of parameters that should be improved. However, the responsivity for optimized FPA, whose images acquired by that FPA will be shown in next section, is equal to 1.2 A/W. Moreover, the quantum efficiency of that FPA for 4.92 µm cut-off wavelength is calculated as 60 %. Quantum efficiency (η) is also comparable to values reported in literature.

5.4. FPA Image Demonstration of T2SL FPA

Firstly, the reduction in FPA image quality caused by the high dark current will be shown in this section. Moreover, the images acquired by PECVD SiO_2 passivated and PECVD SiO_2 passivated plus $(NH_4)_2S$ pre-treated FPAs will be compared. Afterwards, the effect of substrate removal on FPA image will be shown for initially fabricated and marked as dummy FPA. The last demonstration for this thesis study will be the image of optimized T2SL FPA.

As it is remembered from Section 5.1.3.2, dark currents of differently passivated samples are compared at large area pixel level in terms of individual pixel dark currents and dark current densities. $(NH_4)_2S$ pre-treated sample has given the highest dark current. Moreover, in Figure 5.4, the comparison of PECVD SiO_2 passivated and PECVD SiO_2 passivated plus $(NH_4)_2S$ pre-treated samples have been discussed. Samples differing from each other only by $(NH_4)_2S$ pre-treatment has shown significantly different results which pre-treated sample has given $2\,x\,10^3$ times higher value. The effect of this high current on image quality will be demonstrated in this section. Two T2SL FPAs are produced with same fabrication process. The difference between them is that one of sample is treated by $(NH_4)_2S$ before PECVD of SiO_2. The other samples' SiO_2 is deposited directly (without pre-treatment). In Figure 5.24, an image acquired by a $(NH_4)_2S$ pre-treatment FPA is presented.

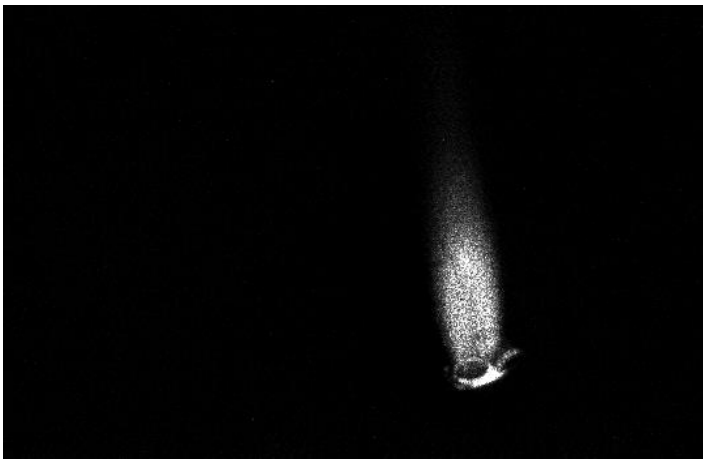

Figure 5.24. An image acquired by a 640 x 512 MWIR SiO_2 passivated and $(NH_4)_2S$ pre-treatment FPA at 77K.

As it is seen in Figure 5.24, the response of the detector is so small that can only gather photons from external lighter having a relatively high temperature. In fact, lighter can hardly be seen. The detector is almost saturated only by dark current, and it is not possible to get a response for incoming photons. However, in Figure 5.25, the image acquired by SiO_2 passivated FPA is demonstrated. The integration time is kept fixed for untreated sample whereas it is varied for different bias voltages. However, the achievable image is in Figure 5.24 with the best effort. Also, both images are taken with $f/2.3$ optics at 77 K.

Figure 5.25. An image acquired by a 640 x 512 MWIR SiO_2 passivated T2SL FPA at 77 K.

Even if some dead pixels and bad pixel areas are observed, the image is dramatically better than pre-treated FPA image. Besides, observed dead or bad pixels are not directly related not to apply pre-treatment. Otherwise, they are mostly coming from post-process step such as FCB. Therefore, the pre-treatment with $(NH_4)_2S$ is not applicable for T2SL structures unless more improvements are provided in the application of this treatment.

The effect of GaSb substrate on the absorption of photons is explained in Section 4.2.7. This absorption causes to decrease in the number of photons that can reach active layer. Furthermore, GaSb substrate is also lead blurring in images. In Figure 5.26, 77 K image of initially fabricated and marked as dummy FPA is demonstrated.

The substrate of this FPA is grinded as substrate remains ~50 μm. The image is acquired with $f/2.3$ optics and 2 ms integration time. Upper left hand side of FPA is damaged at grinding cycle, and wafer initially has large void defect at middle of the sample. The blurring caused by GaSb substrate can be easily seen.

Figure 5.26. An image acquired by a T2SL FPA having 50 μm substrate.

After the image is acquired, the FPA is un-mounted from LCC socket, and wirebonds are ripped off. It is observed that FPA is cracked most probably at cooling cycle of FPA. Even if it is anticipated that these cracks reveal additional problems like attack of chemical etchant used in chemical etching of the substrate, the risk chanced in order to investigate the effect of substrate visually. Afterwards, the 50 μm-thick-GaSb substrate is completely removed with chemical etching. The image is re-acquired with same conditions such as $f/2.3$ optics and 2 ms integration time at 77 K. In Figure 5.27, the image acquired by same FPA with completely removed substrate is demonstrated. As it is estimated, additional problems are observed. The chemical etchant has attacked FPA at defect and cracks. Also, at some minor points, additional in-responsive pixels find out.

Figure 5.27. An image acquired by a T2SL FPA having completely removed substrate.

However, the blurring of the image disappears although image seems not to be better than other with initial look. This comparison shows that GaSb substrate significantly affects absorption of a photon and creates blurring in FPA image. Therefore, GaSb substrate should be removed entirely in T2SL detectors for better performance.

As a result of investigations and characterizations performed on either large area samples or low-grade FPAs, the final and developed fabrication procedure for 640 x 512 MWIR 15 µm pitch T2SL FPA is as follows:

- Mesa structures are formed with the wet etching method.
- Ti/Au ohmic contact metallization is adopted.
- FPAs are passivated with polyimide, and polyimide is cured.
- UBM and In bump formation steps are performed with the same lithography.
- After FCB process, underfill is injected, and two-step substrate removal procedure, grinding and chemical etching, is applied.

When wirebonding and LCC mounting of FPA are completed, FPA is ready for characterization and image demonstration.

With necessary improvements in fabrication processes and gathered characterization data, the optimized 640 x 512 15 µm pixel pitch MWIR Type-II Superlattice FPA is obtained. An image acquired by this FPA is presented in Figure 5.28.

Figure 5.28. An image acquired by a 640 x 512 MWIR Type-II Superlattice Detector.

The image shown in Figure 5.28 is recorded with $f/2.3$ optics and 2 ms integration time at 60 mV reverse bias and 77 K. The cut-off wavelength for this detector is 4.92 µm. The responsivity is equal to $1.2\ \mathrm{A/W}$ with quantum efficiency $(\eta) > 60\ \%$ without anti-reflection. The measured NETD is 30 mK at 77 K. The operability is successfully reached at $99\ \%$. Moreover, the dark current density of large area detector fabricated from same wafer with same fabrication cycle is $3.1\ x\ 10^{-8}\ \mathrm{A/cm^{-2}}$ for 220 µm x 220 µm area diode. Results that are reached at thesis work are comparable to literature, and at some points, better values are reported in this thesis.

CHAPTER 6

CONCLUSIONS AND FUTURE WORK

This thesis reports on design and fabrication of state of the art Type-II Superlattice (T2SL) detector. The work covers all stages of the focal plane array implementation including the design of detector material, detector and focal plane array microfabrication, and detailed characterizations at both FPA and pixel levels.

Scanning Electron Microscopy (SEM) technique has been used for morphologic investigations of fabrication processes to develop necessary conditions. Characterizations at pixel level have been carried out on large area diodes. The experimented fabrication methods for the production of T2SL FPAs have been compared in terms of current-voltage characteristics. The dark current modeling for large area diode has been presented to distinguish the dominant mechanism at different bias regions. FPA level characterizations have been performed on initially fabricated FPAs to differentiate the effects of the fabrication process. Fabricated FPA is mapped according to defined parameters for NETD, noise, and responsivity. The reasons for bad pixels which are marked in terms of threshold and mean values of each phenomenon are also investigated. The NETD and responsivity values for optimized FPA is calculated and presented in the thesis.

Moreover, image-level comparisons of experimented fabrication processes such as effect of pre-treatment over FPA image and advancement in image quality with substrate removal are referred.

After morphologic investigations of fabrication processes and characterizations at large area pixel level and FPA level besides with dark current simulation, image acquisition with the 640 x 512 15 µm pitch MWIR Type-II Superlattice FPA is demonstrated. The image is obtained with $f/2.3$ optics and 2 ms integration time at 60 mV reverse bias and at 77 K. Detector has 4.92 µm cut-off wavelength, $1.2\ \mathrm{A/W}$ responsivity with quantum efficiency $(\eta) >$ 60 %, 30 mK NETD at 77 K and 99 % operability. The dark current density of large area detector (220 µm x 220 µm) fabricated on same wafer with same fabrication steps is $3.1\ x\ 10^{-8}\ \mathrm{A/cm^{-2}}$.

In conclusion, large format (640 x 512), small pixel pitch (15 µm), high-performance MWIR T2SL FPA is fabricated in this thesis work. Although results that are reached at thesis work are lower (dark currents, NETD) and higher (responsivity, quantum efficiency) when they are compared to results reported in literature, reaching better performance (at least same performance) with reduced consumptions such as power and cost, smaller size detectors approaching today's theoretical limits and beyond these limits, and diversification of portfolio with innovative designs are main objectives for future studies.

REFERENCES

[1] W. Herschel, “Experiments on the Refrangibility of the Invisible Rays of the Sun. By William Herschel, LL. D. F. R. S.,” *Philos. Trans. R. Soc. London* **90**, 284–292 (1800).

[2] T. J. Seebeck, “Ueber die magnetische Polarisation der Metalle und Erze durch Temperatur-Differenz,” *Ann. Phys.* **82**, 133–160 (1826).

[3] A. Rogalski, “Infrared detectors: An overview,” in *Infrared Phys. Technol.* **43** (2002).

[4] E. S. Barr, “The Infrared Pioneers - II. Macedonio Melonni,” *Infrared Phys.* **2**, 63–67 (1962).

[5] E. S. Barr, “The infrared pioneers III. Samuel Pierpont Langley,” *Infrared Phys.* **3**, 195–206 (1963).

[6] W. Smith, “Effect of Light on Selenium During the Passage of An Electric Current,” in *Nature* **7** (1873).

[7] T. W. Case, “Notes on the change of resistance of certain substances in light,” *Phys. Rev.* **9**, 305–310 (1917).

[8] A. Tolungüç, “Molecular Beam Epitaxy Growth and Characterization of Mercury Cadmium Telluride Epilayers for Infrared Detector Applications” (Middle East Technical University, 2011).

[9] W. D. Lawson, S. Nielsen, E. H. Putley, and A. S. Young, “Preparation and properties of HgTe and mixed crystals of HgTe-CdTe,” *J. Phys. Chem. Solids* **9**, 325–329 (1959).

[10] L. Esaki and R. Tsu, “Superlattice and Negative Differential Conductivity in Semiconductors,” *IBM J. Res. Dev.* **14**, 61–65 (1970).

[11] L. L. Chang, L. Esaki, and G. A. Sai-Halaz, “Infrared Optical devices of layered structure,” *IBM Tech. Discl. Bull* **20**, 2019 (1977).

[12] L. Esaki; and H. Sakaki, “New Photoconductor,” *IBM Tech Discl. Bull.* **20**, 2456 (1977).

[13] D. D. Coon and R. P. G. Karunasiri, “New mode of IR detection using quantum wells,” *Appl. Phys. Lett.* **45**, 649 (1984).

[14] L. C. Chiu, J. S. Smith, S. Margalit, A. Yariv, and A. Y. Cho, “Application of internal photoemission from quantum-well and heterojunction superlattices to infrared photodetectors,” *Infrared Phys.* **23**, 93–97 (1983).

[15] L. C. West and S. J. Eglash, “First observation of an extremely large-dipole infrared transition within the conduction band of a GaAs quantum well,” *Appl. Phys. Lett.* **46**, 1156–1158 (1985).

[16] B. F. Levine, K. K. Choi, C. G. Bethea, J. Walker, and R. J. Malik, “New 10 μm infrared detector using intersubband absorption in resonant tunneling GaAlAs superlattices,” *Appl. Phys. Lett.* **50**, 1092–1094 (1987).

[17] M. J. E. Golay, “A pneumatic infra-red detector,” *Rev. Sci. Instrum.* **18**, 357–362 (1947).

[18] A. Rogalski, “History of infrared detectors,” *Opto-electronics Rev.* **20**, 279–308 (2012).

[19] Y. Arslan, “High Performance Focal Plane Array Technologies From Short to Long Wavelength Infrared Bands” (Middle East Technical University, 2014).

[20] G. Gaussorgues, *Infrared Thermography* (Springer Netherlands, Dordrecht, 1994).

[21] Sch., “Wikimedia Foundation Inc.,” [Online]. <https://upload.wikimedia.org/wikipedia/commons/f/ff/BlackbodySpectrum_loglog_150dpi_en.png> (Accessed: 21 January 2018).

[22] A. Rogalski, *Infrared Devices and Techniques*, 2nd ed., K. Chrzanowski, Ed. (2002).

[23] J. T. Longo, D. T. Cheung, A. M. Andrews, C. C. Wang, and J. M. Tracy, “Infrared focal planes in intrinsic semiconductors,” *IEEE Trans. Electron Devices* **25**, 213–232 (1978).

[24] A. Rogalski, “History of infrared detectors,” *Opto-Electronics Rev.* **18**, 121–136 (2010).

[25] S. H. Bae, S. J. Lee, Y. H. Kim, H. C. Lee, and C. K. Kim, “Analysis of 1/f noise in LWIR HgCdTe photodiodes,” *J. Electron. Mater.* **29**, 877–882 (2000).

[26] J. Bajaj, G. M. Williams, N. H. Sheng, M. Hinnrichs, D. T. Cheung, J. P. Rode, and W. E. Tennant, "Excess (1/ f) noise in $Hg_{0.7}Cd_{0.3}Te$ p-n junctions," *J. Vac. Sci. Technol. A Vacuum, Surfaces, Film.* **3**, 192–194 (1985).

[27] S. Ozer and C. Besikci, "Assessment of InSb photodetectors on Si substrates," *J. Phys. D. Appl. Phys.* **36**, 559–563 (2003).

[28] C. Besikci, "EE 514-Infrared Devices and Systems," in *Infrared Devices Syst.* (2012).

[29] R. G. Driggers, R. Vollmerhausen, J. P. Reynolds, J. Fanning, and G. C. Holst, "Infrared detector size: how low should you go?," *Opt. Eng.* **51**, 63202 (2012).

[30] S. D. . Gunapala, D. R. Rhiger, and C. Jagadish, *Advances in Infrared Photodetectors*, 1st ed., (Amsterdam, The Netherlands : Academic Press, 2011).

[31] H. Frensley, W. R., and Kroemer, "Theory of the energy-band lineup at an abrupt semiconductor heterojunction," *Phys. Rev. B Solid State* **16**, 2642–2652 (1977).

[32] W. A. Harrison, "Elementary theory of heterojunctions," *J. Vac. Sci. Technol.* **14**, 1016–1021. (1977).

[33] J. N. Schulman and Y.-C. Chang, "Band mixing in semiconductor superlattices," *Phys. Rev. B* **31**, 2056–2068 (1985).

[34] D. L. Smith and C. Mailhiot, "Proposal for strained type II superlattice infrared detectors," *J. Appl. Phys.* **62**, 2545–2548 (1987).

[35] R. H. Miles, D. H. Chow, J. N. Schulman, and T. C. McGill, "Infrared optical characterization of $InAs/Ga_{1-x}In_xSb$ superlattices," *Appl. Phys. Lett.* **57**, 801–803 (1990).

[36] H. Mohseni, V. Litvinov, and M. Razeghi, "Interface-induced suppression of the Auger recombination in type-II InAs/GaSb superlattices," *Phys. Rev. B* **58**, 15378–15380 (1998).

[37] F. Fuchs, U. Weimer, W. Fletschen, J. Schmitz, E. Ahlswede, M. Walther, J. Wagner, and P. Koidl, "High performance $InAs/Ga_{1-x}In_xSb$ superlattice infrared photodiodes," *Appl. Phys. Lett.* **71**, 3251–3253 (1997).

[38] J. L. Johnson, L. A. Samoska, A. C. Gossard, J. L. Merz, M. D. Jack, G. R. Chapman, B. A. Baumgratz, K. Kosai, and S. M. Johnson, "Electrical and optical properties of infrared photodiodes using the $InAs/Ga_{1-x}In_xSb$ superlattice in heterojunctions with GaSb," *J. Appl. Phys.* **80**, 1116–1127 (1996).

[39] N. Herres, F. Fuchs, J. Schmitz, K. M. Pavlov, J. Wagner, J. D. Ralston, P. Koidl, C. Gadaleta, and G. Scamarcio, "Effect of interfacial bonding on the structural and vibrational properties of InAs/GaSb superlattices," *Phys. Rev. B* **53**, 15688–15705 (1996).

[40] A. Y. Lew, S. L. Zuo, E. T. Yu, and R. H. Miles, "Anisotropy and growth-sequence dependence of atomic-scale interface structure in InAs/$Ga_{1-x}In_xSb$ superlattices," *Appl. Phys. Lett.* **70**, 75–77 (1997).

[41] F. Fuchs, L. Burkie, W. Pletschen, J. Schmitz, M. Waither, H. Gullich, N. Herres, S. Muller, F. Angewandte, et al., "InAs / GaInSb infrared superlattice diodes : Correlation between surface morphology and electrical performance," *Proc. SPIE* **3794**, 41–46 (1999).

[42] J. Steinshnider, M. Weimer, R. Kaspi, and G. W. Turner, "Visualizing interfacial structure at non-common-atom heterojunctions with cross-sectional scanning tunneling microscopy," *Phys. Rev. Lett.* **85**, 2953–2956 (2000).

[43] B. R. Bennett, "Strain relaxation in InAs / GaSb heterostructures," *Appl. Phys. Lett.* **73**, 3736 (1998).

[44] G. J. Brown, F. Szmulowicz, R. Linville, A. Saxler, K. Mahalingham, C. H. Lin, C. H. Kuo, and W. Y. Hwang, "Type-II superlattice photodetector on a compliant GaAs substrate," *IEEE Photonics Technol. Lett.* **12**, 684–686 (2000).

[45] C. M. Ciesla, B. N. Murdin, C. R. Pidgeon, R. A. Stradling, C. C. Phillips, M. Livingstone, I. Galbraith, D. A. Jaroszynski, C. J. G. M. Langerak, et al., "Suppression of Auger recombination in arsenic-rich $InAs_{1-x}Sb_x$ strained layer super-lattices," *J. Appl. Phys.* **80**, 2994–2997 (1996).

[46] S. Maimon and G. W. Wicks, "nBn detector, an infrared detector with reduced dark current and higher operating temperature," *Appl. Phys. Lett.* **89** (2006).

[47] S. Maimon, "Reduced Dark Current Photodetector," 7,687,871 B2 (2010).

[48] P. Klipstein, "XBn barrier photodetectors for high sensitivity and high operating temperature infrared sensors," in *Proc SPIE* **6940**, (2008).

[49] J. B. Rodriguez, E. Plis, G. Bishop, Y. D. Sharma, H. Kim, L. R. Dawson, and S. Krishna, "NBn structure based on InAs/GaSb type-II strained layer superlattices," *Appl. Phys. Lett.* **91** (2007).

[50] A. Khoshakhlagh, J. B. Rodriguez, E. Plis, G. D. Bishop, Y. D. Sharma, H. S. Kim, L. R. Dawson, and S. Krishna, "Bias dependent dual band response from InAsGa (In) Sb type II strain layer superlattice detectors," *Appl. Phys. Lett.* **91** (2007).

[51] A. D. Hood, A. J. Evans, A. Ikhlassi, D. L. Lee, and W. E. Tennant, "LWIR strained-layer superlattice materials and devices at teledyne imaging sensors," in *J. Electron. Mater.* **39**, (2010).

[52] B. M. Nguyen, D. Hoffman, P. Y. Delaunay, and M. Razeghi, "Dark current suppression in type II InAsGaSb superlattice long wavelength infrared photodiodes with M-structure barrier," *Appl. Phys. Lett.* **91** (2007).

[53] I. Vurgaftman, E. H. Aifer, C. L. Canedy, J. G. Tischler, J. R. Meyer, J. H. Warner, E. M. Jackson, G. Hildebrandt, and G. J. Sullivan, "Graded band gap for dark-current suppression in long-wave infrared W-structured type-II superlattice photodiodes," *Appl. Phys. Lett.* **89** (2006).

[54] P. Y. Delaunay, A. Hood, B. M. Nguyen, D. Hoffman, Y. Wei, and M. Razeghi, "Passivation of type-II InAsGaSb double heterostructure," *Appl. Phys. Lett.* **91** (2007).

[55] N. Gautam, H. S. Kim, M. N. Kutty, E. Plis, L. R. Dawson, and S. Krishna, "Performance improvement of longwave infrared photodetector based on type-II InAs/GaSb superlattices using unipolar current blocking layers," *Appl. Phys. Lett.* **96** (2010).

[56] D. Z. Y. Ting, C. J. Hill, A. Soibel, S. A. Keo, J. M. Mumolo, J. Nguyen, and S. D. Gunapala, "A high-performance long wavelength superlattice complementary barrier infrared detector," *Appl. Phys. Lett.* **95** (2009).

[57] E. A. Plis, "InAs/GaSb Type-II Superlattice Detectors," *Adv. Electron.* **2014**, 1–12 (2014).

[58] H. Kroemer, "The 6.1 Å family (InAs, GaSb, AlSb) and its heterostructures: A selective review," in *Phys. E Low-Dimensional Syst. Nanostructures* **20**, (2004).

[59] C. Cervera, K. Jaworowicz, H. Aït-Kaci, R. Chaghi, J. B. Rodriguez, I. Ribet-Mohamed, and P. Christol, "Temperature dependence performances of InAs/GaSb superlattice photodiode," in *Infrared Phys. Technol.* **54**, (2011).

[60] X. Li, D. Jiang, Y. Zhang, D. Wang, Q. Yu, T. Liu, H. Ma, and L. Zhao, "Investigation of dark current mechanisms on type-II InAs/GaSb superlattice very long wavelength infrared detectors," *J. Phys. D. Appl. Phys.* **49**, 165105 (IOP Publishing, 2016).

[61] D. R. Rhiger, R. E. Kvaas, S. F. Harris, and C. J. Hill, "Characterization of LWIR diodes on InAs/GaSb Type-II superlattice material," *Infrared Phys. Technol.* **52**, 304–309 (2009).

[62] M. Walther, R. Rehm, F. Fuchs, J. Schmitz, J. Fleißner, W. Cabanski, D. Eich, M. Finck, W. Rode, et al., "256×256 focal plane array midwavelength infrared camera based on InAs/GaSb short-period superlattices," *J. Electron. Mater.* **34**, 722–725 (2005).

[63] M. Walther, R. Rehm, J. Fleissner, J. Schmitz, J. Ziegler, W. Cabanski, and R. Breiter, "InAs/GaSb type-II short-period superlattices for advanced single and dual-color focal plane arrays," in *Proc. SPIE* **6542**, B. F. Andresen, G. F. Fulop, and P. R. Norton, Eds., (2007).

[64] P. Y. Delaunay, B. M. Nguyen, D. Hoffman, and M. Razeghi, "320x256 infrared Focal Plane Array based on Type II InAs/GaSb superlattice with a 12 μm cutoff wavelength," *Spie* **6542** (2007).

[65] D. R. Rhiger, R. E. Kvaas, S. F. Harris, R. E. Bornfreund, Y. N. Thai, C. J. Hill, J. V. Li, S. D. Gunapala, and J. M. Mumolo, "Progress with type-II superlattice IR detector arrays," in *SPIE* **6542**, (2007).

[66] H. S. Kim, E. Plis, J. B. Rodriguez, G. D. Bishop, Y. D. Sharma, L. R. Dawson, S. Krishna, J. Bundas, R. Cook, et al., "Mid-IR focal plane array based on type-II InAsGaSb strain layer superlattice detector with nBn design," *Appl. Phys. Lett.* **92** (2008).

[67] E. Plis, H. S. Kim, J. B. Rodriguez, G. D. Bishop, Y. D. Sharma, a Khoshakhlagh, L. R. Dawson, J. Bundas, R. Cook, et al., "nBn based infrared detectors using type-II InAs/(In,Ga)Sb superlattices," *Proc. SPIE - Int. Soc. Opt. Eng.* **6940**, 69400–69401 (2008).

[68] M. Walther, R. Rehm, J. Schmitz, J. Niemasz, F. Rutz, A. Wörl, L. Kirste, R. Scheibner, J. Wendler, et al., "Defect density reduction in InAs / GaSb type II superlattice focal plane array infrared detectors," *Quantum* **7945**, 1–10 (2011).

[69] H. Martijn, C. Asplund, R. M. von Würtemberg, and H. Malm, "High-performance MWIR type-II superlattice detectors," *Proc. SPIE 8704, Infrared Technol. Appl. XXXIX* **8704**, 87040Z–87040Z–9 (2013).

[70] H. Katayama, J. Murooka, M. Naitoh, R. Sato, S. Kawasaki, Y. Itoh, S. Sugano, T. Takekawa, M. Kimata, et al., "Development status of Type II superlattice infrared detector in JAXA," *Proc. SPIE* **8704**, 870416 (2013).

[71] G. Chen, A. Haddadi, A. Hoang, R. Chevallier, and M. Razeghi, "Demonstration of type-II superlattice MWIR minority carrier unipolar imager for high operation temperature application," 45–47 (2015).

[72] K. Miura, K. Machinaga, S. Balasekaran, T. Kawahara, M. Migita, H. Inada, Y. Iguchi, M. Sakai, J. Murooka, et al., "High performance type II superlattice focal plane array with 6μm cutoff wavelength," 98190V (2016).

[73] J. Jenkins, S. Terterian, B. Tu, W. Strong, M. Roebuck, T. J. De Lyon, H. Sharifi, R. D. Rajavel, J. Caulfield, et al., "Fabrication of small pitch, high definition (HD) 1kx2k/5um MWIR focal-plane-arrays operating at high temperature (HOT)," *Spie* **10177**, 101771J (2017).

[74] H. Sharifi, M. Roebuck, S. Terterian, J. Jenkins, B. Tu, W. Strong, T. J. De Lyon, R. D. Rajavel, J. Caulfield, et al., "Advances in III-V bulk and superlattice-based high operating temperature MWIR detector technology," *Spie* **10177**, 101770U (2017).

[75] E. Papis Polakowska, "Surface treatments of GaSb and related materials for the processing of mid-infrared semiconductor devices," *Electron Technol. - Internet J.* **38**, 1–34 (2006).

[76] O. Dier, C. Lin, M. Grau, and M.-C. Amann, "Selective and non-selective wet-chemical etchants for GaSb-based materials," *Semicond. Sci. Technol.* **19**, 1250–1253 (2004).

[77] R. Chaghi, C. Cervera, H. Aït-Kaci, P. Grech, J.-B. Rodriguez, and P. Christol, "Wet etching and chemical polishing of InAs/GaSb superlattice photodiodes," *Semicond. Sci. Technol.* **24**, 65010-1–6 (2009).

[78] K. M. Chang, J. J. Luo, C. Der Chiang, and K. C. Liu, "Wet etching characterization of InSb for thermal imaging applications," *Japanese J. Appl. Physics, Part 1 Regul. Pap. Short Notes Rev. Pap.* **45**, 1477–1482 (2006).

[79] F. Rutz, R. Rehm, J. Schmitz, J. Fleissner, M. Walther, and A. I. M. I. Gmbh, "InAs / GaSb superlattice focal plane array infrared detectors : manufacturing aspects," 1–10 (2009).

[80] H. Inada, K. Machinaga, S. B., K. Miura, Y. Tsuji, M. Migita, Y. Iguchi, H. Katayama, and M. Kimata, "Pretreatment for surface leakage current reduction in type-II superlattice MWIR photodetectors," 90700Z (2014).

[81] L. Yang, J. Deng, Y. Shi, Y. Chen, and B. Wu, "Fabrication and performance of InAs/GaSb type-II superlattices mid-wavelength infrared detectors," *Proc. SPIE* **8907**, 890741(8pp) (2013).

[82] H. Katayama, J. Murooka, R. Sato, M. Kimata, T. Kitada, T. Isu, M. Patrashin, and I. Hosako, "Development of type II superlattice detector for future space applications in JAXA," *Pacific Rim Conf. Lasers Electro-Optics, CLEO - Tech. Dig.* **8353**, 1–8 (2013).

[83] K. A. Olver, "A New Procedure for the Application and Curing of Polyimide Film on Gold Coated Silicon Wafers," *Sensors (Peterborough, NH)* (2009).

[84] P. Details, A. A. Promoter, and A. P. Precursor, "PI-2600 Series – Low Stress Applications," *Stress Int. J. Biol. Stress*, 1–4 (2009).

[85] A. Gin, Y. Wei, J. Bae, A. Hood, J. Nah, and M. Razeghi, “Passivation of type II InAs/GaSb superlattice photodiodes,” *Thin Solid Films* **447–448**, 489–492 (2004).

[86] A. Gin, Y. Wei, A. Hood, A. Bajowala, V. Yazdanpanah, M. Razeghi, and M. Tidrow, “Ammonium sulfide passivation of Type-II InAs/GaSb superlattice photodiodes,” *Appl. Phys. Lett.* **84**, 2037–2039 (2004).

[87] K. Miura, Y. Iguchi, T. Katsuyama, and Y. Kawamura, “Mid-infrared sensors with InAs/GaSb superlattice absorption layers grown on InP substrates,” *SEI Tech. Rev.* **1**, 58–62 (2014).

[88] K. Hackiewicz, P. Martyniuk, J. Rutkowski, and A. Kowalewski, “Calculations of Dark Current in Interband Cascade Type-II Infrared InAs/GaSb Superlattice Detector,” *Acta Phys. Pol. A* **132**, 1415–1419 (2017).

[89] B. Klein, E. Plis, M. N. Kutty, N. Gautam, A. Albrecht, S. Myers, and S. Krishna, “Varshni parameters for InAs/GaSb strained layer superlattice infrared photodetectors,” *J. Phys. D. Appl. Phys.* **44**, 75102 (2011).

[90] P. Martyniuk and A. Rogalski, “MWIR barrier detectors versus HgCdTe photodiodes,” *Infrared Phys. Technol.* **70**, 125–128 (2015).

[91] P. Martyniuk, J. Wróbel, E. Plis, P. Madejczyk, A. Kowalewski, W. Gawron, S. Krishna, and A. Rogalski, “Performance modeling of MWIR InAs/GaSb/B–$Al_{0.2}Ga_{0.8}Sb$ type-II superlattice nBn detector,” *Semicond. Sci. Technol.* **27**, 55002 (2012).

[92] Q. K. Yang, F. Fuchs, J. Schmitz, and W. Pletschen, “Investigation of trap-assisted tunneling current in InAs/(GaIn)Sb superlattice long-wavelength photodiodes,” *Appl. Phys. Lett.* **81**, 4757–4759 (2003).

APPENDIX A

OCTAVE SCRIPT

```
function [netd_mean, resp_mean_clean, noise_mean, cold_level, pixel_percentage_total_bad, netdnu, respnu, noisenu]=analysis()
clear;
close all;
plots_hide=1;
frames=64;
size_x=640;
size_y=512;
hot=zeros(size_y,size_x,frames);
cold=zeros(size_y,size_x,frames);
deltaT=10000;                % temperature difference between scenes in mK
resp_threshold_low=0.5;      % pixel with responsivity smaller than this will be marked as bad (mean responsivity)
resp_threshold_high=2;       % pixel with responsivity higher than this will be marked as bad (mean responsivity)
netd_threshold=3;            % pixel with NETD higher than this will be marked as bad (mean netd)
noise_threshold=3;           % pixel with noise higher than this will be marked as bad (mean noise)

list=dir('hot');             % data reading
for j=1:frames               % all hot frames are in hot variable as 3-D
[f, MSG]=fopen(strcat('hot\',list(j+2,1).name),'r' );
 for i=1:size_y
 hot(i,:,j)=fread(f, size_x,'uint16');
 endfor
fclose(f);
endfor

list=dir('cold');
for j=1:frames               % all cold frames are in cold variable as 3-D
[f, MSG]=fopen(strcat('cold\',list(j+2,1).name),'r' );
 for i=1:size_y
 cold(i,:,j)=fread(f, size_x,'uint16');
 endfor
fclose(f);
endfor
```

```
cold_mean=mean(cold,3);                % average in 3-D, cold mean frame
cold_noise=std(cold,0,3);              % standard deviation in 3-D, cold noise frame
hot_mean=mean(hot,3);                  % average in 3-D, hot mean frame
hot_noise=std(hot,0,3);                % not used
responsivity=hot_mean-cold_mean;
noise=cold_noise;
bad_resp_low=responsivity>mean(responsivity(:))*resp_threshold_low;        % map low responsivity pixels as
0 in the map bad_resp_low
bad_resp_high=responsivity<mean(responsivity(:))*resp_threshold_high;       % map high responsivity pixels as
0 in the map bad_resp_high
bad_noise=noise<mean(noise(:))*noise_threshold;          % map high noise pixels as 0 in the map bad_noise
bad=bad_resp_high & bad_resp_low & bad_noise;            % add all bad pixels in map bad
responsivity_nonzero=responsivity.*bad -1 + bad;         % bad pixels marked with -1 in responsivity

netd=deltaT*noise./responsivity_nonzero;
netd_clean=netd(bad);
resp_clean=responsivity_nonzero(bad);
bad_netd=netd<netd_threshold*mean(netd_clean(:));
cold_level=mean(mean(cold_mean));
operability=bad&bad_netd;

levels=figure("name","Levels");
imagesc(subplot(2,2,1),cold_mean,[mean(mean(cold_mean))/1.5 1.5*mean(mean(cold_mean))]);
set(subplot(2,2,1),"title","Cold Frames Average");
colorbar;

imagesc(subplot(2,2,2),hot_mean, [mean(mean(cold_mean))/1.5 1.5*mean(mean(cold_mean))]);
set(subplot(2,2,2),"title","Hot Frames Average");
colorbar;

imagesc(subplot(2,2,3),responsivity,[mean(mean(responsivity))/1.5 1.5*mean(mean(responsivity))]);
set(subplot(2,2,3),"title","Responsivity");
colorbar;

imagesc(subplot(2,2,4),cold_noise, [min(min(noise))/0.9 1.5*mean(mean(cold_noise))]);
set(subplot(2,2,4),"title","Noise");
colorbar;

bad_pixels=figure("name","Bad Pixels");
imagesc(subplot(2,2,1),bad_resp_low);
set(subplot(2,2,1),"title", "Low Responsivity");
colormap("hot");
colorbar;

imagesc(subplot(2,2,2),bad_resp_high);
set(subplot(2,2,2),"title", "High Responsivity");
colormap("hot");
colorbar;

imagesc(subplot(2,2,3),bad_noise);
set(subplot(2,2,3),"title", "High Noise");
colormap("hot");
colorbar;

imagesc(subplot(2,2,4),bad_netd);
set(subplot(2,2,4),"title", "High NETD");
colormap("hot");
colorbar;

figure_netd=figure("name","NETD");
imagesc(subplot(2,2,1),netd, [median(netd_clean(:))/1.5, 1.5*median(netd_clean(:))]);
set(subplot(2,2,1),"title", "NETD");
colorbar;
```

```
imagesc(subplot(2,2,2),operability);
set(subplot(2,2,2),"title", "Bad pixel map");
colorbar;

subplot(2,2,4);
hist(cold_noise(:),[2:median(cold_noise(:))/50:3*median(cold_noise(:))],1)
set(subplot(2,2,4),"title","Noise Histogram");

subplot(2,2,3);
hist(netd_clean(:),[median(netd_clean(:))/50:median(netd_clean(:))/50:4*median(netd_clean(:))],1);
set(subplot(2,2,3),"title","NETD Histogram");
text(0,650,pwd);

print (levels, "figures", "-dpdf");
print (figure_netd, "figures", "-dpdf", "-append");
print (bad_pixels, "figures", "-dpdf", "-append");
if(plots_hide) set (bad_pixels, "visible", "off"); end;
if(plots_hide) set (levels, "visible", "off"); end;
if(plots_hide) set (figure_netd, "visible", "off"); end;
save -ascii netd.txt netd;
save -ascii netd_clean.txt netd_clean;
save -ascii noise.txt noise;
save -ascii responsivity.txt responsivity;

%figure_netd_hist=figure("name","Responsivity Histogram");
%hist(responsivity(:),[min(responsivity):median(responsivity(:))/50:2*median(responsivity(:))],1);
netd_mean=mean(netd_clean(:));
netd_median=median(netd_clean(:));
netdnu=std(netd_clean(:),0)/netd_mean;

pixel_number_resp_low=640*512-sum(bad_resp_low(:));
pixel_percentage_resp_low=(1-sum(bad_resp_low(:))/640/512)*100;
pixel_number_resp_high=640*512-sum(bad_resp_high(:));
pixel_percentage_resp_high=(1-sum(bad_resp_high(:))/640/512)*100;
pixel_number_noisy=640*512-sum(bad_noise(:));
pixel_precentage_noisy=(1-sum(bad_noise(:))/640/512)*100;
pixel_number_netd_high=640*512-sum(bad_netd(:));
pixel_percentage_netd_high=(1-sum(bad_netd(:))/640/512)*100;
pixel_number_total_bad=640*512-sum(operability(:));
pixel_percentage_total_bad=(1-sum(operability(:))/640/512)*100;

resp_mean_raw=mean(responsivity_nonzero(:));
resp_mean_clean=mean(resp_clean(:));
respnu=std(resp_clean(:),0)/resp_mean_clean;
noise_mean=mean(noise(:));
noisenu=std(noise(:),0)/noise_mean;

a=fopen("report.txt", "w");
fprintf(a, "%s",pwd);
fprintf(a, "\r\n\r\nNETD(mK):\r\nMean: %.3d  Median: %.3d\r\n",netd_mean,netd_median );
fprintf(a, "\r\nBad Pixels:\r\nResponsivity Low: %d pixels %.2d%%",
pixel_number_resp_low,pixel_percentage_resp_low);
fprintf(a, "\r\nResponsivity High: %d pixels %.2d%%",pixel_number_resp_high,pixel_percentage_resp_high);
fprintf(a, "\r\nNoise High: %d pixels %.2d%%\n",pixel_number_noisy, pixel_precentage_noisy );
fprintf(a, "\r\nNetd High: %d pixels %.2d%%\n",pixel_number_netd_high, pixel_percentage_netd_high );
fprintf(a, "\r\nTotal Bad: %d pixels %.2d%%\r\n",pixel_number_total_bad,pixel_percentage_total_bad );
```

```
fprintf(a, "\r\nStatistics:\r\nResponsivity: %.5d (raw)",resp_mean_raw);
fprintf(a, "\r\nResponsivity: %.5d (clean)",resp_mean_clean);
fprintf(a, "\r\nNoise: %.3d",noise_mean);
fprintf(a, "\r\nCold Mean: %.5d",mean(cold_mean(:)));
fprintf(a, "\r\nHot Mean: %.5d\r\n",mean(hot_mean(:)));
fprintf(a, "\r\nParameters:\r\nTemperature Differance: %d K",deltaT/1000);
fprintf(a, "\r\nResponse Low Threshold: %d x",resp_threshold_low);
fprintf(a, "\r\nResponse High Threshold: %d x",resp_threshold_high);
fprintf(a, "\r\nNoise High Threshold: %d x",noise_threshold);
fclose(a);
endfunction
```